

Department of Physics and Astronomy  
University of Heidelberg

2015

Master thesis in Physics

submitted by

Jonas Kuhn

born in Sigmaringen



Trace gas imaging in the atmosphere with a  
Fabry-Pérot interferometer - A case study for sulfur  
dioxide

This Master thesis has been carried out by Jonas Kuhn  
at the  
Institute of Environmental Physics  
under the supervision of  
Prof. Dr. Ulrich Platt



## **Trace gas imaging in the atmosphere with a Fabry-Pérot interferometer - A case study for sulfur dioxide:**

Atmospheric trace gas imaging allows the direct assessment of chemical dynamics, transport and mixing processes and is therefore desired in atmospheric physics and chemistry. For instance, the application of imaging measurements at trace gas point sources can substantially improve the determination of emission fluxes. The SO<sub>2</sub> Camera is an imaging technique that is already applied at volcanoes. However, cross interferences of the detection principle can lead to significant uncertainties in the trace gas quantification.

In this thesis an imaging technique employing a Fabry-Pérot interferometer (FPI) is introduced. In order to identify and quantify a trace gas species, the FPI's transmittance spectrum is matched to the molecule's absorption structures.

The method was investigated for sulfur dioxide (SO<sub>2</sub>) in a model study. Moreover, a one pixel prototype was built as proof of concept. The detection limit reached with this simple prototype device is  $\sim 8.5 \cdot 10^{16}$  molec cm<sup>-2</sup> or  $\sim 34$  ppm m of SO<sub>2</sub> in a 1 s measurement period. It could be shown, that compared to the SO<sub>2</sub> Camera, the FPI technique has drastically reduced cross interferences to ozone, clouds and aerosol extinction. Finally, several implementations of the technique in an imaging instrument were proposed and discussed.

## **Bildgebende Spurenstofffernerkundung in der Atmosphäre mit Hilfe eines Fabry-Pérot Interferometers - Eine Fallstudie für Schwefeldioxid:**

Bildgebende Messungen atmosphärischer Spurenstoffe erlauben die direkte Untersuchung von Transport- und Mischungsprozessen, sowie von Abläufen chemischer Reaktionen in der Atmosphäre. Beispielsweise kann die Messung von Emissionen von Punktquellen atmosphärischer Spurenstoffe durch die Anwendung bildgebender Messmethoden deutlich verbessert werden. Die SO<sub>2</sub> Kamera wird als bildgebende Messtechnik bereits an Vulkanen verwendet. Das Messprinzip hat allerdings große Querempfindlichkeiten die zu bedeutenden Unsicherheiten in der Messung führen können.

In dieser Arbeit wurde eine Messtechnik vorgestellt, in der ein Fabry-Pérot Interferometer (FPI) verwendet wird. Die Transmissionseigenschaften des FPIs werden an die charakteristischen Absorptionsstrukturen eines Moleküls angepasst, um dieses nachzuweisen und zu quantifizieren.

Anhand des Beispiels von Schwefeldioxid (SO<sub>2</sub>) wurde eine Modellstudie durchgeführt. Zum Nachweis der Umsetzbarkeit wurde weiterhin ein Prototyp einer Ein-Pixel FPI Kamera gebaut. Die SO<sub>2</sub> Nachweisgrenze dieses Prototyps liegt bei  $\sim 8.5 \cdot 10^{16}$  molec cm<sup>-2</sup> oder 34 ppm m für 1 s Messzeit. Es konnte gezeigt werden, dass im Vergleich zur SO<sub>2</sub> Kamera die Querempfindlichkeiten der FPI Messtechnik bezüglich Ozon, Wolken und Aerosolextinktion bedeutend kleiner sind. Schließlich wurden mehrere Umsetzungen der Messmethode in schnellen bildgebenden Messinstrumenten vorgeschlagen und diskutiert.

# Contents

<b>1</b>	<b>Introduction</b>	<b>1</b>
<b>2</b>	<b>Theoretical background</b>	<b>3</b>
2.1	Absorption spectroscopy in the atmosphere . . . . .	3
2.1.1	Absorption spectroscopy . . . . .	3
2.1.2	Radiative transport in the atmosphere . . . . .	6
2.2	Imaging of trace gases in the atmosphere . . . . .	10
2.2.1	Differential Optical Absorption Spectroscopy . . . . .	11
2.2.2	SO <sub>2</sub> Camera . . . . .	12
2.2.3	Gas Correlation Spectroscopy . . . . .	14
2.3	Gas detection with a Fabry-Pérot interferometer . . . . .	15
2.3.1	The Fabry-Pérot interferometer . . . . .	15
2.3.2	The Fabry-Pérot interferometer in atmospheric remote sensing	20
<b>3</b>	<b>Model study</b>	<b>23</b>
3.1	The FPI instrument model . . . . .	23
3.1.1	The FPI transmission spectrum . . . . .	23
3.1.2	The bandpass filter transmission spectrum . . . . .	26
3.1.3	Simulation of the instrument response . . . . .	27
3.1.4	Signal to noise ratio . . . . .	28
3.2	Model results for FPI based SO <sub>2</sub> measurements in the UV . . . . .	28
3.2.1	Properties and optimum parameters of a UV FPI SO <sub>2</sub> measurement . . . . .	28
3.2.2	Comparison to the SO <sub>2</sub> Camera . . . . .	34
3.2.3	FPI imaging issues . . . . .	37
<b>4</b>	<b>Proof of concept study - The one pixel FPI SO<sub>2</sub> device</b>	<b>40</b>
4.1	OP FPI SO <sub>2</sub> device - instrument setup . . . . .	40
4.1.1	The realistic Fabry-Perot interferometer . . . . .	40
4.1.2	The optical setup . . . . .	44
4.1.3	The one pixel detector . . . . .	46
4.1.4	The combined instrument setup . . . . .	48
4.2	OP FPI SO <sub>2</sub> device - performance . . . . .	50
4.2.1	Noise . . . . .	50
4.2.2	SO <sub>2</sub> sensitivity . . . . .	57
4.2.3	Stability . . . . .	61
4.2.4	Improvement suggestions . . . . .	63

4.2.5	Conclusion . . . . .	64
<b>5</b>	<b>FPI imaging applications</b>	<b>65</b>
5.1	Scanning OP FPI device . . . . .	65
5.2	Parallelized beam . . . . .	66
5.2.1	Tilt tuning . . . . .	66
5.2.2	Pressure tuning . . . . .	68
5.2.3	Aperture tuning . . . . .	68
5.3	Rings (no parallelization) . . . . .	70
5.3.1	Tilt tuning . . . . .	70
5.3.2	Pressure tuning . . . . .	70
5.3.3	Windowing . . . . .	70
5.4	Summary . . . . .	75
<b>6</b>	<b>Conclusions and Outlook</b>	<b>77</b>
	<b>Bibliography</b>	<b>80</b>



# 1 Introduction

Earth's atmosphere mainly consists of nitrogen and oxygen molecules that are stable under the given conditions. So called trace gases are present in low quantities and cause or influence a multitude of atmospheric processes of crucial importance, like the green house effect or shielding of high energy radiation. Quantifying trace gases in the atmosphere is important for investigating atmospheric processes.

One method to detect trace gas species in the atmosphere is optical absorption spectroscopy. Known characteristic spectral absorption features can be used to identify and quantify the trace gas species by radiance measurements. With this method, remote sensing measurements can be performed directly in the atmosphere. This is applied since decades in several different techniques (e.g. [Moffat and Millan, 1971](#); [Platt et al., 1979](#)).

Sources of atmospheric trace gases are particularly interesting, since they can have large influences on atmospheric processes. Besides carbon dioxide and water vapor, many volcanoes permanently emit large amounts of sulfur dioxide (SO<sub>2</sub>) (e.g. [Textor et al., 2004](#)). SO<sub>2</sub> can be measured by optical remote sensing, since it has strong and differential absorption structures in the ultraviolet wavelength range. Moreover, it has a lifetime of the order of days in the free atmosphere (e.g. [Beirle et al., 2014](#)). Thus, it can be detected even at larger distances from the crater, and the atmospheric SO<sub>2</sub> background concentrations are very low. The large amounts of water vapor and carbon dioxide emitted by volcanoes are much more complex to quantify with remote sensing techniques, since they have to be separated from their high (for water vapor also a highly variable) atmospheric background signals. Volcanic SO<sub>2</sub> emissions, especially when injected in higher altitudes, can have a significant impact on climate. Sulfate aerosol can be formed and directly backscatter sunlight, or serve as cloud condensation nuclei. For instance, this has been observed for the eruption of Mt. Pinatubo in 1991 ([Robock, 2000](#)). Moreover, the SO<sub>2</sub> emission flux is used as an indicator for volcanic activity and magma dynamics (e.g. [Olmos et al., 2007](#); [Malinconico, 1979](#)).

Today, the Differential Optical Absorption Spectroscopy (DOAS) technique ([Platt and Stutz, 2008](#)) is routinely employed for volcanic SO<sub>2</sub> emission flux monitoring ([Galle et al., 2010](#)). Scanning telescopes and compact spectrometers are used to record radiance spectra from plume cross sections whose SO<sub>2</sub> content is evaluated. SO<sub>2</sub> emission fluxes can be inferred from additional wind velocity estimates. The time resolution of this method is of the order of minutes.

Fast imaging remote sensing measurements are highly desirable in atmospheric chemistry and physics. Chemical dynamics, mixing and transport processes can directly be assessed with high time resolution. One imaging method, the SO<sub>2</sub> Camera (Bluth et al., 2007; Mori and Burton, 2006; Kern et al., 2010; Lübcke et al., 2013), is frequently used for measuring volcanic SO<sub>2</sub> fluxes. It makes use of strong SO<sub>2</sub> absorption features in the UV and uses a simplified detection principle that commonly employs one or two interference filters. Thereby, it is able to record two dimensional SO<sub>2</sub> distributions with a time resolution of the order of Hz. This imaging measurements allow the determination of volcanic SO<sub>2</sub> emission fluxes with a much higher time resolution than DOAS measurements. Moreover, the plume propagation velocity can be directly determined from series of images.

However, the SO<sub>2</sub> Camera has relatively high cross interferences with volcanic plume aerosol and is limited by the variability of the ozone background. Moreover, clear sky conditions are required.

In this thesis, a novel concept for a trace gas imaging technique is investigated. A Fabry-Pérot interferometer with its transmission features matched to differential molecule absorption structures is employed. A high selectivity for single species can be reached, without dispersively recording spectral radiances (as e.g. the DOAS technique). Hence, the application in a fast imaging measurement is possible. In this thesis, the technique is to a large extent examined for SO<sub>2</sub> measurements in the UV. Thus, it could be directly compared to the existing SO<sub>2</sub> Camera technique.

In Chap. 2, the theoretical background for the thesis is outlined. A basic explanation of atmospheric absorption spectroscopy is given, focusing on the ultraviolet to visible wavelength range. Existing remote sensing techniques are briefly discussed, before introducing the theory of the Fabry-Pérot interferometer and its application to atmospheric remote sensing. The developed model of the FPI is described in Chap. 3. It is used to determine optimized instrument parameters and to predict the approximate performance of the technique. In particular, the sensitivity towards SO<sub>2</sub> and cross interferences with ozone and aerosol were investigated. In a proof of concept study a one pixel prototype of a Fabry-Pérot interferometer based SO<sub>2</sub> Camera was built. In Chap. 4, the instrument setup is presented and test measurements are shown and discussed in order to evaluate its performance. Finally, in Chap. 5, different possibilities to implement the FPI technique in a fast imaging scheme are presented. The methods are briefly described and their advantages as well as their feasibility are discussed.

## 2 Theoretical background

The objective of this thesis is to assess the feasibility of employing a Fabry-Perot Interferometer (FPI) to atmospheric remote sensing, particularly to volcanic SO<sub>2</sub> imaging in the UV wavelength range.

Absorption spectroscopy is the underlying concept of atmospheric trace gas remote sensing in the ultraviolet and visible (UV-VIS) wavelength range. In Sect. 2.1 absorption spectroscopy and its application in the atmosphere are introduced.

In Sect. 2.2 the concept of imaging of volcanic (or other trace gas) plumes is described. Imaging is the extension of a trace gas remote sensing principle to the retrieval of spatially resolved information in two dimensions. Already applied techniques are briefly presented in order to be able to compare them with the FPI imaging method in later chapters.

In the last part of this chapter (Sect. 2.3) the FPI theory and the principle of applying the FPI to atmospheric remote sensing is described. The similarity between FPI spectral characteristics and regularly spaced molecule absorption bands is exploited. Earlier, FPIs were used to study molecular absorption spectra in the laboratory (e.g. [Barrett and Myers, 1971](#)) before they were already applied to atmospheric remote sensing in the infrared (IR) by e.g. [Wilson et al. \(2007\)](#). Moreover, even FPI imaging schemes already were built (e.g. [Pisani and Zucco, 2009](#)). This thesis focuses on UV applications and especially volcanic trace gas imaging. This is a novel field of FPI applications.

### 2.1 Absorption spectroscopy in the atmosphere

This section will introduce the principle of absorption spectroscopy (Sect. 2.1.1). In the atmosphere, radiative transfer in the UV-VIS is strongly influenced by the scattering of light at particles. This has to be accounted for in atmospheric remote sensing and is therefore briefly outlined in Sect. 2.1.2. A more comprehensive treatment of the topic can be found e.g. in [Platt and Stutz \(2008\)](#).

#### 2.1.1 Absorption spectroscopy

The principle of absorption spectroscopy represents the basic concept that is used in this thesis. It exploits spectral characteristics of different substances in order to quantify and distinguish them. For molecules, these characteristics emerge from discrete energy states, determined by the molecular structure. Nuclear masses and internuclear binding potentials determine rotational and vibrational energy states of the molecules. The interaction of electrons with other electrons and the nuclei

account for the different electronic states of the molecule. Electronic states have energy separations from the ground state of the order of several eV, corresponding to visible up to UV wavelengths of electromagnetic radiation. Vibrational transitions lay in the infrared ( $E_{\text{vib}} \sim \frac{hc}{3\mu\text{m}} = 0.41\text{ eV}$ ) and rotational transitions in the far infrared to microwave region ( $E_{\text{rot}} \sim \frac{hc}{100\mu\text{m}} = 0.012\text{ eV}$ ). Combinations of these transitions, obeying transition rules from symmetry considerations, form the total energy spectrum of the molecule.

The initial distribution of the molecules within these energy states is determined by the temperature  $T$  via the Boltzmann factor. For room temperature ( $T = 300\text{ K}$ ) the probability of a single molecule to have the energy of a typical rotational state  $E_{\text{rot}} = \frac{hc}{100\mu\text{m}}$  and of a typical vibrational state  $E_{\text{vib}} = \frac{hc}{3\mu\text{m}}$  compared to the ground state  $E_g = 0$  are

$$\frac{p(E_{\text{rot}})}{p(0)} = \exp\left(-\frac{E_{\text{rot}}}{k_b \cdot T}\right) = 0.61 \quad (2.1)$$

$$\frac{p(E_{\text{vib}})}{p(0)} = \exp\left(-\frac{E_{\text{vib}}}{k_b \cdot T}\right) = 10^{-7} \quad (2.2)$$

The degeneracy of the states can increase this number by roughly an order of magnitude. This means, that mainly low rotational states and hardly any vibrational or electronic states are populated at room temperature. UV or VIS radiation that is resonant to the energy states of a present molecule species will therefore cause transitions from lower to higher energy states. This process is called absorption. The excited state is very short lived, since either the energy is lost by collision with other molecules or by isotropic reemission of a photon, or the molecule is dissociated. Absorption therefore leads to an extinction of a light beam traversing the absorbing medium. Due to the discrete energy states, absorption lines emerge in the spectrum. The gray line in Fig 2.1 shows the absorption spectrum of  $\text{SO}_2$ .

The extinction in an absorbing medium is described by Bouguer-Lambert-Beer's law. For each individual wavelength  $\lambda$  the relative change in intensity  $\frac{dI_\lambda}{I_\lambda}$  of the radiation having traversed an absorber of infinitesimal thickness  $dl$  with a number density  $\rho$  of an absorbing molecule species is given by:

$$\frac{dI_\lambda}{I_\lambda} = -\rho \sigma_\lambda dl \quad (2.3)$$

The spectral characteristics of the absorber is represented by the absorption cross section  $\sigma_\lambda$ . It represents the above explained absorption processes in dimensions of a geometrical cross section (commonly in  $\text{cm}^2$ ). Integration over an arbitrary light path  $s$  yields:

$$I_\lambda(s) = I_\lambda(0) \exp\left[-\int_0^s \sigma_\lambda \rho dl\right] \quad (2.4)$$

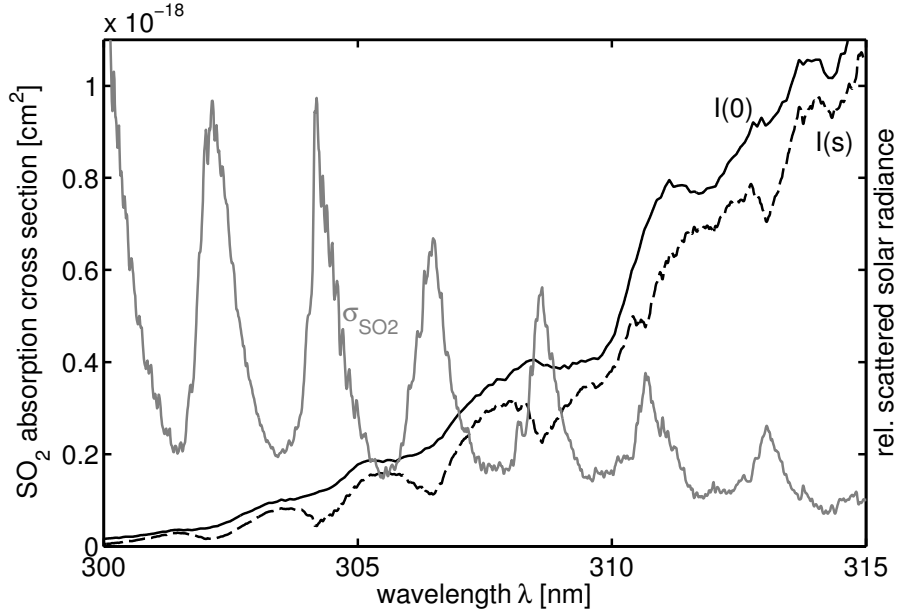


**Figure 2.1** – In gray, the  $\text{SO}_2$  absorption cross section is plotted. The black drawn line shows a typical spectrum of scattered solar radiation. The dashed line indicates the scattered solar radiation spectrum after an  $\text{SO}_2$  absorption by an  $\text{SO}_2$  CD of  $S_{\text{SO}_2} = 10^{18} \text{ molec cm}^{-2}$ .

The integral in the exponent is called optical density or extinction  $\tau$ . If  $\sigma_\lambda$  is independent of external conditions (e.g. temperature and pressure) that may change within the light path (mostly valid in the UV-VIS), Eq. 2.4 can be converted to:

$$\tau_\lambda = -\log \frac{I_\lambda(s)}{I_\lambda(0)} = \sigma_\lambda \int_0^s \rho \, dl = \sigma_\lambda S \quad (2.5)$$

$S$  is the integrated amount of absorbing molecules along the light path. It is called the column density (CD) of the absorber. Figure 2.1 shows the the spectral radiances  $I(0)$  and  $I(s)$  for scattered solar radiation and the extinction of an  $\text{SO}_2$  CD of  $10^{18} \text{ molec cm}^{-2}$ .

Absorption spectroscopy can for instance be used to determine the absorption cross sections  $\sigma_\lambda$  of gases. This can be done in the laboratory under controlled conditions with known gas concentrations and light paths.

With known cross sections, absorption spectroscopy can be used to detect and quantify gases in the environment via wavelength selective radiance measurements. The column density can be retrieved either by using the detailed cross section information of a gas or by calibration methods. In this thesis we will work with the latter application of absorption spectroscopy, applied in the free atmosphere.

## 2.1.2 Radiative transport in the atmosphere

When applying optical absorption spectroscopy in the free atmosphere one has to account for all the interactions of light with atmospheric particles. The atmosphere mainly consists of gas molecules but also contains non gaseous matter, referred to as aerosol. Both, gases and aerosol can absorb and scatter light, where scattering can be elastic or inelastic (e.g. [Roedel and Wagner, 2011](#)). The processes are briefly explained and the radiative transfer equation for UV-VIS radiation is introduced. Moreover, issues for the remote sensing application at volcanoes are outlined.

### Absorption

Gas molecules absorb radiation as explained in Sect. 2.1.1. In the atmosphere, the absorptions of all present gas species sum up. Aerosol can also cause an extinction due to absorption, e.g. by its physical cross section. Consider for instance a volcanic ash cloud. Compared to the narrowband absorption features of molecules, broadband absorption features are expected for aerosol particles.

### Elastic scattering

Mie theory describes the interaction of an electromagnetic plane wave with a spherical particle ([Mie, 1908](#)). Despite there is no analytical solution, it offers a basis to describe atmospheric scattering processes.

An important quantity is the size parameter  $x = \frac{2\pi r}{\lambda}$ . It links the particle's effective radius  $r$  to the wavelength  $\lambda$  of incoming light. The scattering efficiency  $Q$  describes the ratio of the effective scattering cross section  $\sigma_s$  of a particle to its geometrical cross section  $\sigma_{geo} \propto r^2$ . The phase function  $\Theta(\vartheta)$  determines the probability for the radiation to be scattered into the angle  $\vartheta$  towards the propagation direction of the incoming beam. For our considerations,  $Q$  and  $\Theta$  as a function of the size parameter contain sufficient information for the treatment of light scattering in the atmosphere.

An often used simplification of Mie theory is the Rayleigh approximation for particles that are small compared to the wavelength of incident radiation ( $x \ll 1$ ). Under this constraint the Mie solution becomes analytical and can be thought of as a dipole moment induced to the particles by the electromagnetic radiation.

The cross section  $\sigma_R$  of Rayleigh scattering is a function of  $\lambda^{-4}$ . The phase function is symmetric in  $\vartheta$ , meaning that the probabilities of forward and backward scattering are equal:

$$\sigma_R = \sigma_{R,0} \cdot \lambda^{-4}, \quad \Theta(\vartheta) = \frac{3}{4}(1 + \cos^2(\vartheta)) \quad (2.6)$$

Atmospheric molecules are typically much smaller than the wavelengths of UV and visible light. Therefore Rayleigh scattering is well suited for describing light scattering on air molecules. The air molecule's polarizability determines  $\sigma_{R,0} \approx$

$4.4 \cdot 10^{-16} \text{cm}^2 \text{nm}^4 \text{molec}^{-1}$  (Roedel and Wagner, 2011).

The size of aerosol particles, like cloud droplets, particulates emitted by combustion motors or volcanic ash can cover a range of several orders of magnitude. They commonly do not fulfill the  $x \ll 1$  criterion. The wavelength dependency of the scattering cross section is thus variable with particle size and the phase function gets asymmetric, preferring forward scattering. Generalizing, this process is referred to as Mie scattering.

For a given particle size distribution the aerosol extinction or aerosol optical density (AOD)  $\tau_{\text{Mie}} = \sigma_{\text{Mie}} S_{\text{aerosol}}$  of a Mie scatterer is parameterized by the Ångström parameterization:

$$\tau_{\text{Mie}}(\lambda) = \tau_{\text{Mie}}(\lambda_0) \left( \frac{\lambda}{\lambda_0} \right)^{-\gamma}, \quad (2.7)$$

with the Ångström exponent  $\gamma \in [0, 4]$ . Note, that  $\gamma$  is limited by the Rayleigh case. In volcanic plumes, an Ångström coefficient of 1.2 was found to be representative by Spinetti and Buongiorno (2007). However, volcanic plume aerosol contents can be highly variable, leading to complex Ångström coefficient distributions across the plume.

### Inelastic scattering

Most scattering events are elastic. The molecule, excited by the incident photon to a non resonant (often called virtual) electronic state, relaxes back to its initial state. It emits a photon with the same energy as the incident photon. In inelastic scattering events the excited molecule relaxes to a different vibrational or rotational state nearby the initial state. In this case, a photon with a different energy compared to the incident photon is emitted. This process is also called Raman scattering. The scattering efficiency for rotational Raman scattering is only about 2 – 4% (Roedel and Wagner, 2011) of the scattering efficiency of Rayleigh scattering. For vibrational Raman scattering it is even less ( $\sim 0.04\%$ , e.g. Lampel et al., 2015). In narrow structured spectra (as e.g. the Fraunhofer spectrum) inelastic scattering can lead to substantial distortion. The radiance at a Fraunhofer line wavelength of low intensity is enhanced by Raman scattered light from nearby wavelengths with high intensity, filling up the absorption line (Chance and Spurr, 1997). This is also referred to as the Ring effect (Grainger and Ring, 1962).

### Radiative transfer and volcanic trace gas measurements in the UV-VIS

The radiance of sunlight reaching an observer on the ground has undergone absorption and scattering on aerosol particles and gas molecules. The radiance in a light path of narrow solid angle  $\omega$  gets attenuated by absorption and scattering of light out of this path. However, light can also be scattered into this light path, enhancing the observed radiance. These processes dominate radiative transfer in the UV-VIS

and can be formulated in the so called radiative transfer equation. Thermal emission can be neglected for the regarded wavelength range. A change in radiance  $I$  within a small light path segment  $ds$  of a narrow light beam (or a narrow viewing solid angle) can be described for each wavelength by:

$$\frac{dI_\omega}{ds} = -(\tau_a + \tau_s) \cdot I_\omega + \tau_s \int_{4\pi} I^*(\Omega') \cdot \Gamma(\Omega', \omega) d\Omega' \quad (2.8)$$

The first summand represents Boguere-Lambert-Beer's law (see above, Eq. 2.4) with added scattering extinction  $\tau_s = \tau_{\text{Mie}} + \tau_R$ . The second term accounts for photons scattered into the beam solid angle  $\omega$ . It is dependent on the radiance  $I^*$  arriving at the regarded beam volume and the scattering extinction  $\tau_s$ .  $\Gamma$  contains the scattering phase function information. Together with  $\tau_s$  it determines the fraction of  $I^*$ , by which  $I$  is enhanced.

Equation 2.8 is essential for all applications described in this thesis, especially since the measurement techniques mostly use scattered sunlight as light source. Hence, the radiative transfer equation determines the light source as well as the traversing process across the absorber. A useful measure for the separation of these two processes is the mean free path  $s_{ph,R}$  of a photon in the atmosphere where only Rayleigh scatterers are present.

$$s_{ph,R}(\lambda) = \frac{1}{\sigma_R(\lambda) \cdot \rho} = \frac{\lambda^4}{\sigma_{R,0} \cdot \rho} \quad (2.9)$$

The fraction  $1 - \frac{1}{e} \approx 0.63$  of all photons from a distance  $s_{ph,R}$  to a detector get scattered again. A crucial point is, that due to the  $\lambda^{-4}$  dependency of the Rayleigh scattering efficiency, this visibility range varies for instance by a factor of 7.7 from visible ( $s_{ph,R}(500 \text{ nm}) = 57 \text{ km}$ ) to UV ( $s_{ph,R}(300 \text{ nm}) = 7.4 \text{ km}$ ) wavelength.

The trace gas column density, measured with passive optical remote sensing, does not contain information about the light path. Accurate quantification of the trace gas amount (for instance in a volcanic trace gas emission flux measurement) is therefore complicated.

Figure 2.2 sketches a typical volcanic trace gas remote sensing scenario. The volcanic plume cross section is colored brown. The ideal light path describes scattering events of radiation (that has not traversed the plume) behind the plume, directly into the instrument's FOV. However, in reality several different light paths are possible.

Light can be scattered into the instrument FOV from molecules or aerosol in between plume and instrument. This radiation most likely does not carry any absorption information from the plume gases. It leads to an underestimation of the volcanic trace gas CDs. This effect is referred to as light dilution and, in everyday life, can be compared to the fading of colors of distant objects in the atmosphere.

Another issue for the measurement is multiple scattering of light inside the volcanic

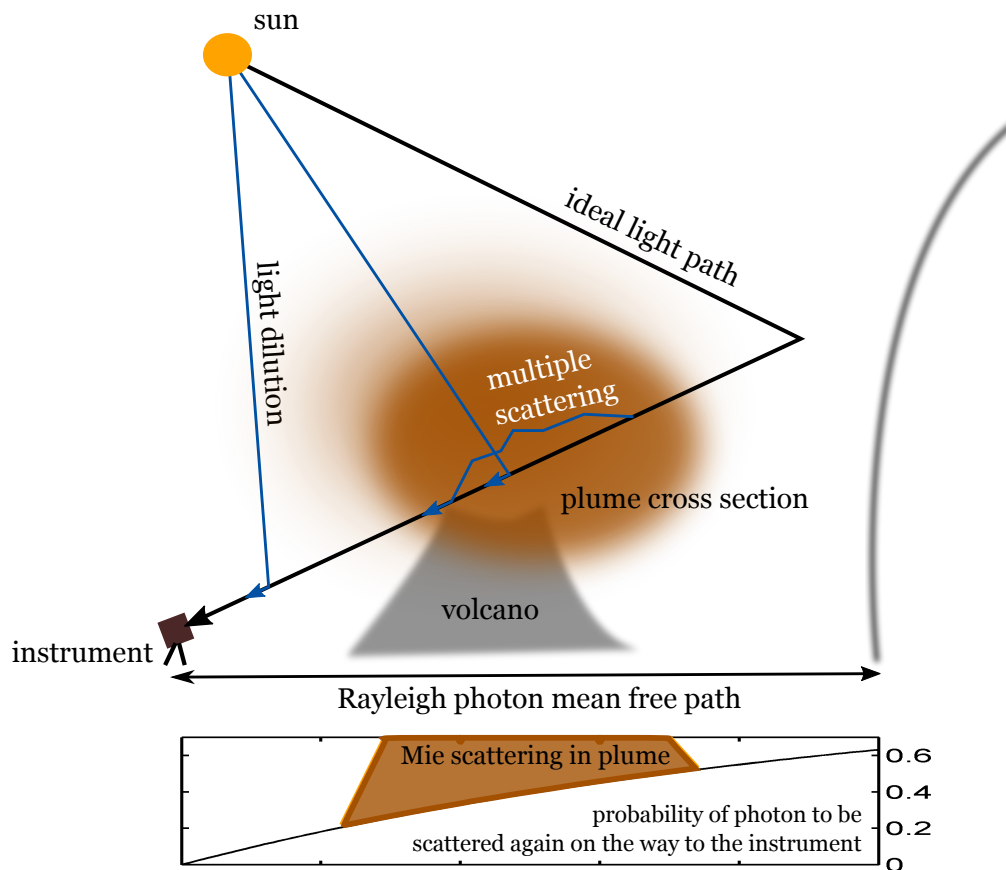


**Figure 2.2** – Sketch of a typical volcanic trace gas remote sensing scenario. The black line denotes the ideal light path typically assumed in data evaluation. The blue lines show several different possible light paths that impact the measurement’s accuracy. The faint gray line roughly indicates the Rayleigh photon mean free path, as an indicator of the instrument’s visibility range. In the panel below the sketch, the scattering probability of a photon on the way to the instrument is outlined.

plume. The enhanced aerosol abundances there drastically decrease the photon mean free path within the plume. Multiple scattering leads to increased light paths within the plume and therefore to overestimation of the volcanic trace gas CDs. All kinds of light paths and mixtures of multiple scattering and light dilution are possible. Current studies mostly suggest generalized corrections to recorded data (e.g. Kern et al., 2013). However, the high variability of aerosol in volcanic plumes as well as in the surrounding atmosphere makes the assessment of these issues complex.

In Figure 2.2 the Rayleigh photon mean free path  $s_{ph,R}$  is indicated in the measurement geometry. In the panel below the drawing, the probability of a photon to be Rayleigh scattered on the way to the instrument is plotted as a function of the distance to the instrument. The photon mean free path in a volcanic plume containing aerosol is often drastically reduced. The thus increased scattering probability with

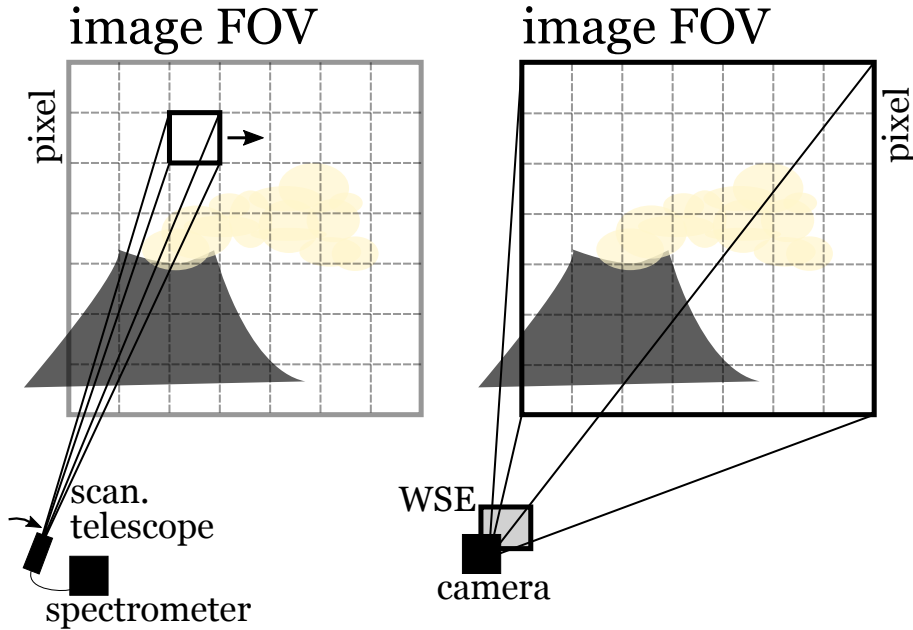


**Figure 2.3** – Dispersive imaging techniques require scanning schemes (left panel), whereas nondispersive detection methods can be implemented in full frame imaging schemes (right panel). Wavelength selective elements (WSE) can be placed in the light paths of cameras.

principally unknown characteristics within the plume is marked in brown.  $s_{\text{ph,R}}$  increases with the instruments elevation angle because of decreasing pressure. This figure suggests to avoid large distances between instrument and plume, since e.g. for 300 nm and atmospheric standard pressure and temperature,  $s_{\text{ph,R}}$  is only  $\sim 7.4$  km.

## 2.2 Imaging of trace gases in the atmosphere

Spatially and temporally resolved remote sensing (i.e. imaging) measurements of trace gases in the atmosphere are highly desired in atmospheric physics and chemistry. They allow the direct assessment of chemical dynamics, transport and dilution processes in the atmosphere.

The different imaging approaches can be categorized by their acquisition technique for wavelength information and their acquisition technique for spatial information (in two dimensions).

An image consists of spatial pixels  $\{i, j\}$  that cover the image field of view (FOV) with their respective pixel FOVs. Each pixel will measure radiances  $I^{\{i,j\}}$  that can be processed to a trace gas dependent instrument response  $R^{\{i,j\}}$ , that is either directly the trace gas column density  $S^{\{i,j\}}$  or can be linked to  $S^{\{i,j\}}$  via calibration. Techniques, where the incoming radiation of a pixel FOV is mapped to a spatial dimension of the detector in order to get wavelength information (e.g. grating or prism spectrometer), are referred to as dispersive. In contrast, nondispersive techniques use wavelength selective elements (WSE, e.g. filters, etc.) that can be placed

in front of the detector in a way that one pixel FOV is mapped to a single detector pixel. Spectral information is mostly gained via tuning the WSE.

Since one spatial dimension is lost in dispersive methods due to conversion into a wavelength dimension, only scanning across the image FOV yields a full frame image. With nondispersive techniques it is in general possible to implement full frame cameras. Once the WSE is placed in front of a two dimensional detector the spatial information is increased by the number of detector pixels (see Fig. 2.3).

For both, dispersive and nondispersive methods, the acquisition time per image frame with a given signal to noise ratio (SNR)  $t_{\text{frame}}$  is limited by the instrument's light throughput. The light throughput for dispersive measurements is limited the spectral resolution (for grating spectrometers to a large extent determined by the entrance slit). The WSEs of nondispersive techniques can in principle have arbitrarily large effective apertures and therefore higher light throughputs.

For dispersive techniques,  $t_{\text{frame}}$  is additionally limited by the spatial scanning process. nondispersive methods are limited by the WSE's tuning properties, and the intended spectral information per pixel (e.g. determined by the number of tuning steps).

Roughly speaking, there is a tradeoff between spectral and spatial (or/and temporal) resolution of the imaging measurement that has to be made according to the intention of the measurement. Different imaging remote sensing methods are briefly introduced in the following.

### 2.2.1 Differential Optical Absorption Spectroscopy

Differential Optical Absorption Spectroscopy (DOAS, e.g. [Platt and Stutz, 2008](#)) is the underlying principle of separating narrowband (differential) absorption features from broadband spectral contributions. Most of the following techniques use this principle in some way. However, with the term DOAS technique I will always refer to the dispersive DOAS measurements introduced in this subsection.

The DOAS technique is a dispersive technique for remote sensing of atmospheric trace gases. Distinct narrowband structures of molecules are identified in recorded optical density spectra, obtained from spectral radiance measurements. Known narrowband absorption cross sections of the molecules are used in a fitting routine, where all broadband effects are accounted for by a polynomial.

The gases narrowband (with respect to the analyzed wavelength range) absorption cross sections  $\sigma'_i$  can be separated from the broadband part  $\sigma_{b,i}$  for every molecule species  $i$ :

$$\sigma_i(\lambda) = \sigma'_i(\lambda) + \sigma_{b,i}(\lambda) \quad (2.10)$$

The optical density from a measured spectrum  $I(\lambda)$  related to a reference  $I_0(\lambda)$  can

be written as:

$$\tau(\lambda) = -\log \frac{I(\lambda)}{I_0(\lambda)} = \tau_R(\lambda) + \tau_{\text{Mie}}(\lambda) \quad (2.11)$$

$$+ \sum_i \sigma_{b,i}(\lambda) S_i + \sum_i \sigma'_i(\lambda) S_i \quad (2.12)$$

The first three contributors are broadband compared to the last one. A polynomial fit can be used to define  $I'_0(\lambda)$ , which differs from  $I_0(\lambda)$  by the broadband contributions. This allows to determine the narrowband optical density:

$$\tau'(\lambda) = -\log \frac{I(\lambda)}{I'_0(\lambda)} = \sum_i \sigma'_i(\lambda) S_i \quad (2.13)$$

Via fitting the known  $\sigma'_i(\lambda)$  to the measured  $\tau'(\lambda)$ , the  $S_i$  can be obtained as fit coefficients.

This method uses a very high spectral information content that allows the simultaneous measurement of several gas species. Moreover, radiative transfer effects principally can be accounted for. For instance, the impact of the Ring effect can be calculated from the reference spectrum. Moreover, approximations for the light path can be made by exploiting the absorption bands of the oxygen collision complex  $\text{O}_4$  (e.g. [Wagner et al., 2004](#)).  $\text{O}_4$  is abundant in the atmosphere in a constant amount dependent on temperature, pressure and  $\text{O}_2$  that, itself, has no narrowband absorption within the typically regarded wavelength ranges in the UV.

As explained above, this dispersive method can only record two dimensional spatial information via scanning. Scanning DOAS schemes are called imaging DOAS (IDOAS, e.g. [Lohberger et al., 2004](#)) and can be implemented in two ways. In the whisk broom scanning approach, light from a single viewing direction is collected with a telescope and the two spatial directions are scanned. In the push broom scanning approach, a 2d detector is used, where, with special optics, one spatial detector dimension is used for wavelength information and the other for one spatial dimension. The remaining spatial dimension is scanned.

In the whisk broom scanning approach a second detector dimension can be used to increase the light throughput per wavelength channel. Therefore, the two approaches mainly differ in their technical implementation, rather than the time needed to acquire a complete image.

### 2.2.2 $\text{SO}_2$ Camera

The  $\text{SO}_2$  Camera is a nondispersive remote sensing method for  $\text{SO}_2$  using very limited spectral information. The measurements have, however, a high spatial and temporal resolution ( $t_{\text{frame}} \approx 1\text{s}$ ). A bandpass filter transmitting in the UV at  $\sim 310\text{nm}$  (filter A with transmittance spectrum  $T_A$ ,  $\text{FWHM} \approx 10\text{nm}$ , see Fig. 2.4) is employed. In this wavelength region,  $\text{SO}_2$  and ozone are typically the dominant

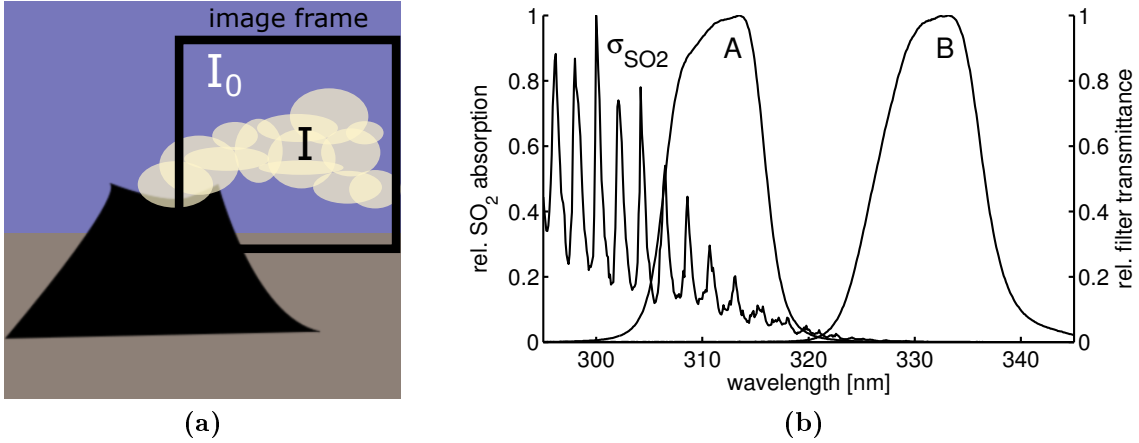


**Figure 2.4** – (a) Typical image frame of an SO<sub>2</sub> Camera.  $I_0$  and  $I$  can be derived from one acquisition. (b) SO<sub>2</sub> absorption cross section with the the transmission spectra of the two SO<sub>2</sub> Camera filters.

gaseous atmospheric absorbers. In the free atmosphere, SO<sub>2</sub> has a lifetime of the order of hours or days. Since globally there are only a few spread strong point sources (industrial sources and volcanoes), the atmospheric background concentration is very low. In contrast, ozone has a comparably high and steady atmospheric abundance (mainly in the stratosphere). Compared to the acquisition time of an SO<sub>2</sub> Camera image it varies only by small fractions on relatively long timescales. The SO<sub>2</sub> Camera is therefore able to quantify SO<sub>2</sub> CDs ( $S_{\text{SO}_2}$ ) at point sources via the optical density in filter A's range:

$$\tau_A = -\log \frac{I_A}{I_{A,0}} = \frac{\int d\lambda I(\lambda) T_A(\lambda)}{\int d\lambda I_0(\lambda) T_A(\lambda)} \propto S_{\text{SO}_2} \quad (2.14)$$

$I_0(\lambda)$  is the background spectral radiance.  $I(\lambda)$  is the spectral radiance of light that additionally traversed the point source's plume and therefore contains the SO<sub>2</sub> imprint. The background radiance  $I_{A,0}$  can be acquired by recording an image with another viewing direction in an SO<sub>2</sub> free FOV, or by the radiance of a plume free region within the measurement FOV (see Figure 2.4).

The background and plume measurement oftentimes have a different aerosol content, since commonly there are for instance more ash and condensate particles in volcanic plumes than in the surrounding atmosphere. These lead to an additional extinction. Therefore, a second filter (filter B) is used, transmitting at around 330nm, where the SO<sub>2</sub> absorption is more than an order of magnitude smaller. The aerosol extinction, due to its broadband characteristics, is considered to be constant within the 20nm spectral separation of filter A and filter B. This allows the correction of the aerosol contribution to the instrument's SO<sub>2</sub> signal. The SO<sub>2</sub> signal or the

instrument response of the SO<sub>2</sub> Camera is called apparent absorbance (AA):

$$AA = \tau_A - \tau_B = -\log \frac{I_A I_{B,0}}{I_{A,0} I_B} = (\tilde{\sigma}_{A,\text{SO}_2} - \tilde{\sigma}_{B,\text{SO}_2}) S_{\text{SO}_2} \quad (2.15)$$

$\tilde{\sigma}_{i,\text{SO}_2}$  are the radiance weighted SO<sub>2</sub> cross sections averaged over the respective filter wavelength range. Since especially the radiance weighting varies for different measurement conditions, calibration is required. An additional DOAS measurement with a narrow FOV within the SO<sub>2</sub> Camera's FOV (Lübcke et al., 2013; Kern et al., 2010) is commonly chosen over calibration cell methods that were used earlier.

The ozone background CD changes with daytime, mainly due to a varying solar zenith angle (SZA). This means that the changes in the spectral radiance induced by ozone, within the time period between plume and reference measurement, are interpreted as SO<sub>2</sub>. However, due to the high spatial information content, there is almost always a background spot (with no plume) in the image that can be used for a real time ozone correction. The ozone correction across the whole FOV can only roughly be done by a measurement looking in a different SO<sub>2</sub> free direction. At many volcanoes the SO<sub>2</sub> emissions, and therefore the SO<sub>2</sub> optical densities, are very high. Hence, the SO<sub>2</sub> absorption signals at those volcanoes dominate the distortion of remaining ozone uncertainty.

The wavelength dependency of the scattering efficiency (see Sect. 2.1.2) can cause an aerosol interference, once the aerosol optical density (AOD) changes significantly within the separation of the two filters. This is especially the case for small aerosol particles. In first order, for low AODs this leads to a wavelength dependent aerosol extinction that is interpreted as SO<sub>2</sub> by the SO<sub>2</sub> Camera. This kind of aerosol interference is difficult to correct, since the aerosol content and composition can vary strongly within the plume. The DOAS calibration is able to correct for it to some extent, in cases of homogeneous aerosol type distributions. For higher AODs, multiple scattering will influence the light path in the absorber. This is a general problem for volcanic remote sensing (see Sect. 2.1.2).

### 2.2.3 Gas Correlation Spectroscopy

Gas correlation spectroscopy (GCS) is a nondispersive technique that can be employed for gases with strong differential absorption structures. Radiance measurements of light that traversed the absorbing gas are recorded with a varying amount of the same gas, artificially added within the camera's optical path. This means, that the WSE can be a gas cell containing a certain amount of absorber that is consecutively moved in and out the light path. Via prefiltering, a wavelength region  $\Delta\lambda$  has to be isolated, where the absorber's absorption is strongly differential (for UV SO<sub>2</sub> measurements e.g. filter A of the SO<sub>2</sub> Camera). For an atmospheric absorber optical density  $\tau_{i,atm}$  and an absorber optical density  $\tau_{i,cell}$  in the gas cell the

radiance  $I$  without and  $I_{cell}$  with gas cell are compared in their ratio  $R_{gcs}$ :

$$R_{gcs} = \frac{I_{cell}}{I} = \frac{\int d\lambda I_0(\lambda) \exp(-\tau_{i,atm}(\lambda) - \tau_{i,cell}(\lambda))}{\int d\lambda I_0(\lambda) \exp(-\tau_{i,atm}(\lambda))} \quad (2.16)$$

$I_0(\lambda)$  is the spectral radiance of the scattered sunlight, without trace gas absorption. For a trace gas free atmosphere the extinction of the gas in the cell will determine the ratio  $R_{gcs,0}$ . This ratio is in principle constant for any broadband influence on  $I_0(\lambda)$  but also for narrowband absorption structures that do not correlate with the absorption structures of the gas to be measured. The gas in the cell strongly extincts light at the gas' absorption peaks. For an atmosphere containing this gas,  $R_{gcs}$  will be higher than  $R_{gcs,0}$ , since  $I(\lambda) = I_0(\lambda) \exp(-\tau_{i,atm}(\lambda))$  is already weakened, or even blocked, at the wavelength of strong gas cell absorption.

The GCS method uses more detailed spectral information than the SO<sub>2</sub> Camera. Therefore, reduced ozone and aerosol interferences are expected. Another advantage is, that the technical implementation of an imaging setup can be kept rather simple with, for instance, a bandpass filter and a movable gas cell. However, the gas has to fulfill certain conditions in order to be suited for GCS. It needs to have the above mentioned strong differential absorption structures. Broadband contributions (as observed in the SO<sub>2</sub> absorption) will significantly increase the total cell optical density without contributing to sensitivity, thus reducing the signal. Moreover, the gas needs to be chemically stable in order to maintain a constant cell optical density.

## 2.3 Gas detection with a Fabry-Pérot interferometer

In this section the principle of employing a Fabry-Pérot interferometer (FPI) in absorption spectroscopy is examined. Firstly, the FPI theory is explained. More comprehensive descriptions can be found e.g. in (Perot and Fabry, 1899; Demtröder, 2007). In Sect. 2.3.2 basic thoughts on applications of a FPI to trace gas remote sensing are introduced.

### 2.3.1 The Fabry-Pérot interferometer

When electromagnetic radiation of a radiance  $I_0$  reaches an interface of a changing refractive index  $n$ , it is split up in a reflected and a refracted (transmitted) part. This is described by Fresnel's reflection laws. The reflectivity  $R$  is a function of the difference  $\Delta n$  in refractive index and the incidence angle  $\beta$ . The transmission  $T = 1 - R - A$  is determined by the reflectivity and absorptivity  $A$ . In this study, the absorptivity is neglected, since the material used has vanishing absorption in the regarded wavelength range. The radiances of the resulting reflected and transmitted

partial beams  $I_r$  and  $I_t$  are related to the incident radiation  $I_0$  by:

$$I_r = R I_0 \quad (2.17)$$

$$I_t = T I_0 = (1 - R) I_0 \quad (2.18)$$

The dependence on the wavelength and the incidence angle of the incoming radiation is shown in Fig. 2.5. It is determined by the refractive index of fused silica and Fresnel's equations. Generally, these effects are rather broadband, especially for the incident angle range examined in this study with maximum incident angles of about  $10^\circ$ .

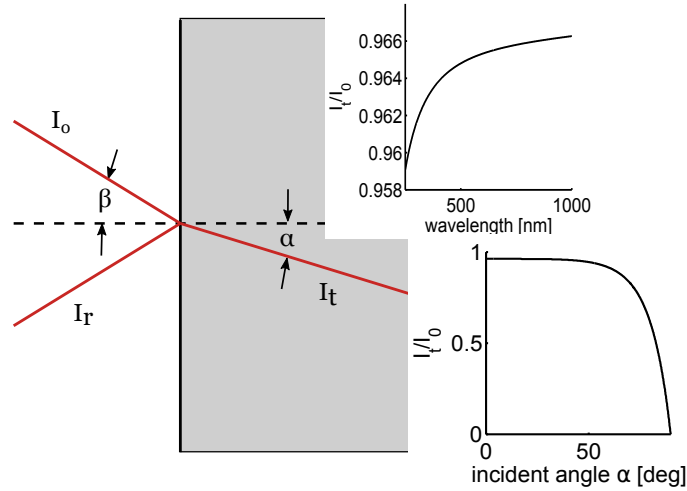


**Figure 2.5** – Reflection and refraction of a light beam at an interface of changing refractive index. The upper small panel sketches the wavelength dependency of the transmission due to the refractive index (refractive index according to [Kitamura et al., 2007](#)). The lower small panel shows the incidence angle dependency of the transmission.

If we now add a second, plane parallel reflective surface, the assessment of  $I_r$  and  $I_t$  becomes more complex. Radiation traversing the first surface gets partially reflected at the second and so on. Light bounces back and forth between the two surfaces, causing a multitude of transmitted and reflected partial beams with a constant difference in optical path (see Fig. 2.6). When overlapping spatially, these transmitted or reflected partial beams interfere and thereby cause characteristic transmittance and reflectance patterns. This setup is called Fabry-Perot interferometer (FPI). In the following  $d$  denotes the spatial separation of the two surfaces, and  $n$  the refractive index of the medium in between the two surfaces.  $\alpha$  will always be the angle between the propagation vector of the radiation within the two reflective surfaces and the surface normal.

The interference phenomenon can be assessed regarding an electromagnetic plane wave of amplitude  $|A_0| \propto \sqrt{I_0}$ , incident under an angle  $\beta$  onto the FPI (Fig. 2.6). The amplitudes of the partial beams reflected by the first surface ( $|A_i|$ ) transmitted

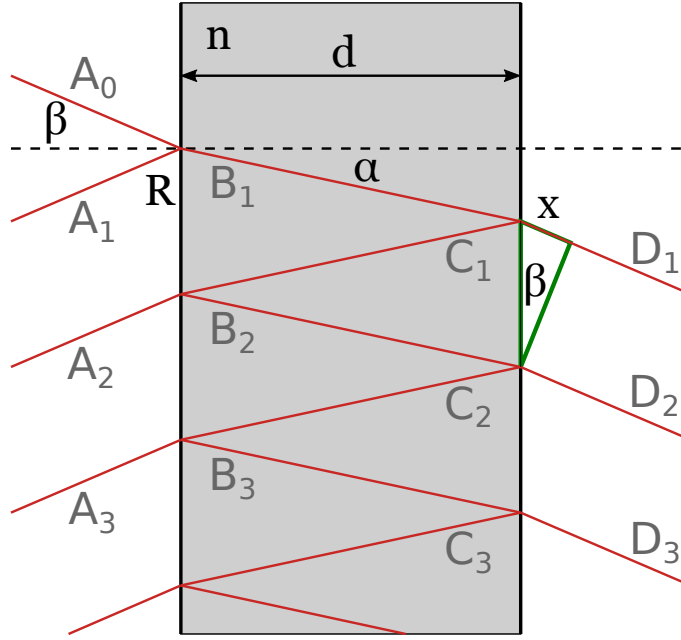


**Figure 2.6** – Light path of an incident light beam ( $A_0$ ) in an FPI. The light gets reflected back and forth in between the two reflective surfaces. The interference of transmitted and the reflected partial beams leads to the spectral characteristics of the FPI, dependent on surface displacement  $d$ , refractive index  $n$ , incidence angle  $\alpha$  and surface reflectivity  $R$ .

by the first surface ( $|B_i|$ ), reflected by the second surface ( $|C_i|$ ) and transmitted by the second surface ( $|D_i|$ ) are given by:

$$\begin{aligned}
 |A_1| &= \sqrt{R} |A_0| \\
 |B_1| &= \sqrt{R-1} |A_0| \\
 |C_1| &= \sqrt{R} |B_1| \\
 |D_1| &= \sqrt{R-1} |B_1| \\
 |A_2| &= \sqrt{R-1} |C_1| \\
 |B_2| &= \sqrt{R} |C_1| \\
 &\vdots
 \end{aligned}$$

Two consecutively transmitted or reflected partial beams (e.g.  $D_i$  and  $D_{i+1}$ ) then have an optical path length difference of

$$\Delta = 2 \frac{nd}{\cos \alpha} - x = 2nd \cos \alpha \quad \text{see Fig. 2.6.} \quad (2.19)$$

$\Delta$  and the phase jump  $\phi_r$  of reflections at the optically denser surfaces account for the total phase shift  $\delta$  of two consecutively transmitted or reflected beams:

$$\delta = \frac{2\pi \Delta}{\lambda} + \phi_r \quad (2.20)$$

All transmitted beams experience an even number of reflections that have no impact on the phase difference ( $\phi_r = 0$ ), whereas the reflected beams experience always an odd number of reflections ( $\phi_r = \pi$ ).

Summing up the reflected and transmitted partial beams with the right phase and squaring in order to again obtain intensities yields:

$$T_{FPI} = \frac{I_t}{I_0} = \frac{1}{1 + \tilde{F} \sin^2 \frac{\delta}{2}} \quad (2.21)$$

$$R_{FPI} = \frac{I_r}{I_0} = \frac{\tilde{F} \sin^2 \frac{\delta}{2}}{1 + \tilde{F} \sin^2 \frac{\delta}{2}} \quad (2.22)$$

with

$$\tilde{F} = \frac{4R}{(1 - R)^2} \quad (2.23)$$

Equations (2.21) and (2.22) are called Airy formulas and describe the transmission and reflection as a function of  $\delta$  and the so called finesse coefficient  $\tilde{F}$  (see Appendix X for detailed derivation). As expected from energy conservation, for negligible absorption  $T_{FPI} + R_{FPI} = 1$  holds for any given  $\delta$ . The peaks of total transmission, periodic in  $\delta$  are caused by constructive interference of the transmitted beams constraint by

$$\delta = 2\pi m \quad (2.24)$$

with the order  $m \in \mathbb{N}$ . For an increasing surface reflectivity  $R$  (and thus increasing  $\tilde{F}$ ), more and more partial beams effectively interfere. For a beam that got reflected  $2l$  times inside the FPI, the constraint to interfere constructively with the first beam is  $l\delta = 2\pi m$ . This means that if  $\frac{\delta}{2\pi}$  changes ever so little from an integer, a high  $l$  will be able to cause a partial beam with a phase shift  $l\delta$  that interferes destructively with the first transmitted partial beams, etc. Therefore, for higher  $\tilde{F}$ , the FPI transmission falls off more rapidly from the maximum and the pattern gets sharper. In Fig. 2.7  $T_{FPI}$  is shown as a function of  $\delta$  for different values of  $\tilde{F}$ .

For a set of instrument parameters  $\{d, n, \alpha, R\}$  the FPI behaves like a spectral filter that only transmits light of resonant frequency  $\nu$ . The spectral FPI transmission peaks are equidistant in frequency since  $\delta \propto \nu$ . We will however mainly work with the FPI transmission as a function of wavelength  $\lambda$ . Since  $\delta \propto \frac{1}{\lambda}$ , only for high orders  $m$  approximate periodicity is observed.

The FPI transmission spectrum can be characterized by two measures. The free spectral range (FSR) is defined as the separation of two transmission maxima. In phase units the FSR is always  $2\pi$ . In wavelength units, two neighboring transmission peaks are at  $\lambda_m$  and  $\lambda_{m+1}$ . The FSR  $\delta\lambda$  is then given by:

$$\delta\lambda = \lambda_m - \lambda_{m+1} = \frac{\Delta}{m} - \frac{\Delta}{m+1} = \frac{\Delta}{(m+1)m} \quad (2.25)$$

$$= \lambda_{m+1} \lambda_m \frac{1}{\Delta} \approx \frac{\lambda_m^2}{\Delta} \quad (2.26)$$

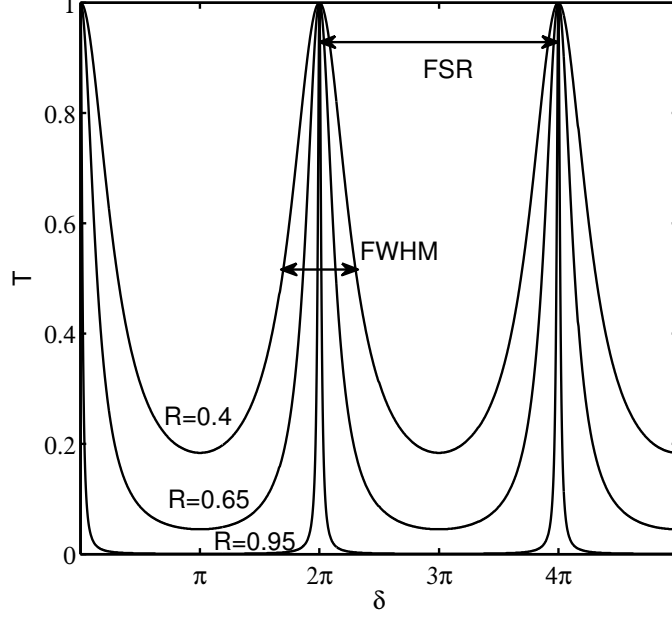


**Figure 2.7** – FPI transmittance as a function of the phase shift  $\delta$  of two consecutively transmitted partial beams. The FSR is dependent on the optical light path in between the two reflective surfaces. The ratio of FSR and FWHM of a transmittance peak is called finesse and determined by the reflectivity  $R$  of the surfaces.

In addition, the full width at half maximum (FWHM)  $\epsilon$  of a transmission peak can be derived from Eq. (2.21):

$$T_{FPI} \left( \frac{\epsilon}{2} \right) = \frac{1}{2} \Leftrightarrow \epsilon = 4 \arcsin \left( \frac{1}{\sqrt{\tilde{F}}} \right) = 4 \arcsin \left( \frac{1-R}{2\sqrt{R}} \right) \approx \frac{2(1-R)}{\sqrt{R}} \quad (2.27)$$

The approximation only holds for  $\tilde{F} \gg 1$  or  $R > 0.5$ . The FWHM in units of wavelength is  $f = \frac{2\pi\Delta}{\epsilon}$ . The ratio of FSR to FWHM is called finesse  $F$  and represents a measure for the number of interfering beams:

$$F = \frac{\delta\lambda}{f} = \frac{\lambda_m^2 \epsilon}{2\pi \Delta^2} = \frac{2\pi}{\epsilon} \approx \frac{\pi\sqrt{R}}{1-R} \quad (2.28)$$

For an ideal FPI, Eq. (2.28) fully describes the finesse as a function of the surface reflectivity  $R$  only. In reality, there are also other effects causing broadening of the transmission peaks, which can be for instance the roughness or misalignments of the reflective surfaces. To all these effects  $i$  a finesse  $F_i$  can be linked that sum up reciprocally to the total finesse of a setup:

$$\frac{1}{F_{tot}} = \sum \frac{1}{F_i} \quad (2.29)$$

The effect with the lowest finesse predominantly determines the transmission spectrum.

### 2.3.2 The Fabry-Pérot interferometer in atmospheric remote sensing

As introduced above, the FPI's spectral transmission profile  $T_{FPI}(\lambda)$  is determined by its instrument parameters  $\{d, n, \alpha, R\}$ . By varying the instrument parameters, the spectral transmission is also varied. Therefore, the FPI is suited for the employment as the WSE in a nondispersive remote sensing setup.

#### Shifting the FPI spectrum

In the precedent section, the characterization of the FPI by FSR and finesse was introduced. However, the FSR only states the spectral displacement of two FPI fringes, not their absolute position. The position  $\lambda_m$  of the transmission maxima with order  $m$  can be derived from the interference condition (see Eq. (2.24) and (2.20)):

$$\lambda_m = \frac{\Delta}{m} \quad (2.30)$$

When we relate the responses of the absolute fringe position  $\lambda_m$  and the FSR  $\delta\lambda$  (Eq. 2.26) to a small change of  $\Delta$ , we find that for high orders the shift of the spectra will dominate the change in FSR (stretch):

$$\frac{\text{shift}}{\text{stretch}} = \frac{\frac{d\lambda_m}{d\Delta}}{\frac{d\delta\lambda}{d\Delta}} = m + 1 \quad (2.31)$$

This is essential for the applications explained in the following. When using higher orders, small changes in the FPI parameters  $d$ ,  $n$  and  $\alpha$  allow us to shift the transmission spectrum, conserving the FSR in good approximation.

#### FPI trace gas detection principle

A possible application could be as follows: An FPI transmits in a prefiltered wavelength range with a single fringe of high order. The FSR of the FPI is as large as the prefiltered wavelength range. By continuously varying an FPI parameter the fringe is shifted across the range and a spectrum can be recorded (Fig. 2.8). The resolution would be limited by the finesse and the resolution of the tuning process. In comparison to a grating spectrometer the acquisition time per spectrum would be much higher, since each wavelength channel has to be recorded separately. On the other hand, one spectral acquisition can supply all image pixels at once, which is a substantial advantage for imaging.

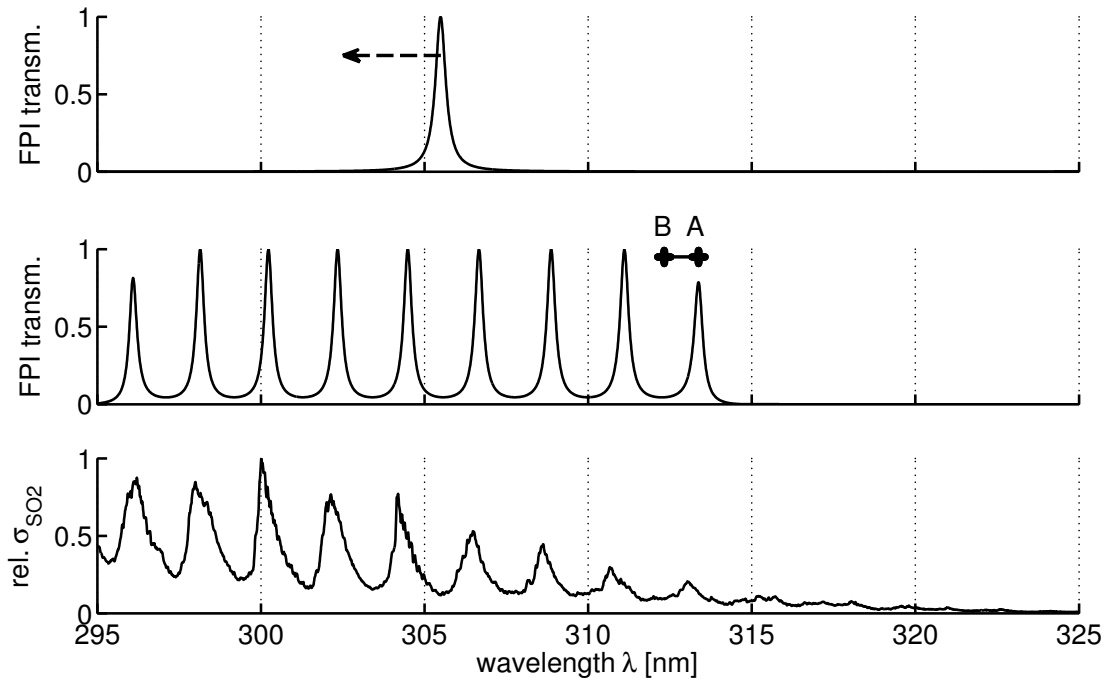


**Figure 2.8** – Two principles of applying an FPI to spectroscopy: In the upper panel an isolated FPI fringe (could also be a narrowband interference filter) is shown. It can be used to scan the whole spectrum. In the middle panel the method applied in this thesis is sketched. The FPI’s FSR is matched to the band structure in  $\text{SO}_2$  absorption. The lower panel shows the  $\text{SO}_2$  absorption spectrum.

This approach is in principle similar to the ‘tilted filter’ imaging method. A narrowband bandpass interference filter is tilted in front of a detector in order to gain wavelength information (applied for e.g.  $\text{NO}_2$  by [Benton, 2013](#)). A bandpass interference filter principally can be looked at as an overlay of several FPI layers. These layers react to a change in incidence angle (due to the tilt) with a shift of the transmission peak (e.g. [Pollack, 1966](#)).

In this thesis, the FPI is employed in a slightly different way. For many molecules one can identify approximately periodical spectral absorption features. Within the scope of the periodicity of the molecules’ absorption it is possible to match the FPI transmission pattern to molecule absorption band structures. That way, the FPI would be able to extract an extensive amount of molecule specific information from the spectra with only a few tuning steps. For instance an ‘on-line’ measurement (FPI transmits at several absorption peaks of the molecule) could simply be compared to an ‘off-line’ measurement (FPI transmits at molecule’s absorption minima). By this procedure, the spectral FPI transmission is only shifted by half the spectral distance of two absorption peaks in frequency. Therefore, structures chang-

ing on higher wavelength scales are effectively excluded from the measurement. On the one hand, this is an advantage, since it does not have to be extracted in an additional evaluation step (like in DOAS methods), on the other hand the broadband information will not be available for the assessment of e.g. radiative transfer influences.

The trace gas detection principle of an FPI instrument can for instance be similar to the SO<sub>2</sub> Camera principle. Instead of band pass filters, an FPI with its transmission spectrum matched to the narrowband SO<sub>2</sub> absorption bands is used. Via tuning, the comb shaped transmission of the FPI can be shifted between an on line setting ('setting A') and an off line setting ('setting B'). Accordingly, the instrument response or apparent absorbance seen by the FPI setup would be:

$$AA_{FPI} = \tau_{FPI,A} - \tau_{FPI,B} \quad (2.32)$$

The optical density  $\tau_{FPI,i}$  corresponds to the optical density observed through the FPI in setting  $i = A, B$ . Other forms of the instrument response are thinkable. The FPI apparent absorbance  $AA_{FPI}$  is used in the following, since it is ideally proportional to the trace gas CD. Moreover, it allows a straight forward comparison with the SO<sub>2</sub> Camera technique.

## 3 Model study

The subject of this chapter is the examination of FPI based SO<sub>2</sub> remote sensing in a model study. In Sect 3.1, the different model components are described and basic properties, especially of the FPI itself, are discussed. Then, optimal setup parameters, for the application to SO<sub>2</sub> in the UV, are determined, regarding signal to noise ratio (SNR) estimates. Moreover, in Sect. 3.2, the properties and the performance of the simulated setup is assessed and compared to existing imaging techniques. Finally, general issues of the application of an FPI in imaging setups are addressed.

Parts of this chapter are published in [Kuhn et al. \(2014\)](#).

### 3.1 The FPI instrument model

#### 3.1.1 The FPI transmission spectrum

An essential part of the model is to reproduce the FPI transmission spectrum  $T_{FPI}(\lambda)$ . In the experimental part of this thesis a so called 'air spaced' FPI was used. It consists of two plane parallel fused silica plates, where the inner surfaces of these plates are the active FPI reflective surfaces. Thus, the angle between optical axis and light propagation direction  $\alpha$  equals the incidence angle  $\beta$  onto the FPI. In the following, this angle is labeled as  $\alpha$ .

$T_{FPI}$  is given by the Airy function (Eq. (2.21)) as a function of the phase difference of two consecutively transmitted beams  $\delta(\Delta)$  (Eq. (2.20)) and the reflectivity  $R$ . The transmission spectrum as a function of wavelength is given by:

$$T_{FPI}(\lambda; d, n, \alpha, R) = \left[ 1 - \frac{4R(\lambda, \alpha)}{(1 - R(\lambda, \alpha))^2} \sin^2 \left( \frac{2\pi d n(\lambda) \cos \alpha}{\lambda} \right) \right]^{-1}, \quad (3.1)$$

where the expression for the finesse coefficient (Eq. (2.23)) was included. The refractive index  $n$  is a function of wavelength and the reflectivity  $R$  is also wavelength dependent and varies additionally with the incidence angle  $\alpha$ . However, the variations of  $R(\lambda, \alpha)$  and  $n(\lambda)$  are negligible, since we will only regard a comparably narrow wavelength window of typically less than 20 nm and the range of incidence angles will not exceed 20°.

In Fig. 3.1 the spectral FPI transmission is plotted for different surface displacements  $d \in \{5\mu m, 10\mu m, 25\mu m\}$  (colors) and reflectivities  $R \in \{0.65, 0.90\}$  ( $n = n_{air}$  and  $\alpha = 0$ ). As expected from the theoretical considerations of Sect. 2.3 we observe shorter FSR for increasing  $d$ . The finesse increases with the reflectivity  $R$ .

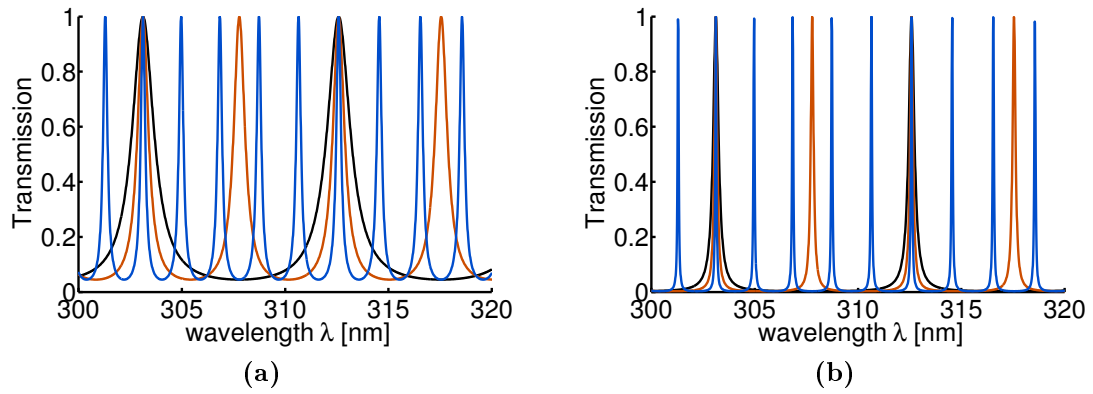


**Figure 3.1** – FPI transmittance spectrum for different FPI surface displacements  $d = \{5 \mu\text{m} \text{ (black)}, 10 \mu\text{m} \text{ (orange)}, 25 \mu\text{m} \text{ (blue)}\}$  and for different surface reflectivities  $R = 0.65$  (a) and  $R = 0.90$  (b). The finesse grows with  $R$ , the FSR shrinks with  $d$ .

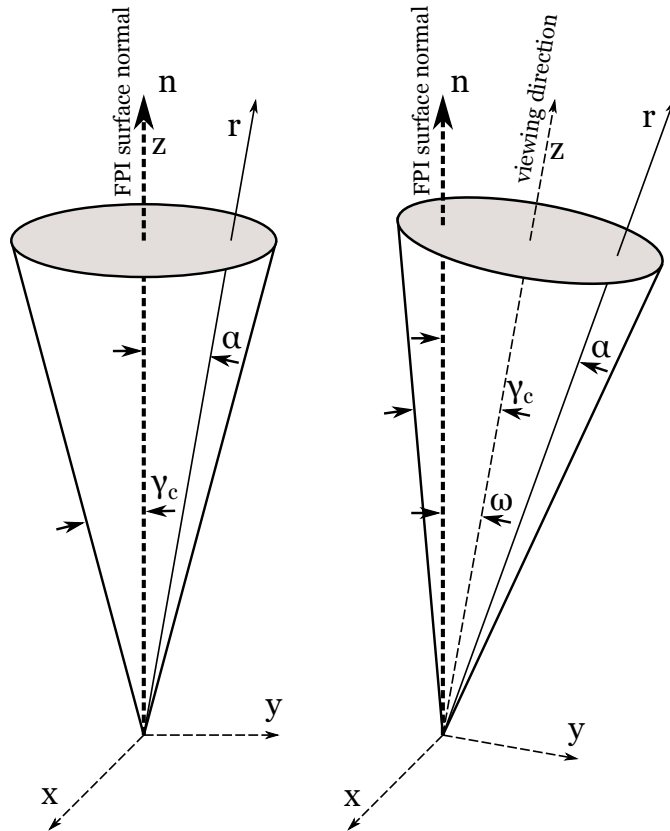


**Figure 3.2** – Light cones incident on the FPI surface with surface normal  $\vec{n}$ . On the left, the cone axis  $\vec{z}$  (or viewing direction) is parallel to the surface normal. The distribution of  $\alpha$  is obtained via integration over the polar coordinate  $\vartheta$ . On the right, the cone is tilted by  $\omega$  versus  $\vec{n}$ . In order to obtain the distribution of  $\alpha$ , the transformation  $\alpha(\omega; \vartheta, \varphi)$  is needed.

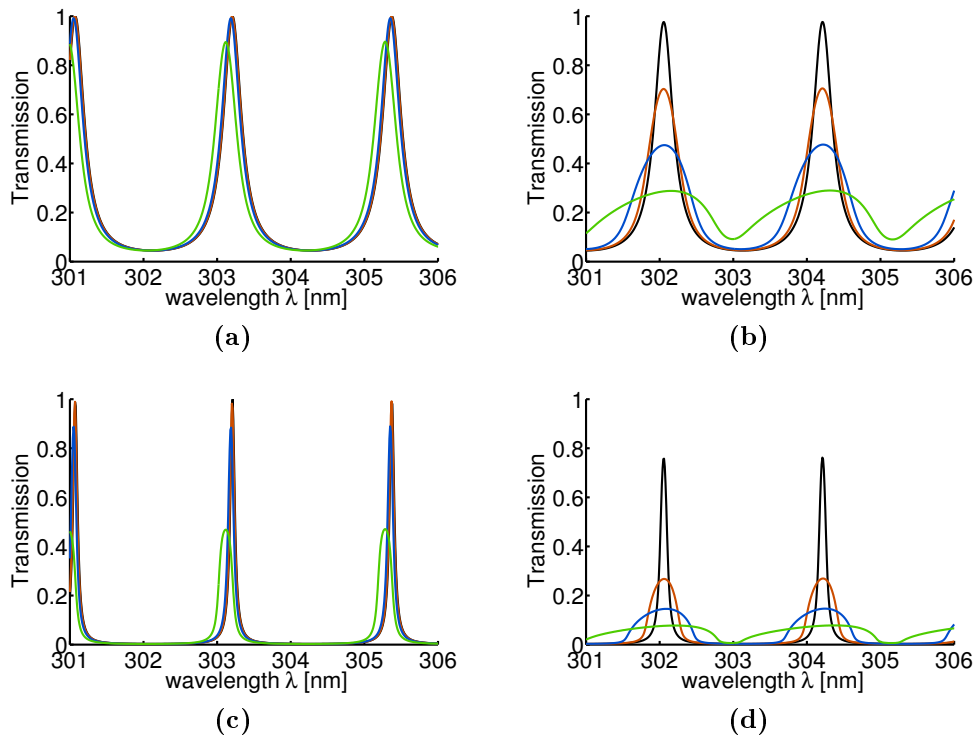


**Figure 3.3** – Effective FPI transmittance spectrum for light beams with cone angle  $\gamma_c = \{0.1^\circ$  (black),  $0.5^\circ$  (orange),  $1^\circ$  (blue),  $2^\circ$  (green) $\}$ , different reflectivities  $R = 0.65$  (a,b),  $R = 0.9$  (c,d), and different FPI tilt angles  $\omega = 0$  (a,c) and  $\omega = 5^\circ$  (b,d). For tilted FPIs the cone angle of incoming light leads to a higher blurring, since the FPI's incidence angle range increases. Sharper FPI transmission peaks (higher finesse for equal FSR) are affected more distinctly, since the shift of the FPI transmission peaks due to changing  $\alpha$  is the same for every finesse.

In reality, the incident light beam is always divergent. In this model, we assume the light beam to be cone shaped. The cone limits the FOV of the measurement. It will cover a range of angles  $[0, \gamma_c]$  measured from the cone axis. The angle distribution incident onto the FPI is then determined by all angles within the cone's solid angle (see Fig. 3.2). The effective FPI transmission  $T_{FPI}^{eff}(\lambda)$  for such a light cone is given by:

$$T_{FPI}^{eff}(\lambda; \gamma_c, \omega, d, n, R) = \frac{1}{N(\gamma_c)} \int_0^{2\pi} \int_0^{\gamma_c} T_{FPI}(\lambda; d, n, \alpha(\omega; \vartheta, \varphi), R) \sin \vartheta \, d\vartheta d\varphi \quad (3.2)$$

$\omega$  is the tilt angle and  $N(\gamma_c)$  is the normalization factor. We have to account for light cones that traverse the FPI under an tilt angle  $\omega$  towards the FPI surface normal (see Fig. 3.2). This is needed when the FPI is tuned by tilting or for the pixel wise assessment of an imaging implementation. For  $\omega \neq 0$  the transformation  $\alpha(\omega; \theta, \phi)$  gets more complex. It can be inferred from the scalar product of the vectors  $n$  and  $r$  in Fig. 3.2

The effective FPI transmission is a weighted average over the FPI transmissions of the contributing incidence angles  $\alpha$ . This leads to a blurring of the FPI transmission spectrum. In Fig 3.3,  $T_{FPI}^{eff}$  is shown for different geometries and different FPI finesses. The colors correspond to different light cone angles ( $\gamma_c \in [0.1, 0.5, 1, 2]^\circ$ ) or FOVs, respectively. The subplots show the transmission spectrum for a low and a high finesse FPI ( $R \in \{0.65, 0.90\}$ ), and for the cone tilt angles  $\omega \in \{0^\circ, 5^\circ\}$ .

For  $\omega = 0$  there is only a weak impact of the different FOV sizes, because the FPI transmission spectrum is a function of  $\cos \alpha$  that does not change much for small angles. The maximum incidence angle equals the cone angle ( $\alpha_{max} = \gamma_c$ ). When tilting the FPI, the range of contributing angles increases. The maximum incidence angle is now  $\alpha_{max} = \gamma_c + \omega$ . In addition the whole angle range is moved towards higher values of  $\alpha$ , where  $\cos \alpha$  varies more significantly. The blurring for the tilted cone is therefore much more distinct. Only for very narrow FOVs, the FPI transmission approximately keeps its shape. For the higher finesse FPI the blurring effect is stronger, since the averaging process acts on an increasingly peaked structure.

### 3.1.2 The bandpass filter transmission spectrum

The FPI transmission spectrum covers a huge wavelength range. It is typically limited by the properties of the reflective surfaces. The wavelength range in which the FPI transmission can be matched to molecule's spectra is typically much smaller. Therefore, for instance a bandpass filter (BPF) is used to prefilter the wavelength range.

The filter's spectral transmission  $T_{BPF}$  has to be included into the instrument model. The prefiltered wavelength range substantially influences the sensitivity and the SNR. Depending on, for instance, the absorber strength or the background radiation spectrum (that can be specific to e.g. the measurement location), different

prefiltering settings can be preferred.

For the model either measurements of available filters or a variable filter model function were used:

$$T_{BPF}(\lambda; \lambda_{c,BPF}, \kappa, \iota) = a \exp \left[ \frac{|\lambda - \lambda_{c,BPF}|}{\kappa} \right]^\iota, \quad (3.3)$$

where  $a$  is the maximum transmission and  $\kappa$  and  $\iota$  are shape parameters. An example is plotted in Fig. 3.4 for  $a = 1$ ,  $\kappa = 9$  and  $\iota = 20$ .  $\lambda_{c,BPF}$  shifts the whole transmission spectrum in wavelength. In reality,  $T_{BPF}(\lambda)$  will also be a function of the incidence angle  $\alpha$ . This was neglected in this study.

### 3.1.3 Simulation of the instrument response

Via the parameters of the FPI and BPF model we can control the instruments optical transfer function. With the detector's spectral response  $Q(\lambda)$  and the spectrum of incident radiation  $I_0(\lambda)$ , the integrated radiance measured by the instrument detector can be determined:

$$I_{FPI}(d, n, \omega, \gamma_c, R, \lambda_{c,BPF}, \sigma_{BPF}) = \int_{\lambda} d\lambda I_0(\lambda) Q(\lambda) T_{FPI}^{eff}(\lambda) T_{BPF}(\lambda) \quad (3.4)$$

For  $I_0(\lambda)$  we use a measured spectrum of scattered sunlight.  $Q(\lambda)$  of a Si CCD detector is included, since the spectrum was recorded with such a detector. A certain column density  $S_i$  of a trace gas  $i$  can be added to the spectrum via the Bouguer-Lambert-Beer law and absorption cross sections  $\sigma_i$  known from laboratory measurements. The spectrum containing the absorber will be referred to as  $I(\lambda)$ .

$$I(\lambda) = I_0(\lambda) \exp(-\sigma_i S_i) \quad (3.5)$$

The same way wavelength dependent aerosol extinctions can be added. Then we can for instance simulate the optical density  $\tau_{FPI}$  seen by the FPI instrument for a certain parameter setting by:

$$\tau_{FPI} = -\log \left( \frac{I_{FPI}}{I_{0,FPI}} \right) \quad (3.6)$$

$$= -\log \left( \frac{\int_{\lambda} d\lambda I_0(\lambda) \exp(\sigma_i(\lambda) S_i) Q(\lambda) T_{FPI}^{eff}(\lambda) T_{BPF}(\lambda)}{\int_{\lambda} d\lambda I_0(\lambda) Q(\lambda) T_{FPI}^{eff}(\lambda) T_{BPF}(\lambda)} \right) \quad (3.7)$$

In this case  $\tau_{FPI}$  is a function of the trace gas absorption of the species  $i$ . We can now for instance simulate the AA of an FPI instrument with two FPI settings according to Eq. (2.32). In the scope of this work only trace gas and aerosol extinction is considered. In principle, more comprehensive radiative transport effects could be included, using simulated spectra from radiative transfer models, where the absorbers and scatterers are varied within.

### 3.1.4 Signal to noise ratio

The instrument response of a realistic instrument will always contain noise. We need a measure for the signal to noise ratio (SNR) in our model in order to account for the light throughput of an instrument or the amount of light coming from the measurement wavelength range.

The instrument responses are obtained from radiance measurements that obey photon statistics. Via Gaussian error propagation, the noise of the instrument response can be calculated from the radiance noise. It was assumed that the integrated radiances  $I$ , are proportional to the number of photons reaching the detector. The corresponding photon shot noise  $\Delta I_{shot}$  is then:

$$\Delta I_{shot} = \sqrt{I}. \quad (3.8)$$

For an arbitrary instrument response  $r$ , determined from  $i$  integrated radiance measurements  $I_i$  the SNR is given by:

$$SNR = \frac{r}{\Delta r} = r \left[ \sum_i \left( \frac{\partial r}{\partial I_i} \Delta I_{shot,i} \right)^2 \right]^{-\frac{1}{2}} \quad (3.9)$$

From the measured reference spectrum  $I_0(\lambda)$ , the absolute number of photons is not known. Therefore, it is also not possible to calculate absolute SNRs. If there are extrema in the SNR, they will not depend on the absolute, but rather on the relative radiance distribution in the spectrum  $I_0(\lambda)$ . Certainly, the assumptions made are fairly rough, e.g.  $Q(\lambda)$  is not accounted for. The SNR estimates are however sufficient for qualitative considerations and coarse optimization calculations.

## 3.2 Model results for FPI based SO<sub>2</sub> measurements in the UV

### 3.2.1 Properties and optimum parameters of a UV FPI SO<sub>2</sub> measurement

As explained in section 2.3.2 the FPI transmission structure is matched to the narrowband SO<sub>2</sub> absorption structures at around 310 nm. Figure 3.4 shows the SO<sub>2</sub> absorption cross section  $\sigma_{SO_2}(\lambda)$  from Vandaele et al. (2009) as a function of wavelength (black line, upper panel). In order to roughly match an FPI transmittance spectrum to the distinct band structure we demand the FSR (Eq. (2.26)) to be equal to the spectral distance  $\delta\lambda_{SO_2}$  between two SO<sub>2</sub> absorption bands:

$$\delta\lambda = \frac{\lambda_m^2}{2nd \cos \alpha} \stackrel{!}{=} \delta\lambda_{SO_2} \quad (3.10)$$

At the wavelength  $\lambda_m = 310\text{nm}$ , for  $\alpha = 0$  and  $n = n_{air}$  the surface separation  $d$  of the FPI would be  $22\mu\text{m}$ . The transmittance spectrum of an FPI with  $d = 21.68\mu\text{m}$

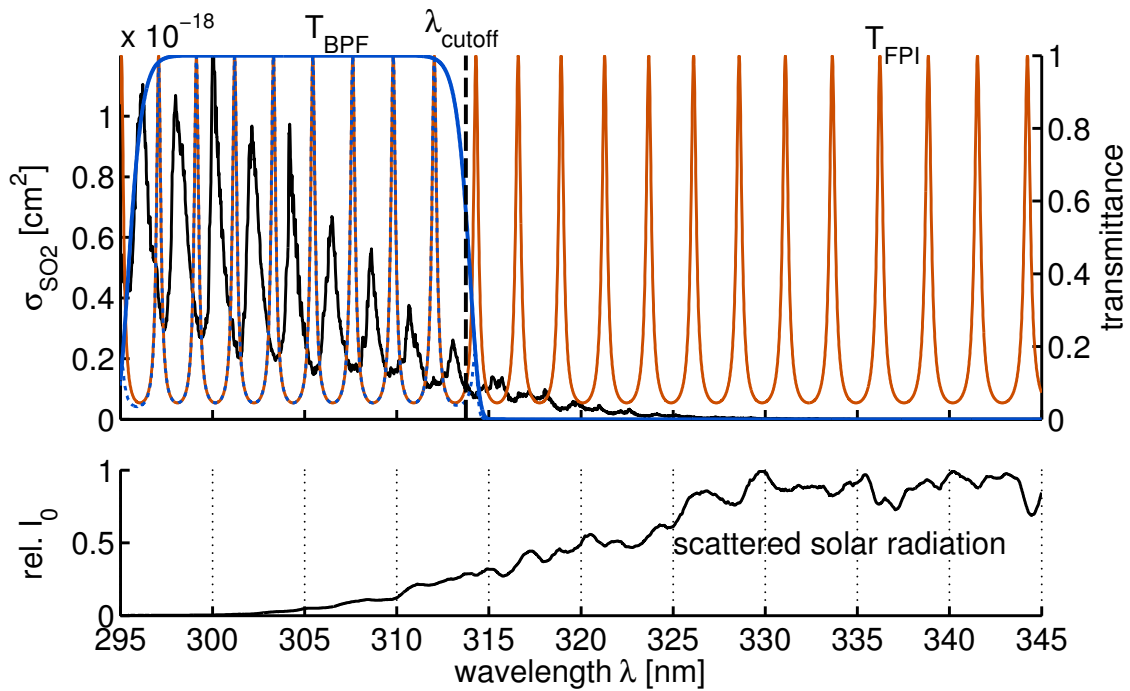


**Figure 3.4** –  $\text{SO}_2$  absorption cross section (black drawn) and a  $T_{\text{FPI}}$  with the FSR matched to the separation of the absorption bands (orange drawn) are shown in the upper panel. The measurement range is limited by the BPF (blue drawn) to wavelengths of matching absorption. The setup's effective transmission ( $T_{\text{BPF}} \times T_{\text{FPI}}$ ) is indicated by the dashed blue line. In the lower panel a typical spectrum of incoming scattered solar radiation is plotted.

and  $R = 0.65$  is plotted in orange. This FPI transmits radiation in between the strong SO<sub>2</sub> absorption bands and quasi 'looks through' the gas.

In the lower panel of Fig. 3.4 the incoming scattered solar radiation is plotted in arbitrary units. Compared to longer wavelengths, there is only little light at wavelengths of distinct SO<sub>2</sub> absorption structure ( $\lambda < 315$  nm). Light transmitting the FPI at longer wavelengths will therefore clearly dominate every integrated radiance measurement, and the SO<sub>2</sub> optical density will vanish. Thus the measurement wavelength range needs to be limited to wavelengths where the absorption structure is strong and matches the FPI transmittance. This is done by a BPF (blue drawn line). The dotted blue line is the spectral transmittance of the whole optical setup. In the following the properties of such a setup are examined using the described model. For the case of SO<sub>2</sub>, the filter model is simplified. The solar radiance for wavelengths  $\lambda < 300$ nm on Earth's surface is almost negligible. The differential band structure of SO<sub>2</sub> at these wavelengths is strong and weakens towards longer wavelengths. We therefore expect the optimal absorption signal to be dominated by the BPFs longer wavelength cutoff edge  $\lambda_{cutoff}$  ( $T_{bpf}(\lambda_{cutoff}) = \frac{T_{bpf}}{2}$ , see Fig. 3.4).

### Instrument parameters

Figure 3.5 shows the optical density  $\tau_{FPI}$  seen through the FPI setup for an SO<sub>2</sub> column density of  $S_{SO_2} = 10^{18}$  molec cm<sup>-2</sup> for a varying FPI surface separation  $d$ . Moreover, the integrated radiances with ( $I_{FPI}(d)$ ) and without ( $I_{0,FPI}(d)$ ) SO<sub>2</sub> absorption are plotted. The variation of  $d$  represents a variation in the optical path difference  $\Delta(d, n, \cos \alpha)$ . In the same way,  $n$  or  $\cos \alpha$  could have been chosen as varying parameter in the following considerations. Different line styles represent different FPI surface reflectivities  $R$ .

The order  $m$  of the transmission peaks in the regarded wavelength range is reasonably high ( $m = \frac{2nd}{\lambda_m} \approx 140$ ). Therefore, we expect an almost pure shift of the FPI transmittance spectrum with changing  $d$ . The progression of  $I_{FPI}(d)$  in the regarded small range of  $d$  is approximately a convolution of the FPI transmittance spectrum with the spectrum of incoming radiance.

We already observe wavelike modulations of the integrated radiance  $I_{0,FPI}$  without added SO<sub>2</sub> absorption (upper left panel of Fig. 3.5). This could be due to spectral features of  $I_0(\lambda)$ . The fact that the FPI transmittance peak is continuously shifted across the BPFs cutoff edges can be another explanation, since at the longer wavelength edge the incoming radiance is significantly higher.

When adding the SO<sub>2</sub> absorption the wavelike modulations change. Moreover, the broadband SO<sub>2</sub> absorption contribution weakens the average signal. For the optical density  $\tau_{FPI}$  (Eq. 3.7), the modulation is only caused by the SO<sub>2</sub> absorption. For several orders, the modulation amplitude is approximately constant as expected from the high order of the transmittance maxima.

For increasing reflectivity  $R$ , and therefore increasing finesse, the modulation amplitude of  $\tau_{FPI}$  increases. This is explained by the fact that for higher finesses and the

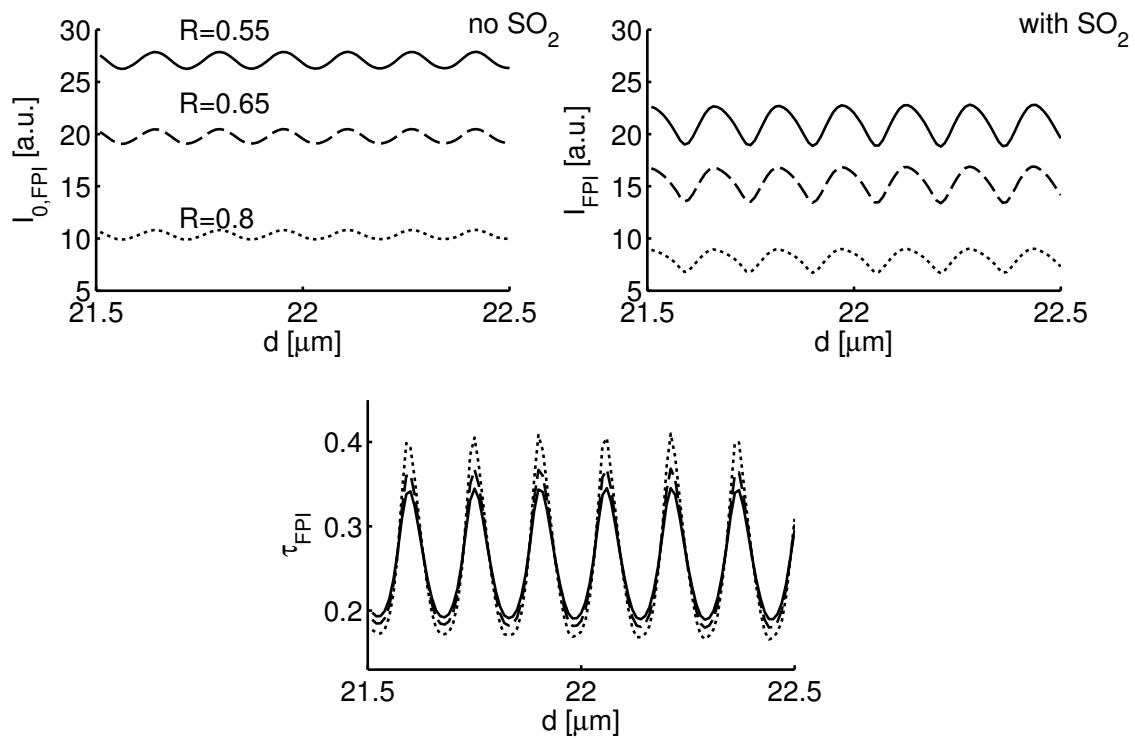


**Figure 3.5** – In the upper panel the integrated radiances, seen by the FPI setup, are plotted; on the left side without added SO<sub>2</sub> absorption, on the right side with an added SO<sub>2</sub> column density of  $10^{18}$  molec cm<sup>-2</sup>. The lower panel shows the optical density  $\tau_{FPI}$  calculated from the above radiances. The modulation approximately represents a convolution of the FPI transmittance spectrum with the SO<sub>2</sub> absorption spectrum.

same FSR the FPI transmittance peaks get sharper. The above mentioned convolution is carried out with an increasingly sharp peak structure and therefore samples the  $\text{SO}_2$  absorption peaks more accurately. Hence, the modulation amplitude is a measure for the sensitivity of the FPI measurement.

The progression of  $\tau_{FPI}(d)$  in the lower panel of Fig. 3.5 suggests values  $d_A$  and  $d_B$  for the FPI settings A and B (see Sect. 2.3.2). Setting A corresponds to a FPI transmittance structure that correlates with the  $\text{SO}_2$  absorption peaks. The corresponding value for  $d_A$  maximizes  $\tau_{FPI}(d)$ . In contrast,  $d_B$  minimizes  $\tau_{FPI}(d)$ , because in setting B the FPI transmits best possible in between the absorption peaks. The AA of the FPI  $\text{SO}_2$  measurement is determined by the optical densities of the two settings according to Eq. 2.32.

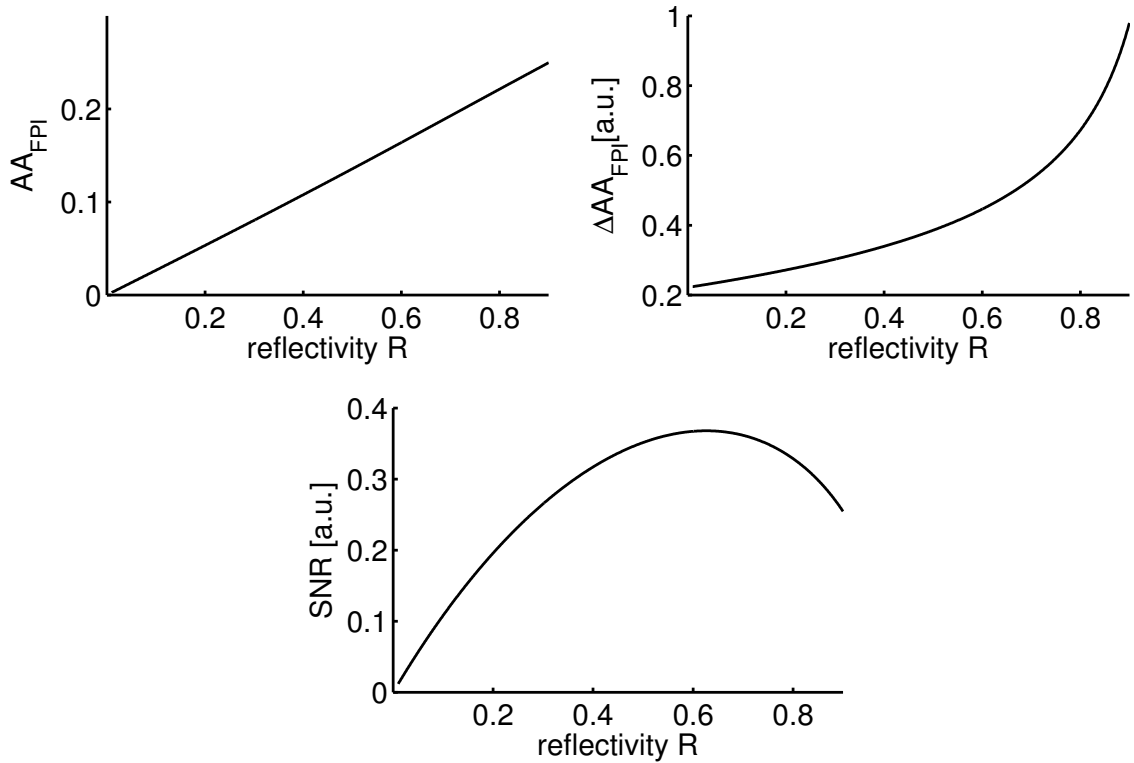


**Figure 3.6** – The Upper left panel shows the AA of an FPI device for  $S_{\text{SO}_2} = 10^{18} \text{ molec cm}^{-2}$  and varying FPI surface reflectivity  $R$ . On the right the corresponding progression of the noise  $\Delta AA$  is plotted. It increases with  $R$  due to the gradually reduced light throughput. The lower subplot shows the progression of the SNR that peaks at around  $R = 0.6$ .

In Fig. 3.6 the impact of the reflectivity  $R$  on the sensitivity is further assessed. The upper left panel shows the AA for constant  $S_{\text{SO}_2} = 10^{18} \text{ molec cm}^{-2}$  as a function of  $R$ . It monotonically increases with  $R$  due to the increasing sharpness of the transmission structure. On the other hand, the noise  $\Delta AA$  (from photon noise, upper right panel) increases drastically for higher  $R$  since the FPI's light throughput is reduced. Hence, the  $\text{SNR}(R)$  (lower panel) has a maximum value. Note that the

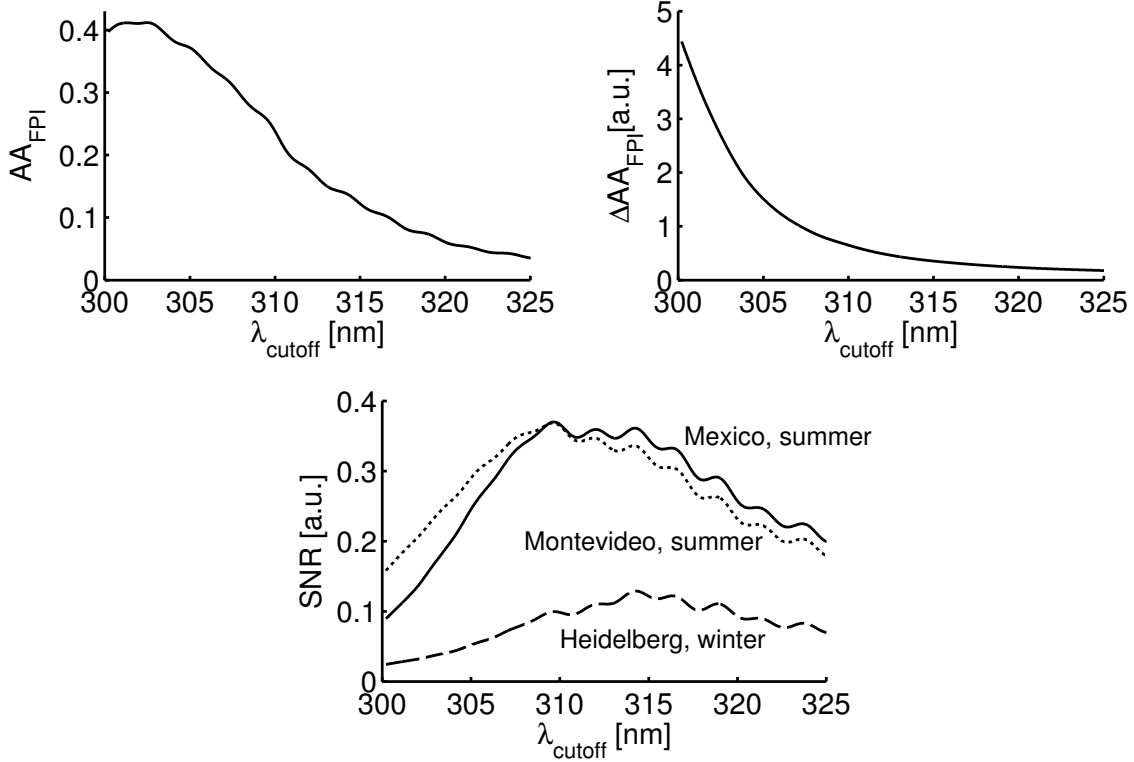


**Figure 3.7** – The upper panels show for  $S_{SO_2} = 10^{18} \text{ molec cm}^{-2}$  and a varying BPF cutoff edge  $\lambda_{cutoff}$  the AA of the FPI setup and the progression of the corresponding noise  $\Delta AA$ . A reference spectrum recorded in Mexico in summer was used for this simulations. Due to different incoming radiance spectra, the optimum of the SNR (lower panel) is dependent on location and time.

reflectivity  $R_{max}$ , maximizing the SNR is not dependent on the absolute number of incoming photons. It only depends on their spectral distribution that is approximated by the measured radiance spectrum  $I_0(\lambda)$ .

The distinct periodical  $SO_2$  absorption features appear in a wavelength range, where the incoming scattered radiance drops significantly (Fig. 3.4). This is mainly due to the strong UV absorption of stratospheric ozone. The choice of the optimal BPF is therefore again a tradeoff between light throughput of the setup (determining the noise) and sensitivity. Figure 3.7 shows the AA (upper left panel), the noise  $\Delta AA$  of the AA (upper right panel) and the SNR (lower panel) as a function of the longer wavelength cutoff edge of the filter  $\lambda_{cutoff}$ . The AA peaks at a very low value of  $\lambda_{cutoff}$ , where the noise is extensively high due to vanishing scattered radiance. The AA drops for higher  $\lambda_{cutoff}$  in a slightly wavy progression. The drop is explained by the inclusion of weaker  $SO_2$  absorption bands to the measurement. The waves originate from the individual absorption bands that gradually enter the measurement wavelength range. For an increasing  $\lambda_{cutoff}$ ,  $\Delta AA$  decreases steadily since wavelength with increasing radiance are covered.

**Table 3.1** – Result of the numerical optimization of the SNR for an FPI SO<sub>2</sub> measurement for  $S_{SO_2} = 10^{18}$  molec cm<sup>-2</sup>.  $d_{AB} = d_A - d_B$  is the required tuning of  $d$  to conduct the change between setting A and setting B. Analogously, a  $\alpha_{AB}$  of  $n_{AB}$  can be found. Adapted from Kuhn et al. (2014)

Parameter	Maximizing value
$d_A$	21.6 $\mu m$
$d_{AB}$	84nm
$R$	0.65 ( $F = 7.1$ )
$\lambda_{cutoff}$	310nm

Due to the square root dependency of the photon shot noise,  $\Delta AA$  firstly shows a strong drop but then slowly flattens. The decrease in AA for higher  $\lambda_{cutoff}$  is stronger, determining a maximum SNR.

## Optimization

The SNR for the SO<sub>2</sub> measurement was optimized regarding all instrument parameters in Kuhn et al. (2014). The corresponding instrument’s transmission spectra are plotted in Fig. 3.8. The calculation was done numerically for an SO<sub>2</sub> column density of  $S_{SO_2} = 10^{18}$  molec cm<sup>-2</sup>. Table 3.1 shows the results. From the simulations and considerations above we can conclude that the optimized values of both, the reflectivity and the BPF cutoff wavelength, have a certain range where the SNR does not change significantly. It is important to bear in mind, that the simulation is based on a measured spectrum, representing the radiance spectrum at a certain time and location. The impact on the SNR can be seen in Fig. 3.7, where the SNR is plotted in different line styles for different locations. Moreover the optimal  $\lambda_{cutoff}$  can be dependent on the amount of SO<sub>2</sub> that is present. High SO<sub>2</sub> column densities, cause high extinctions in the measurement wavelength range and therefore increase the noise. Volcanoes differ substantially in their SO<sub>2</sub> emission rate. The optimizing BPF constellation can therefore also be volcano specific.

### 3.2.2 Comparison to the SO<sub>2</sub> Camera

The above described model allows the comparison between FPI SO<sub>2</sub> measurement and the filter based SO<sub>2</sub> Camera method in terms of sensitivity and selectivity. The SO<sub>2</sub> camera’s instrument response can be simulated using the transmittance profiles of filter A and filter B. Figure 3.8 and 3.9 depicts the combined spectral data used for the instrument models. The SO<sub>2</sub> Camera instrument response was simulated for two choices of filter A (denoted by A and A’), in order to cover different existing camera schemes. The instrument responses (AA) are simulated as a function of the SO<sub>2</sub> column density  $S_{SO_2}$ . Then, the extinction of gases or aerosol is added in order to look at their cross interference. The results are published in Kuhn et al. (2014)

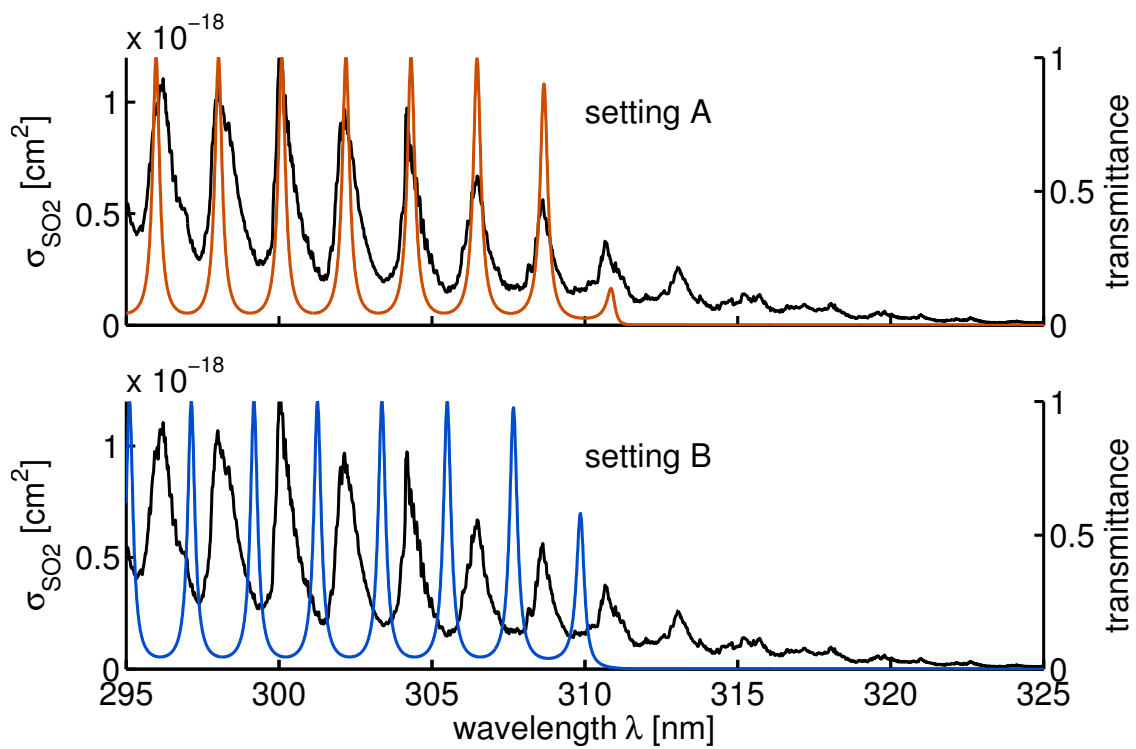


**Figure 3.8** – Spectra of the optimized FPI settings A (upper panel) and B (lower panel) with the  $\text{SO}_2$  absorption cross section.

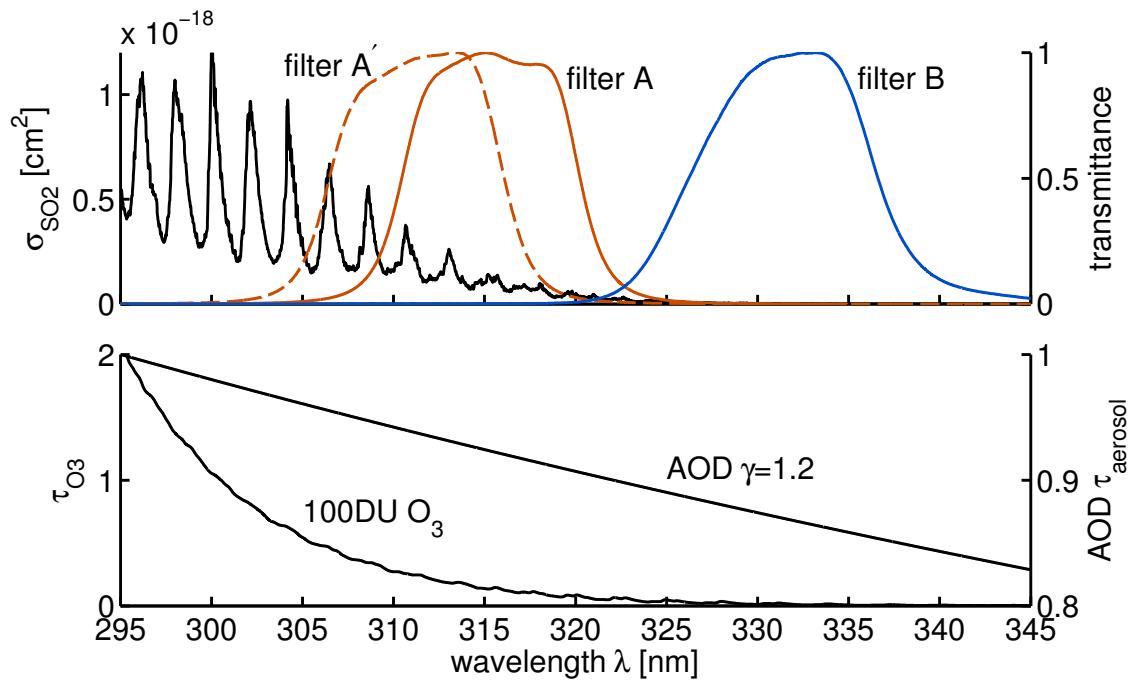


**Figure 3.9** – Spectra used for the comparison of SO<sub>2</sub> Camera with the FPI method. An additional filter A (A', dashed line, upper panel) was used to cover several existing SO<sub>2</sub> camera setups. In the lower panel the optical densities of the examined interfering effects are plotted: 100DU ozone (left ordinate axis) and a plume AOD of  $\approx 1$  with an Ångström exponent of  $\gamma = 1.2$  (right ordinate axis).

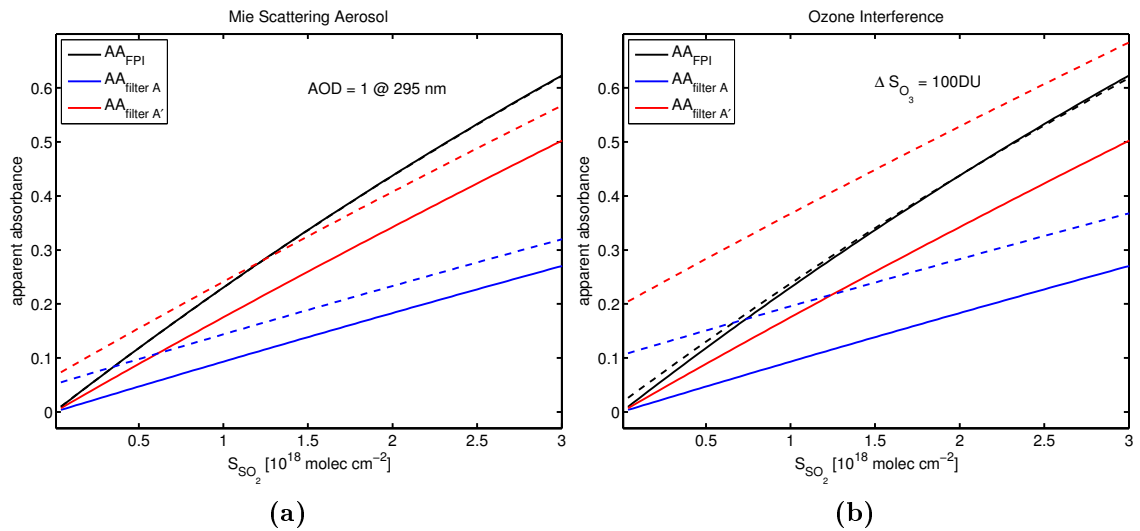


**Figure 3.10** – Simulated calibration curves for the two SO<sub>2</sub> camera schemes and the FPI method. In (a) the dashed lines show the reaction of the instrument response to a plume AOD of  $\approx 1$  with an Ångström exponent of  $\gamma = 1.2$ . (b) shows the reaction to an ozone variation of  $\Delta S_{\text{O}_3} = 100\text{DU}$ . In addition to the higher sensitivity, in both cases the FPI method shows drastically reduced cross interferences. Adapted from Kuhn et al. (2014)

and shown in Fig. 3.10. The cross interference to an aerosol optical density (AOD)  $\tau_{aerosol}$  of 1 at 295nm with an Ångstrom exponent  $\gamma = 1.2$  (sub frame (a)), and to an ozone variation of 100DU (sub frame (b)) was examined ( $\sigma_{O_3}$  from Serdyuchenko et al., 2014). The dashed lines display the instrument response after adding the interfering extinction to  $I_0(\lambda)$ .

The sensitivity of the FPI approach is higher than both SO<sub>2</sub> Camera configurations. The differential SO<sub>2</sub> absorption sensed by the FPI is stronger than the average SO<sub>2</sub> absorption in the wavelength ranges of filter A and filter A'. For high  $S_{SO_2}$  the FPI's calibration curve flattens due to saturation at wavelengths of strong absorption bands.

Apart from the sensitivity advantage, the cross interferences to the FPI's AA is by far smaller than for the SO<sub>2</sub> Camera. For volcanic plumes the assumed AOD is still moderate. However, due to its extinction, it causes false SO<sub>2</sub> signals of around  $3 - 5 \cdot 10^{17}$  molec cm<sup>-2</sup> for the SO<sub>2</sub> Camera. The high aerosol cross interferences were already identified in measurements by e.g. Lübcke et al. (2013). The effect on the FPI method is hardly visible in the graph, since dashed and drawn line nearly completely overlay. The behavior is very similar for the ozone interference.

The assumed variation in ozone of 100DU can be reached by the changing SZA within hours. However, the SO<sub>2</sub> Camera's high spacial and temporal information content can be utilized to correct for this gradual ozone background change (see Sect. 2.2.2). Variations across the image can still occur and cause false SO<sub>2</sub> signals, however on a scale, that is commonly not significant for the measurement.

Aerosol can have multiple impacts on remote sensing measurements. In this study, only effects of an extinction due to Mie scattering were investigated. The DOAS calibration method can to some extent account for this effect. For often observed inhomogeneous aerosol distributions in volcanic plumes this method is however also quite error prone.

This simple simulation showed, that the FPI SO<sub>2</sub> remote sensing technique can on the one hand reach a higher sensitivity. On the other hand its higher selectivity can replace or stabilize the correction procedures of the SO<sub>2</sub> Camera technique.

### 3.2.3 FPI imaging issues

An imaging FPI device can be implemented in different ways that will further be treated in Chap. 5. Here, the example of an FPI placed in front of a lens and a detector array (sketched in Fig. 3.11) is utilized to describe the basics of modeling imaging FPI setups.

Each viewing direction within the camera FOV is projected onto a different location on a detector array to a pixel  $\{i, j\}$ . The incidence angle  $\alpha$  for each viewing direction determines the FPI transmission spectrum for the respective pixel. In Fig. 3.12 (a), the optical density  $\tau_{FPI}$  for  $S_{SO_2} = 10^{18}$  molec cm<sup>-2</sup> is plotted as a function of  $\alpha$ . In addition, the progression of the integrated background intensity  $I_{0,FPI}$  seen through the setup is shown (dashed line).

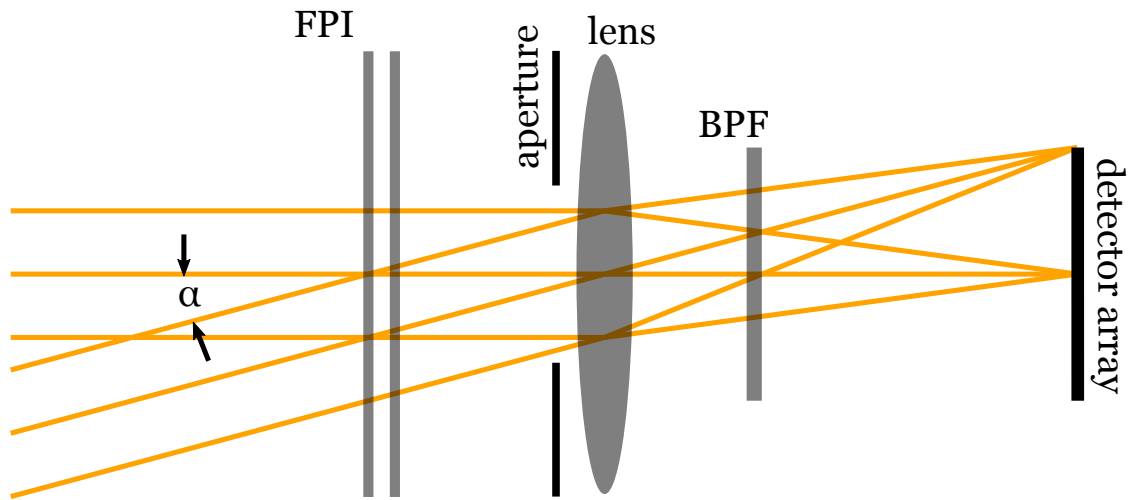


**Figure 3.11** – Sketch of an optical setup, where different incidence angles  $\alpha$  cause rings of equal FPI transmittance spectra on the detector.

The modulations of  $I_{0,FPI}$  and  $\tau_{FPI}$  are expected from above considerations. However, due to the cosine in  $\Delta(\alpha)$ , the frequency of this modulation increases with  $\alpha$ . Figure 3.12 (b) and (c) depict the distributions  $I_{0,FPI}$  and  $\tau_{FPI}$  on the detector array of a setup as sketched in Fig. 3.11. The ring shaped features are expected from the above discussed incidence angle dependency and the fact that  $\alpha$  increases nearly linearly from the detector center. The center of the image edge corresponds to  $\alpha = 10^\circ$ .

For small incidence angles there is a range of about  $2^\circ$ , where the sensitivity of the FPI measurement doesn't change substantially. This is essential for many applications.

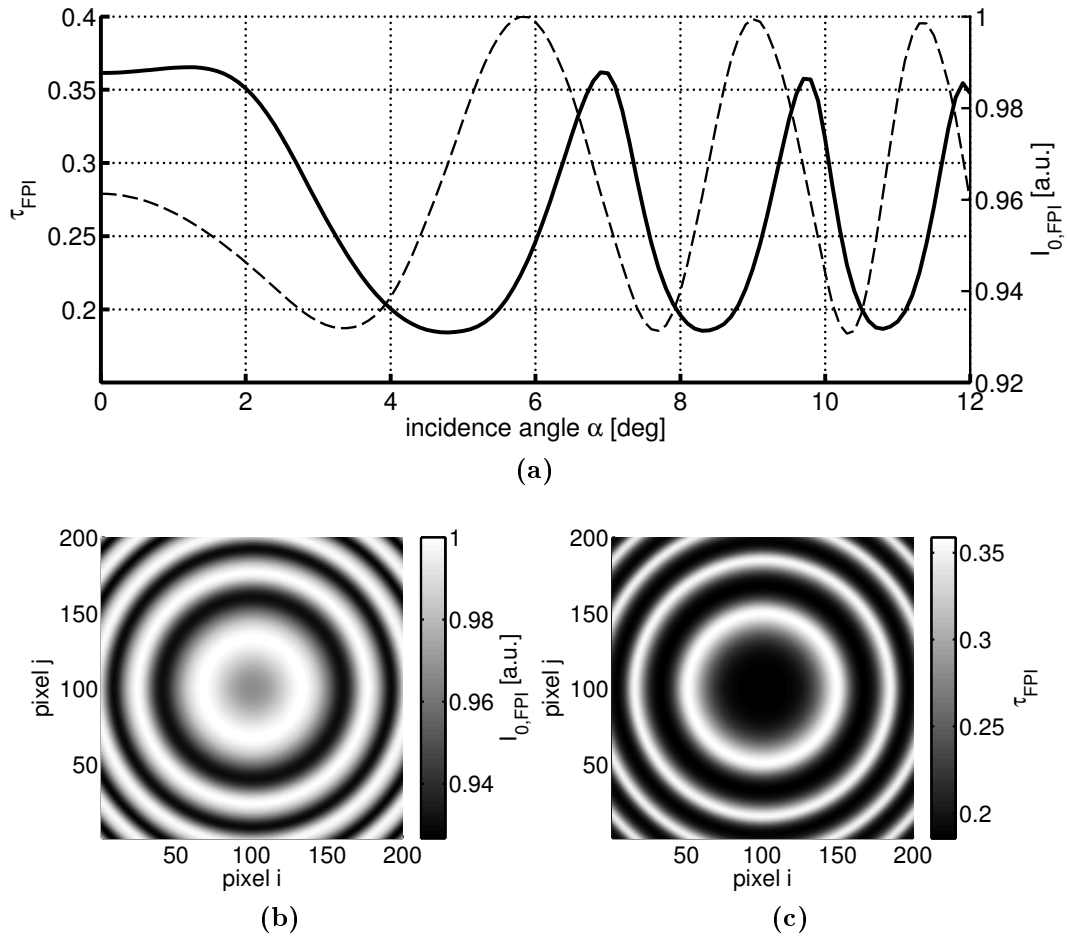


**Figure 3.12** – (a) integrated intensity  $I_{0,FPI}$  and optical density  $\tau_{FPI}$  of  $S_{SO_2} = 10^{18} \text{ molec cm}^{-2}$  seen through FPI setup as a function of the incidence angle  $\alpha$ ; (b) and (c) maps of  $I_{0,FPI}$  and  $\tau_{FPI}$  on a detector array. For instance recorded with the setup in Fig 3.11

## 4 Proof of concept study - The one pixel FPI SO<sub>2</sub> device

In this chapter, the above described method of remote sensing SO<sub>2</sub> with an FPI is verified experimentally. A one pixel (OP) FPI device was built in order to verify the measurement principle apart from its application to imaging. This is important to gain general experience in the work with the experimental setup, before realizing more complex imaging applications. Moreover, a OP FPI SO<sub>2</sub> device can already be applied in volcanic field practice. It can be built simple, small and robust. As shown in the model study, the instrument response represents reliable SO<sub>2</sub> information, without intricate data evaluation.

In section 4.1 the experimental instrument setup of the OP FPI SO<sub>2</sub> device is described. Its performance is evaluated in Sect. 4.2

### 4.1 OP FPI SO<sub>2</sub> device - instrument setup

In this section the experimental instrument setup of the OP FPI SO<sub>2</sub> device is introduced. The employed, commercial FPI is described, before introducing the optical setup and the detector unit.

#### 4.1.1 The realistic Fabry-Perot interferometer

There are two FPI implementation types, the air spaced FPI and the solid FPI. The two fused silica plates of the air spaced FPI can be separated by a material with very low thermal expansion coefficient. The refractive index of air is also hardly dependent on typical ambient temperature variations. In contrast, when using a single fused silica plate in a solid FPI, the temperature dependence of refractive index and the thermal expansion are far higher. This can be regarded as disturbing, but also as an additional tuning option. We preferred the stability of the air spaced type to the apparently unhandy and inert temperature tuning option.

Fabricating FPIs with specifications as displayed in Tab. 3.1 is challenging. The light throughput advantage of nondispersive methods requires a high clear aperture of the WSE. Across the clear aperture of the FPI, the two silica plates need to be parallel on a nanometer scale, since already a surface displace of  $d_{AB} = 84nm$  is responsible for the change from FPI setting A to B. Moreover, the plate surfaces need to be flat on that scale. The flatness and the parallelism can be expressed in a finesse value. In order to determine the effective FPI finesse via the reflectivity  $R$  (Eq. (2.23)), the flatness finesse and the parallelism finesse need to be distinctly



**Figure 4.1** – Fabry-Pérot interferometer from *SLS Optics Ltd.*; two fused silica plates are mounted in the steel cell. Across a 2cm clear aperture the parallelism and flatness of the coated inner plate surfaces (reflectivity  $R = 0.65$ ) is of the order of nanometers.

higher than the reflectivity finesse (see Eq. (2.29)).

In the scope of the required parallelism, tuning via varying the surface displacement (as proposed in [Kuhn et al., 2014](#)) seemed to be hardly realizable. Therefore, a fixed separation air spaced FPI etalon, was purchased from *SLS Optics Ltd.*

### FPI properties

The air spaced FPI is shown in Fig. 4.1. The two  $\sim 10$  mm thick fused silica plates are mounted inside a steel cell. The outer surfaces have opposed wedge angles of  $0.5^\circ$  and have anti reflective coatings in order to avoid interference effects from these surfaces. The spacer material is *Corning ULE* glass (ULE: Ultra Low Expansion). The inner surfaces of the plates have reflective coatings of  $R = 0.65$  at 305 nm, dominating the finesse across a clear aperture of 20 mm.

The surface separation  $d$  could only be specified roughly by the manufacturer. The approximate values were based on coating thickness estimates and had to be validated by our measurements.

Figure 4.2 shows the radiance spectrum of light from a Xe-lamp guided through the FPI after parallelization (orange line). The spectrum was recorded with a grating spectrometer from *Avantes* and a  $100\ \mu\text{m}$  entrance slit. With this spectrometer the finesse can not be examined, since the limited spectral resolution ( $\Delta\lambda \approx 0.6\text{nm}$ ) blurs the peaks. Assuming a symmetric instrument function, the spectral location of the transmission peaks can be determined. A modeled FPI transmission spectrum was matched to this measurement. From the measurement setup it is known that  $n = n_{air}$  and that  $\alpha \approx 0$ . The dashed line shows the modeled FPI transmission spectrum that corresponds to  $d = 21.38\ \mu\text{m}$ . With the high amount of observed transmission peaks the deviations of the FPI transmission spectra of the neighbouring orders could be identified well. The surface displacement  $d$  can thus be determined accurately. Limitations are the calibration of the spectrometer and the certainty of the range of incidence angles of light traversing the FPI.

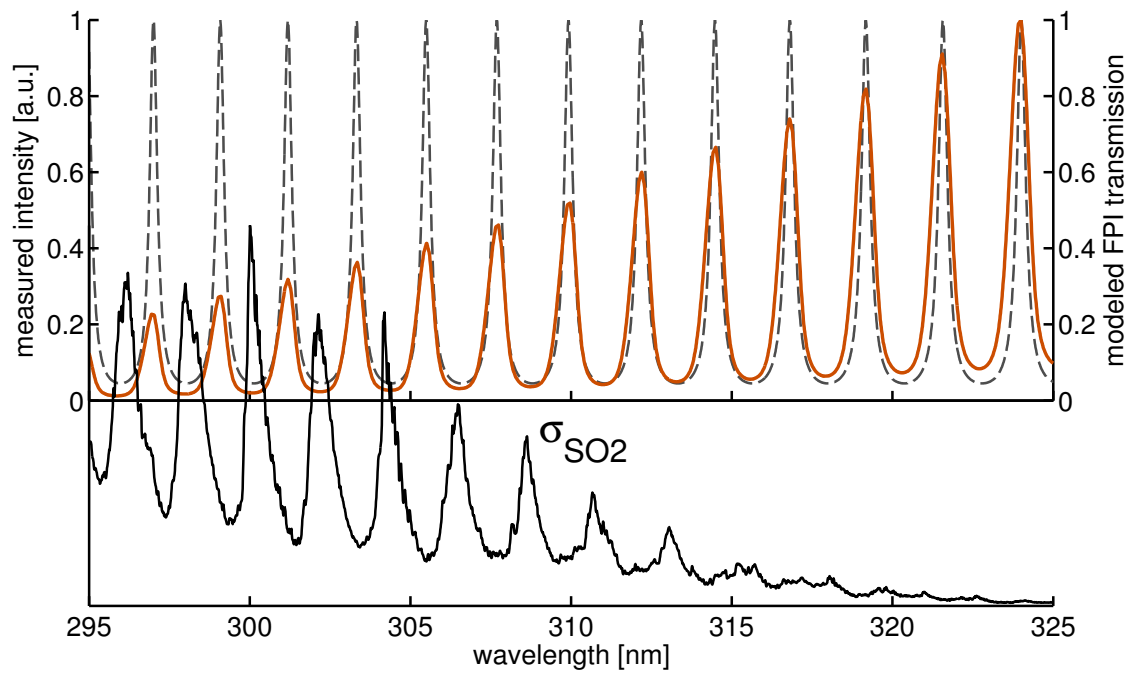


**Figure 4.2** – In orange, the light of a Xe-lamp that traversed the FPI is plotted. The dashed line shows the matched modeled FPI transmission spectrum that was used to determine the surface separation  $d$  of the FPI.  $\sigma_{SO_2}$  is additionally plotted to illustrate the matching of FPI FSR and spectral  $SO_2$  absorption band displacement.

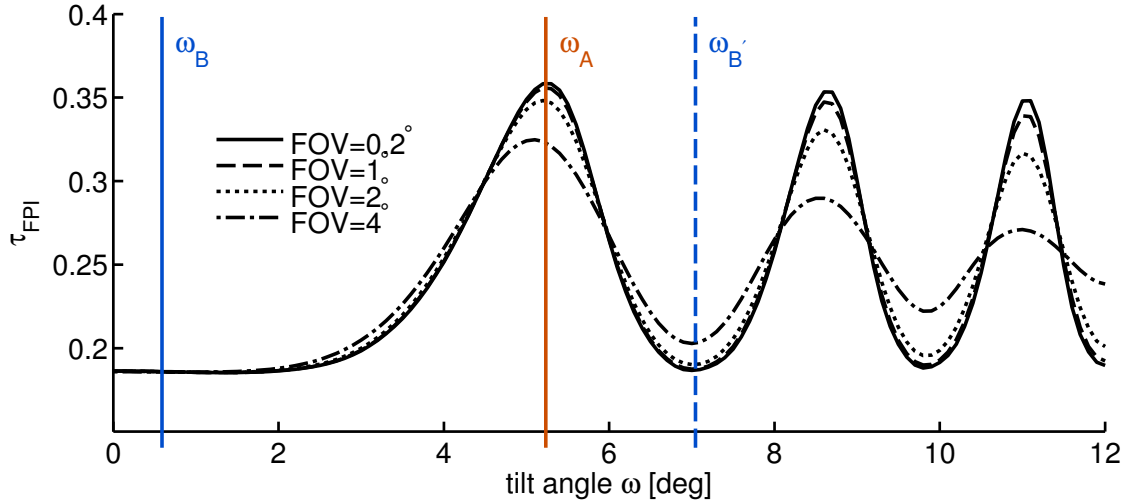


**Figure 4.3** – The optical density seen through the FPI setup  $\tau_{FPI}$  is plotted as a function of the FPI tilt angle. The FPI is tilted within a light cone of different FOV angles (line styles). The etendue of an FPI instrument can be increased by illuminating the FPI with a wider light cone. The sensitivity of the measurement decreases thereby due to the blurring of the spectral FPI transmission. See also Fig. 3.3

The FSR of the FPI nicely matches to the spectral separation of the  $SO_2$  absorption bands (also plotted in Fig. 4.2).

### Tuning the FPI

A very simple measurement scheme would employ two FPIs with different spectral transmittances. They could be employed similarly to the filters of  $SO_2$  Camera's. In this thesis, this possibility is not discussed since only one FPI was available for the experiments.

Another measurement scheme is thinkable where a FPI channels is compared with a channel without FPI (as e.g in [Wilson et al., 2007](#)). Compared to the tuning methods discussed in this thesis, the sensitivity of such a setup is significantly lower.

Since the surface separation of the here applied FPI is fixed the only tuning parameters remaining are the refractive index  $n$  and the incidence angle  $\alpha$ . The required change  $n_{AB}$  in the refractive index to tune the FPI from setting A to setting B is  $\sim 0.003$ . This could for instance be implemented by filling a gas of high refractive index (e.g. Freon 12 with  $n_{F12} = 1.001$  at 435.8 nm [Horvath, 1967](#)) in between the surface and varying the pressure on the scale of a few atmospheres.

Tuning via the incidence angle  $\alpha$  is the technically most convenient tuning option for OP devices and can be implemented by tilting the FPI inside the light path. The incidence angle range has to be limited in order to prevent extensive blurring of the FPI transmission spectrum for higher tilt angles  $\omega$ . Fig 4.3 shows the modeled  $\tau_{FPI}$  for  $S_{SO_2} = 10^{18} \text{ molec cm}^{-2}$  as a function of the FPI tilt angle  $\omega$ . The line styles

represent different FOV cone angles of the light beam incident on the FPI. Greater FOVs are more affected by blurring, thus leading to lower sensitivity. From the progression of  $\tau_{FPI}$  we can define  $\omega_A$  and  $\omega_B$  for the measurement. In our experimental setup the FPI is tilted by a servo motor (see e.g. Fig. 4.4 (b)).

### 4.1.2 The optical setup

The first prototype of the OP FPI SO<sub>2</sub> device has a very simplistic optical setup, shown in Fig. 4.4. A single lens projects light from a narrow FOV onto a single pixel in its focal plane. The tiltable FPI is located in front of the lens, the BPF is placed in front of the FPI, practically serving as outer window of the instrument. Lens tubes, apertures and a box around the optical setup block straylight. The focal length  $f$  of the lense and the cross section  $s_p$  of the OP detector determine the cone angle  $\gamma_c$  of the light beam traversing the FPI and thereby the FOV opening angle ( $2\gamma_c$ ) of the instrument:

$$\gamma_c = \arctan \frac{s_p}{2f} \quad (4.1)$$

### Etendue

The etendue  $E$  is a measure for the light throughput of an instrument regarding its geometrical optical setup. A higher etendue in a radiance measurement therefore means a higher SNR. It is determined by the product of maximum beam cross section  $A_{\text{beam}}$  and maximum beam solid angle  $\Omega_{\text{beam}}$  of the beam that reaches the instrument's detector:

$$E = A_{\text{beam}} \cdot \Omega_{\text{beam}} \quad (4.2)$$

In the described setup, the maximum beam cross section  $A_{\text{beam}}$  is limited by the clear aperture of the FPI (lens and BPF clear apertures are larger). The maximum solid angle  $\Omega_{\text{beam}}$  for this setup is limited by the FPI's incidence angle dependency. For large FOV the blurring of the spectral FPI transmission increases, especially when the FPI is tilted (see Fig. 4.3). This results in a lower sensitivity. In our simple setup, the instrument's FOV is equivalent to the light cone incident on the FPI. Via a parallelization optics and large aperture lenses, (as proposed in [Kuhn et al., 2014](#), see Fig. 5.1) the etendue of a OP device can be further increased.

### Bandpass filter

We used an interference BPF with a transmittance range, comparable to the SO<sub>2</sub> Camera filter A' in Fig. 3.9. In order to shift the transmittance wavelength range towards lower wavelengths, it is placed inside a lens tube with a tilt angle of  $\omega_{\text{BPF}} \approx 10^\circ$ . This shift can be approximated by the expression

$$\lambda_{c,\text{BPF}}(\omega_{\text{BPF}}) \approx \lambda_{c,\text{BPF}}(0^\circ) \sqrt{1 - \frac{\sin^2(\omega_{\text{BPF}})}{n^2}}. \quad (4.3)$$

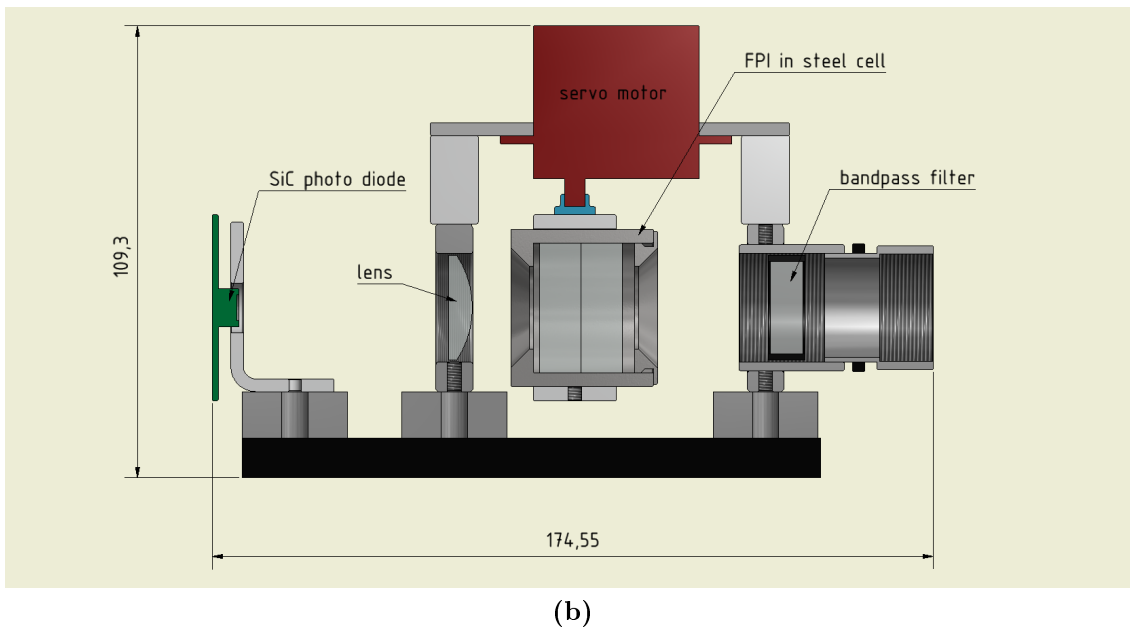
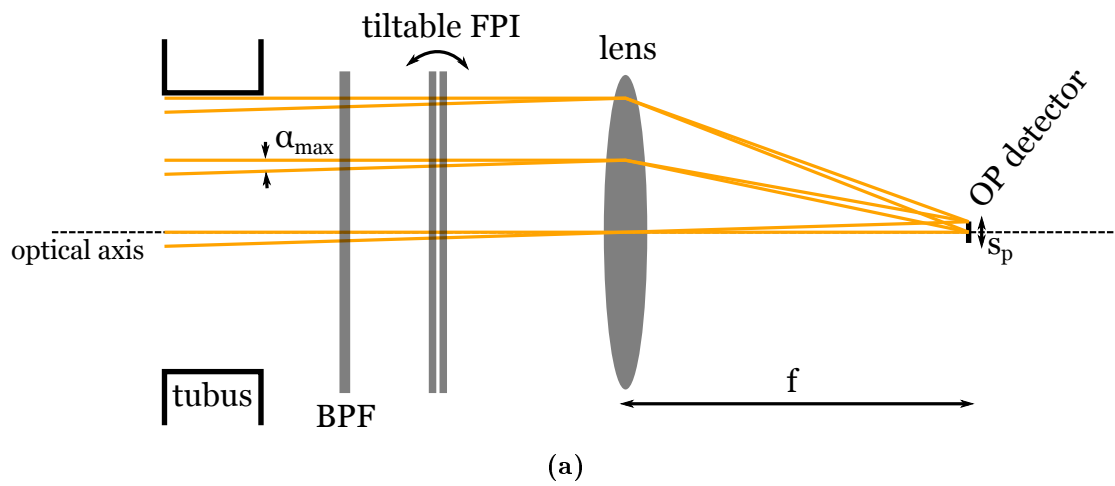


**Figure 4.4** – (a) schematic drawing of the optical setup of the OP FPI instrument. A single lens is used to project light of the instrument FOV onto a OP detector. (b) technical drawing of the optical setup. The FPI is mounted tiltable on a servo motor. The BPF is placed inside a lens tube in front of the FPI.

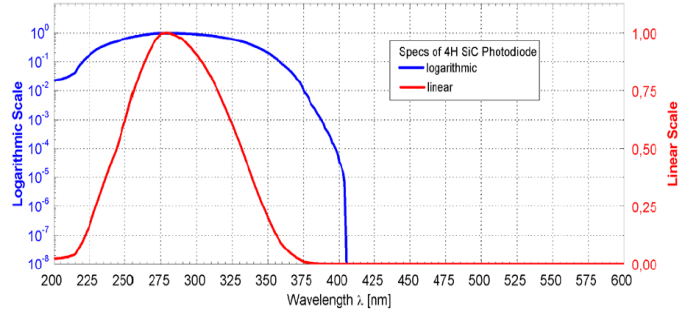


**Figure 4.5** – relative spectral responsivity of the SiC photodiode (sflux GmbH, 2015); the absolute spectral responsivity at the peak is  $0.13 \text{ A W}^{-1}$

In our case the transmittance range has approximately a center wavelength of 308 nm with a FWHM of  $\sim 5 \text{ nm}$ .

### 4.1.3 The one pixel detector

The light that traversed the optical setup is quantified by a detector, placed in the focal plane of the lens (see Fig. 4.4). The core part of the detector is the silicon carbide (SiC) photodiode. Its response (photo current  $I_{\text{ph}}$ ) from the scattered sunlight in the measurement wavelength range is very low. The used amplifier is also described below.

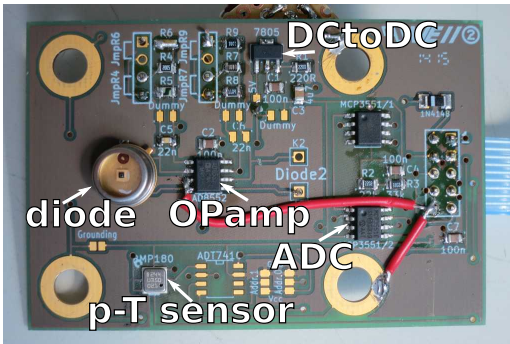
#### Photodiode

A SiC photodiode from *sflux Berlin* is employed in the detector setup. Its quadratic active surface area is  $0.5 \text{ mm}^2$ . Thus, the detector cross section is  $s_d \approx \sqrt{0.5} \text{ mm}$  and  $\gamma_c \approx 0.4^\circ$  (see Eq. (4.1)). This corresponds to a  $0.8^\circ$  FOV opening angle of the instrument.

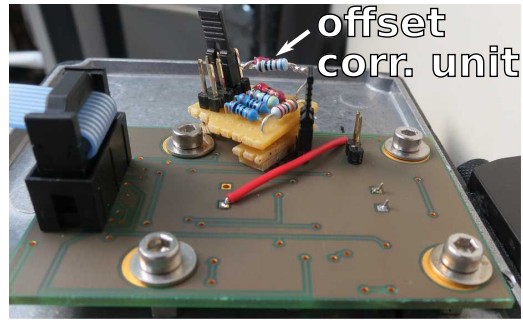
The spectral responsivity of SiC (Fig. 4.5) is advantageous for our measurement, compared to Si. Firstly, this excludes potential straylight from wavelengths  $\lambda > 400 \text{ nm}$ . Moreover, the spectral responsivity of SiC increases for decreasing wavelength in our measurement range. This increases the sensitivity, since the stronger  $\text{SO}_2$  absorption bands are weighted more strongly. The absolute responsivity of the SiC across the measurement wavelength range is  $\sim 0.11 \text{ A W}^{-1}$ . This is equivalent to a quantum efficiency of  $\sim 0.41 \text{ photoelectrons photon}^{-1}$ .

#### Amplifier

The amplifier circuit board (Fig. 4.6) used was originally designed for a different instrument by *Tirpitz (2014)*. From the two amplifier channels on this board, only one is used in the OP FPI  $\text{SO}_2$  instrument. The second channel can optionally be



(a)



(b)

**Figure 4.6** – Front side (a) and back side (b) of the amplifier circuit board. The SiC photodiode is directly mounted on the board with the OPamp, the ADCs and the DC to DC converter. A 10 pin ribbon cable connects the ADCs and the combined pressure and temperature sensor to the *Arduino* board. On the backside the resistor cascade of a variable offset correction that was added to the circuit is visible.

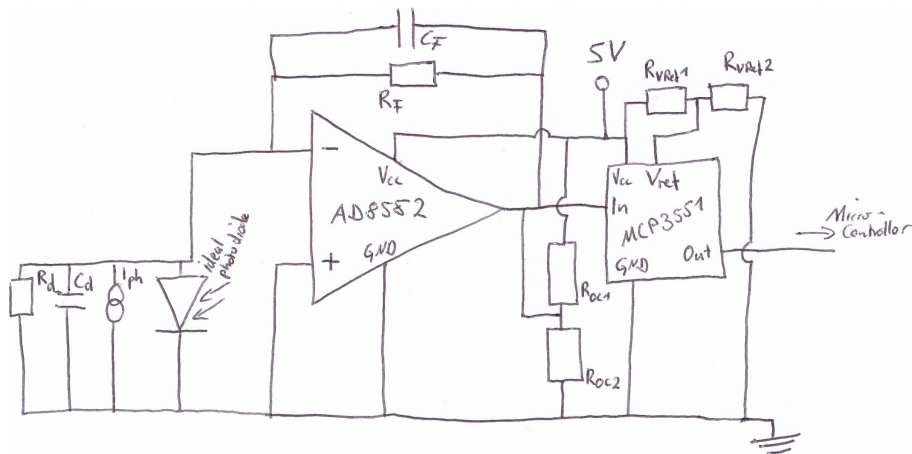


**Figure 4.7** – Schematic drawing of the amplifier circuit. On the left the photodiode equivalent circuit diagram is shown. The ideal photodiode is separated from its parallel resistance and capacitance. The OPamp with feedback loop, the offset correction and the ADC are depicted as well.

used to implement a two stage amplifier<sup>1</sup>. An operational amplifier (OPamp) and an analog to digital converter (ADC) are placed on the circuit board and supplied with a stabilized voltage of 5V from a DC to DC converter. The photocurrent  $I_{\text{ph}}$  of the SiC diode is converted to a proportional voltage  $U_{\text{out}}$  using a transimpedance amplifier circuit (Fig. 4.7, specifications in Tab. 4.1). The output voltage  $U_{\text{out}}$  is ideally determined by the feedback resistor  $R_F$  via:

$$U_{\text{out}} = I_{\text{ph}} R_F \quad (4.4)$$

This only holds for photodiode resistances  $R_d \gg R_F$ . For the high feedback resistances we employ, this simplification is not valid anymore and the output voltage is determined by:

$$U_{\text{out}} = I_{\text{ph}} \left( \frac{1}{R_d} + \frac{1}{R_F} \right)^{-1} \quad (4.5)$$

The feedback capacitance  $C_F$  and the feedback resistor  $R_F$  in the examined setups dominate the operational bandwidth  $\Delta f$  of the amplifier circuit and thus its time constant ( $\frac{1}{e}$  decay time):

$$\tau_{\text{RC}} = R_F C_F = \frac{1}{\Delta f} \quad (4.6)$$

The time constant regulates the tradeoff between noise (see below) and readout speed. The measurement is limited by the tuning process. The servo positioning velocity limits the measurement time resolution to the order of 10 Hz. The detector's bandwidth is set to  $\sim 8$  Hz.

The output voltage  $U_{\text{out}}$  is quantified by the ADC. The resolution of 21 bits and the reference voltage of 3 V determine the voltage resolution  $\Delta V_{\text{ADC}}$  per least significant bit (LSB):

$$\Delta V_{\text{ADC}} = \frac{3 \text{ V}}{2^{21}} = 1.43 \mu\text{V LSB}^{-1} \quad (4.7)$$

Due to the low radiances in the measurement wavelength range, the feedback resistance  $R_F$  is chosen very high. The input offset current of the OPamp therefore cause high offset voltages at the output. These are corrected by an offset correction circuit (also shown in Fig. 4.6) in order to prevent the ADC from overdrive. The whole amplifier board is mounted inside an aluminum housing for electromagnetic shielding.

#### 4.1.4 The combined instrument setup

The above described parts are combined in the OP FPI SO<sub>2</sub> instrument. Fig. 4.8 (a) and (b) show the device. The detector housing, the lense, the FPI mounting and

---

<sup>1</sup>A two stage amplifier makes for instance sense, when the noise is too small to be resolved by the ADC.

**Table 4.1** – parts and specifications of the amplifier circuit, shown in Fig 4.6 and 4.7

part	specification
photodiode	SiC, quantum efficiency $\sim 0.41$
OPamp	AD8552, 5 V supply voltage
ADC	MCP3551, 21 bit, 3 V reference
T/p sensor	BMP180, <i>Bosch</i>
$R_F$	250 M $\Omega$
$C_F$	0.5 nF
$R_{OC1}$	220 k $\Omega$
$R_{OC2}$	37.6 $\Omega$
$R_{Vref1}$	33 k $\Omega$
$R_{Vref2}$	22 k $\Omega$

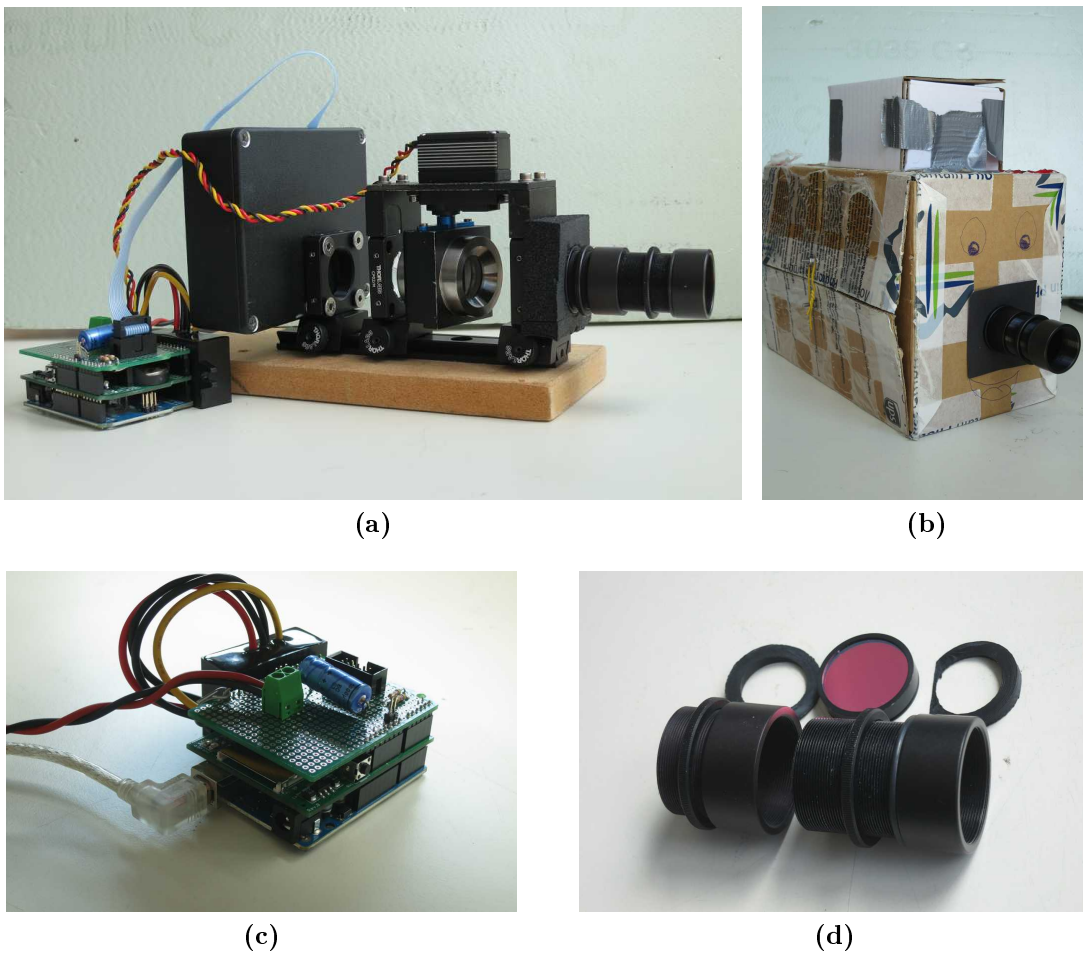


**Figure 4.8** – images of the full OP FPI SO<sub>2</sub> instrument setup without (a) and with (b) pasteboard housing. (c) *Arduino* board with SD card board. Power supply, servo plug and the ribbon cable plug are added on a separate board on top. (d) disassembled lens tube with BPF and tilting spacers.

the tube containing the BPF are fixed on an optical rail. The rail is mounted on a wooden board that can be placed inside the pasteboard camera housing.

A combined temperature and pressure sensor (*BMP108*) is additionally placed on the amplifier board. This sensor and the ADCs are read out by an *Arduino* microcontroller board. It offers the possibilities of saving the data on a memory card, and sending it to a display or a PC via serial communication. Moreover, the *Arduino* can generate pulse width modulated (PWM) signals to master the servo. The entire instrument software can therefore be written within the *Arduino* program environment, using libraries for readout and servo control options, provided by the manufacturers or the work of Tirpitz (2014).

A 12V battery supplies the whole setup with power. The power supply of the servo is decoupled by an additional DC to DC converter in order to avoid impacts of high currents on the amplifier circuit.

In table 4.2 all instrument parts are listed.

## 4.2 OP FPI SO<sub>2</sub> device - performance

In this section the performance of the instrument described above is examined. The low scattered light intensity in the measurement wavelength range requires a very sensitive detector. High noise levels are observed in the instrument signals. Noise sources are examined in Sect. 4.2.1. The SO<sub>2</sub> sensitivity and the cross interferences to the instrument response are discussed in Sect. 4.2.2 and 4.2.3, before improvement suggestions are listed (Sect 4.2.4).

### 4.2.1 Noise

The total noise of the instrument response  $\Delta AA$  determines the detection limit and the resolution of the SO<sub>2</sub> CD quantification. A practical measure for the instrument noise is the 'noise equivalent signal' (NES)

$$S_{\text{SO}_2, \text{NES}} = \frac{\Delta AA}{\chi_{\text{SO}_2}}, \quad (4.8)$$

where  $\chi_{\text{SO}_2} = \frac{dAA}{dS_{\text{SO}_2}}$  is the instrument's SO<sub>2</sub> sensitivity.

The AA consists of radiance measurements that are on the one hand influenced by photo electron shot noise and on the other hand by electronic noise of the detector unit. Moreover, the servo's positional accuracy and repeatability contribute to the total noise of the instrument response. In the following the different contributions are explained and their weights are estimated.

**Table 4.2** – List of parts for the OP FPI SO<sub>2</sub> prototype; prices are in Euro, without taxes

<b>part</b>	<b>#</b>	<b>supplied by</b>	<b>spec.</b>	<b>price</b>	<b>comment</b>
<b>optical setup</b>					
FPI	1	<i>SLS Optics Ltd.</i>		~ 4400	
BPF	1	<i>bk</i>	bk-280-310-S	299	
SiC photodiode	1	<i>sglux Berlin</i>	SG01D-5	53	
fused silica lens 1"	1	<i>Thorlabs</i>	LA4148-UV	96.22	
rail	1	<i>Thorlabs</i>	RLA150/M	34.80	
rail carrier	3	<i>Thorlabs</i>	RC1	21.01	
lens carrier 1"	1	<i>Thorlabs</i>	CP02/M	13.92	add. threads
tube carrier 1.2"	1	<i>Thorlabs</i>	CP12	17.40	add. threads
lens tube	1	<i>Thorlabs</i>	SM1V05	25.75	
lens tube	1	<i>Thorlabs</i>	SM1M10	11.53	
diode board	1			~ 15	see Fig. 4.1
diode board housing	1				aluminum
<b>servo and mount</b>					
servo	1	<i>Hitec</i>	HS-7955TG	73.71	
servo arm	1	<i>robbe</i>		6.28	
servo mount	1				aluminum
vertical spacer	2				aluminum
FPI mount	1				aluminum
<b>electronics</b>					
microcontroller	1	<i>Arduino</i>	Arduino UNO	15	
DC to DC conv.	1				for servo

## Noise in the radiance measurement

The radiance arriving at the active detector area is converted into a photo current  $I_{\text{ph}}$ . Via a transimpedance amplifier, the photo current is further converted into a proportional output voltage  $U_{\text{out}}$  and further digitized by the ADC.

The first conversion is determined by the quantum efficiency of the detector (see Sect. 4.1.3). The photons reach the detector independently and with a constant rate within the radiance measurement period. Thus, they obey Poisson statistics. The electrons that are released by the photons from the photodiode's active area behave equally since the quantum efficiency is basically a constant. The rms (root mean square) noise of  $N_e$  photoelectrons released from the detector is thus  $\sqrt{N_e}$ . This so called photo electron shot noise is therefore a radiance dependent noise source. The radiance measurement period is typically determined by the time constant of the setup  $\tau = \frac{1}{\Delta f}$ . The photo electron number  $N_e$  of the photo current  $I_{\text{ph}}$  causing an output voltage  $U_{\text{out}}$  is:

$$N_e(U_{\text{out}}) = \frac{U_{\text{out}}}{e \Delta f R_F}, \quad (4.9)$$

with the feedback resistance  $R_F$ , the charge  $e$  of an electron and the bandwidth  $\Delta f$  representing the measurement period. For  $R_F = 250 \cdot 10^6 \Omega$ , one ADC LSB  $\Delta V_{\text{ADC}} = 1.43 \mu\text{V LSB}^{-1}$  would thereafter correspond to  $\sim 4200$  photoelectrons (or  $\sim 10000$  photons) in the measurement period  $\frac{1}{\Delta f} = 0.125$  s.

The contribution  $\Delta U_{\text{sn}}$  to the output voltage rms noise  $\Delta U_{\text{out}}$  is then:

$$\Delta U_{\text{sn}} = \sqrt{U_{\text{out}} e \Delta f R_F} \quad (4.10)$$

Typical photo currents in the examined device amount to some hundreds of pA.

The noise contribution of the amplifier electronics is very important to include in the noise considerations, since the photo currents in our case are very low. Thermal excitation of electrons in an electrical conductor cause resistance dependent noise that disturbs the photo current measurement. Moreover, noise from the OPamp's input is present.

In Fig. 4.7 the noise sources of the different components are indicated. The thermal noise of the feedback resistor  $R_F$  is

$$\Delta U_{R_F} = \sqrt{4 k_B T R_F \Delta f}. \quad (4.11)$$

It directly contributes to the electronic output voltage noise  $\Delta U_{\text{out,electr}}$ . The realistic photodiode also has a finite resistance  $R_d$  with a thermal noise contribution. Since the circuit can be viewed as an inverting operational amplifier, the noise contribution of the photodiode is amplified by a factor of  $\frac{R_F}{R_d}$ :

$$\Delta U_{R_d} = \frac{R_F}{R_d} \sqrt{4 k_B T R_d \Delta f} \quad (4.12)$$

**Table 4.3** – List of the noise sources contributing to the total radiance measurement noise  $\Delta U_{\text{out}}$  of the detector units output voltage.

source	noise at output [ $\mu\text{V}_{\text{rms}}$ ]	noise [ $\text{LSB}_{\text{rms}}$ ]
$\Delta U_{R_F}$	5.8	4.1
$\Delta U_{R_d}$	10.8	7.6
$\Delta U_{\text{OPu}}$	0.4	0.3
$\Delta U_{\text{OPi}}$	1.1	0.8
$\Delta U_{\text{ADC}}$	2.5	1.7
$\Delta U_{\text{out,electr}}$	12.6	8.8
$\Delta U_{\text{sn}}(I_{\text{ph}} = 150 \text{ pA})$	1.7	1.2
$\Delta U_{\text{out}}$	12.7	8.9

Similarly, the OPamp's input voltage noise  $\Delta U_{\text{OPu}}$  and input current noise  $\Delta U_{\text{OPi}}$  contribution to  $\Delta U_{\text{out,electr}}$  are determined:

$$\Delta U_{\text{OPu}} = \frac{R_F}{R_d} u_{\text{OP}} \sqrt{\Delta f} \quad (4.13)$$

$$\Delta U_{\text{OPi}} = \frac{R_F}{R_d} i_{\text{OP}} \left( \frac{1}{R_F} + \frac{1}{R_d} \right)^{-1} \sqrt{\Delta f} \quad (4.14)$$

$u_{\text{OP}}$  and  $i_{\text{OP}}$  are the respective noise densities, specified in the OPamp's data sheet. All these noise sources are assumed to have a white spectrum and are therefore proportional to the square root of the bandwidth. In our case the bandwidth is  $\sim 8 \text{ Hz}$ , dominated by the low pass filter of the feedback loop. The photodiode resistance  $R_d \sim 70 \text{ M}\Omega$  was inferred from noise measurements and validated for different feedback resistors.

The ADC contributes to the noise with its constant output noise of  $\Delta U_{\text{ADC}} = 2.5 \mu\text{V}_{\text{rms}}$ .

In Fig. 4.9 the contributions to the total electronic noise  $\Delta U_{\text{out,electr}}$  are plotted as a function of the feedback resistor  $R_F$ . The independent noise sources sum up in a root sum of squares:

$$\Delta U_{\text{out,electr}} = \sqrt{(\Delta U_{R_f})^2 + (\Delta U_{R_d})^2 + (\Delta U_{\text{OPu}})^2 + (\Delta U_{\text{OPi}})^2 + (\Delta U_{\text{ADC}})^2} \quad (4.15)$$

The electronic noise contribution is not dependent on the incident radiance. The gray line shows the photo electron shot noise contribution for a typical photo current ( $\sim 150 \text{ pA}$ ). Additionally, in the lower panel, the SNR of the radiance measurement is plotted. The right ordinate axis of the upper panel shows the feedback capacitance needed for the  $8 \text{ Hz}$  bandwidth (blue line) of the investigated setup.

The vertical dashed line marks our configuration with the  $250 \text{ M}\Omega$  feedback resistor. The noise contributions for this setup are listed in Tab. 4.3.

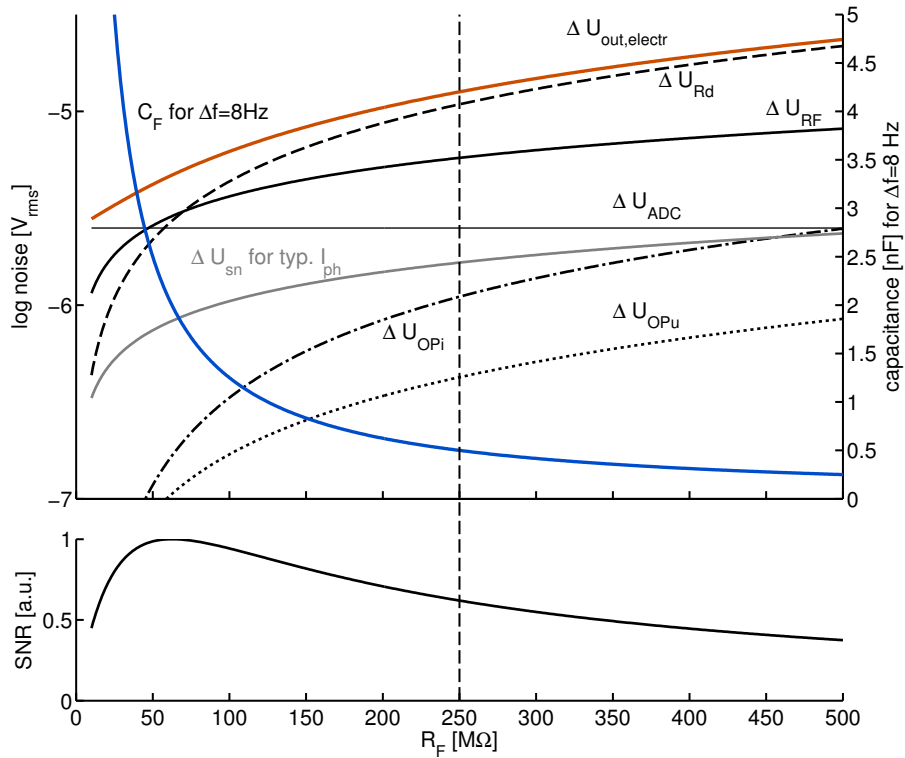


**Figure 4.9** – Upper panel: noise contributions to the output voltage  $\Delta U_{\text{out,electr}}$  of the radiance detector as a function of the feedback resistor  $R_F$ :  $\Delta U_{R_F}$  thermal noise of  $R_F$ ,  $\Delta U_{R_d}$  thermal noise of the diode resistance  $R_d$ ,  $\Delta U_{\text{OPi}}$  and  $\Delta U_{\text{OPu}}$  input current and voltage noise of the OPamp,  $\Delta U_{\text{ADC}}$  ADC output noise;  $\Delta U_{\text{sn}}$  (gray) is the photo electron shot noise for typical radiance; the blue line shows the feedback capacitance  $C_F$  required for a bandwidth of 8 Hz; in the lower panel, the relative SNR of the radiance measurement is plotted also as a function of  $R_F$ . It peaks at  $R_F = R_d$ .

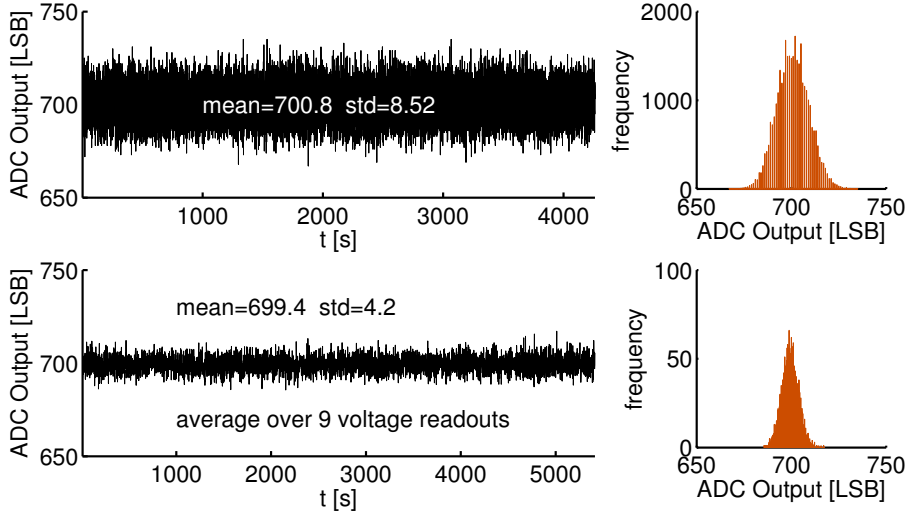


**Figure 4.10** – Measurement of the electronic noise  $\Delta U_{\text{out,electr}}$  (dark measurement). In the upper panel the readout frequency was approximately the bandwidth of the circuit. In the lower panel a measurement with the average of 9 voltage readouts is plotted. On the right the histograms are shown.

For the discussed setup, the noise in the radiance measurement is dominated by the thermal noise of the photodiode resistor and feedback resistor. The input noise of the OPamp and photo electron shot noise are only minor contributions. The SNR of the radiance measurement peaks at around  $R_F = R_d$ . In this consideration the finite photodiode resistance was taken into account for the signal calculation of the transimpedance amplifier (see Eq. (4.5)). For the feedback resistors we use, this becomes significant. We used the suboptimal  $250 \text{ M}\Omega$  feedback resistance because the relation was noticed too lately.

The noise in the radiance measurement can be decreased by averaging over several independent voltage readouts. The noise of such an averaged signal  $\bar{U}_{\text{out}}$  of  $N$  independent measurements is

$$\Delta \bar{U}_{\text{out}} = \frac{\Delta U_{\text{out}}}{\sqrt{N}} \quad (4.16)$$

However, the higher acquisition time per radiance measurement leads to a lower time resolution of the measurement.

Figure 4.10 shows two dark radiance measurements. The upper panel shows the result for the voltage readout at approximately  $\Delta f = \frac{1}{R_F C_F}$ . The lower panel shows the result for a separate measurement, where the instrument software averaged over nine voltage readouts. The rms noise is not by a factor of  $\sqrt{9} = 3$  smaller, as expected above. The readout frequency is most likely too high, since the voltages are still correlated by about  $\frac{1}{e}$ .

The noise of  $\sim 8.5 \text{ LSB}$  in the unaveraged dark measurement matches well to our

estimate of 8.9 LSB (see Tab. 4.3). The offset of  $\sim 700$  LSB is the residual offset after the rough offset correction circuit.

Via Gaussian error propagation the noise in the AA due to the radiance measurement noise  $\Delta AA_{\text{rad}}$  can be determined. The AA consists of four radiance measurements:

$$AA = -\log \frac{I_A I_{B,0}}{I_{A,0} I_B} \quad (4.17)$$

The error is determined by

$$\Delta AA_{\text{rad}} = \sqrt{\sum_i \left( \frac{\partial AA}{\partial I_i} \Delta I_i \right)^2} = \sqrt{\sum_i \left( \frac{\Delta I_i}{I_i} \right)^2} \quad (4.18)$$

for the individual radiance measurements  $I_i$ . For a typical photo current, measured in Heidelberg in the end of May, the AA error for 8 Hz readouts would be  $\Delta AA_{\text{rad}} \approx 0.003$ . Integrating over 8 readouts would mean a measurement time resolution of  $\sim 4$  s. The noise would thereby ideally be reduced to  $\Delta AA_{\text{rad}} \approx 0.001$ .

## Tuning noise

Apart from the noise of the radiance measurements, there is also noise in the tuning process. In our case, the accuracy of the servo and its repeatability are crucial. In the first prototype setup the FPI is directly mounted at the servo shaft (see e.g. Fig. 4.4 (b)). Hence, the servo's angle accuracy equals the tilt accuracy of the FPI. Every servo jittering directly results in a servo tilt jittering. The angular accuracy of the servo motor was determined to  $\Delta \omega \approx 0.2^\circ$ . This is strongly influenced by occasional jittering.

Fig. 4.3 shows how the optical density  $\tau_{\text{FPI}}$  changes with the FPI tilt angle  $\omega$ . For the setting B at  $0^\circ$  tilt the measurement is hardly sensitive on small tilt variations. In setting A, however, the sensitivity is higher. Figure 4.11 shows a magnification of Fig. 4.3 at around  $\omega = 5^\circ$ . When setting A is known well, the impact of the tilt imprecision is moderate. For a FOV of  $1^\circ$ ,  $\Delta \omega$  leads to a variation of  $\Delta \tau_A \approx 0.003$ , when choosing setting A at  $\omega_A = 5.2^\circ$ . For the choice  $\omega_A = 5.5^\circ$ , the deviation is already  $\Delta \tau_A \approx 0.02$ . The noise in  $\tau_A$  in this case directly determines the noise in AA.

The FPI settings for the measurement have to be chosen carefully. The sensitivity decreases for a badly chosen setting. Moreover, the noise due to servo imprecision increases substantially.

The tuning noise of the simple prototype setup is expected to dominate the total noise in the AA. For this proof of concept study the noise of  $\Delta AA = 0.02$  is acceptable.

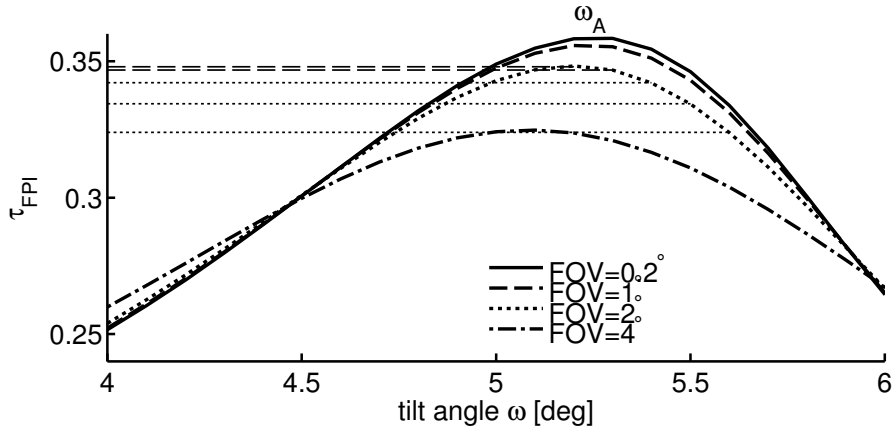


**Figure 4.11** – magnification of a part of Fig. 4.3. The noise due to servo imprecision is strongly dependent on the selected tilt settings. The horizontal lines show for two cases, how a tilt noise  $\Delta\omega = 0.2^\circ$  affects the noise in the instrument response.

**Table 4.4** –  $\text{SO}_2$  Column densities of the gas cells used in the OP FPI  $\text{SO}_2$  device characterization; determined with the DOAS technique.

cell	$\text{SO}_2$ CD [ $10^{18}$ molec $\text{cm}^{-2}$ ]	uncertainty [ $10^{18}$ molec $\text{cm}^{-2}$ ]
k1	0.43	0.03
k2	0.81	0.03
g1	1.13	0.05
g2	2.45	0.05
g3	3.99	0.06

### 4.2.2 $\text{SO}_2$ sensitivity

In this subsection, the  $\text{SO}_2$  sensitivity  $\chi_{\text{SO}_2}$  of the OP FPI  $\text{SO}_2$  device is investigated. Gas cells with a fixed amount of  $\text{SO}_2$  were used in this study. The respective  $\text{SO}_2$  CDs are known from DOAS measurements. Table 4.4 lists the available cells.

The servo is able to perform a tilt scan in small steps. Such scans were performed with and without an  $\text{SO}_2$  cell (g2) inside the instrument FOV. The upper panel of Fig. 4.12 shows the modulation of the measured radiances (in units of ADC LSBs) as a function of the servo position. The  $I_0$  measurement (no  $\text{SO}_2$ , orange) is an average of seven individual scans (thin black lines). For the  $I$  measurement (with  $\text{SO}_2$  cell, blue), 16 individual scans were averaged. The lower panel shows the optical density  $\tau_{\text{FPI}}$ , seen through the FPI for each tilt position. The progression is qualitatively very similar to the simulated  $\tau_{\text{FPI}}$ , shown in Fig. 4.3. Note, that in the simulation slightly different instrument parameters were used. The sequential peaks in the measured optical density most likely represent the FPI transmission being shifted across the  $\text{SO}_2$  absorption peaks. The offset in the measured  $\tau_{\text{FPI}}$  (Fig. 4.12 lower panel) is not only caused by the broadband  $\text{SO}_2$  absorption in the wavelength

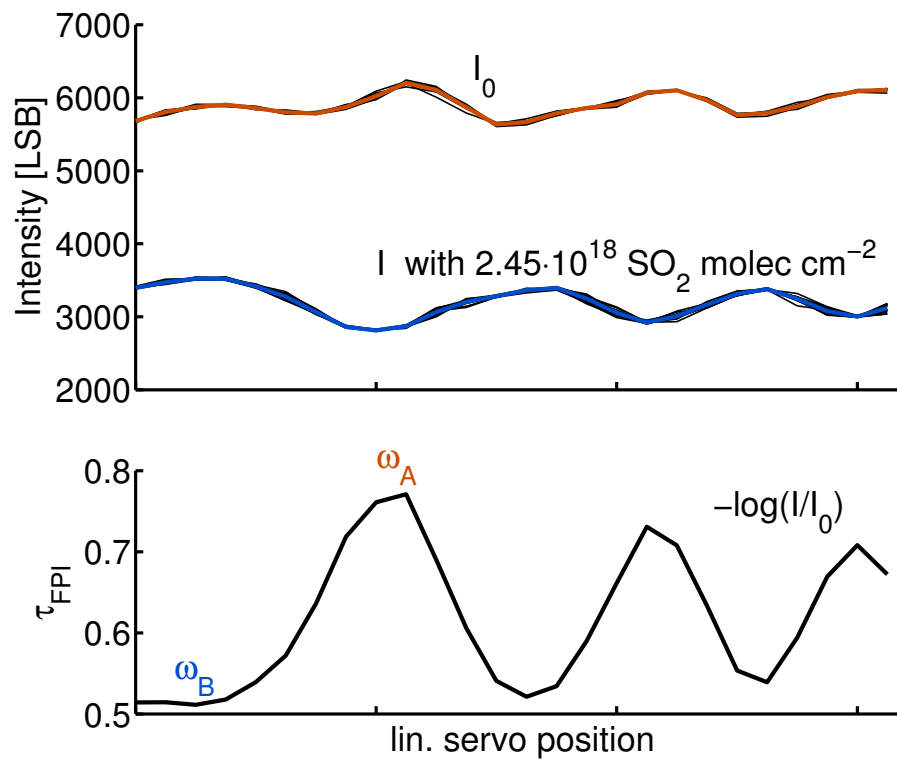


**Figure 4.12** – Upper panel: Progression of the measured radiance as a function of the servo position (approximately proportional to the tilt angle). In blue (orange) the averaged tilt scan with (without) an  $\text{SO}_2$  gas cell is shown. The thin black lines represent the individual scans. In the lower panel, the optical density seen through the FPI is plotted.  $\omega_i$  for the respective measurements settings  $i = A, B$  are suggested.

range but also by reflections at the gas cell or similar effects.

The progression of  $\tau_{\text{FPI}}$  over the servo position allows us to determine suitable values for the settings A and B of the AA measurement. In order to have maximum stability and sensitivity, the broadest extrema (at low  $\omega$ ) of  $\tau_{\text{FPI}}$  should be chosen.

Figure 4.13 shows a OP FPI SO<sub>2</sub> measurement with two settings A and B for the different gas cells. In sub figure (a), the measured radiances ( $I_A$  and  $I_B$ ) are plotted. They were recorded by continuously tilting the FPI from  $\omega_A$  to  $\omega_B$ . Additionally to the SO<sub>2</sub> containing gas cells, an empty cell was evaluated. In sub figure (b) the logarithm of the ratio of the two radiances is plotted. The AA is defined as the relative changes of this ratio compared to a reference (in this case the 'no cell' measurement).

It is clearly visible, how the radiance in FPI setting A ( $I_A$ ) is stronger affected by the SO<sub>2</sub> absorption. This is expected, since in setting A the FPI transmission correlates with the SO<sub>2</sub> absorption peaks. For each gas cell, a constant offset in the radiance ratio is observed. The noise is, as discussed above, mainly due to the servo's imprecision.

For the individual gas cells this offset (the AA) is plotted in Fig. 4.14. There is a clear correlation of the AA with the SO<sub>2</sub> CDs determined with the DOAS technique. When roughly estimating a linear relation for small SO<sub>2</sub> CDs (thick red line), the flattening of the calibration curve due to saturation effects can be guessed. The positioning of the gas cells inside the light path (also in the DOAS measurement) is crucial, since different tilts can increase the light path and therefore affect the measurement.

From the slope of the AA in Fig. 4.14, the SO<sub>2</sub> sensitivity of the prototype is determined to  $\chi_{\text{SO}_2} \approx 10^{-19}$  molecules<sup>-1</sup> cm<sup>2</sup>. The rms noise in the logarithmic radiance ratios is approximately 0.006. This means that the noise in the AA is

$$\Delta\text{AA} = \sqrt{2 \cdot 0.006^2} = 0.0085 \quad (4.19)$$

since it is determined by a background and a trace gas measurement. The NES is therefore

$$\text{NES}_{\text{SO}_2} = \frac{0.0085}{10^{-19}} = 8.5 \cdot 10^{16} \text{ molec cm}^{-2} \text{ or } 34\text{ppm m} \quad (4.20)$$

for a measurement period of  $\sim 1$  s.

For statistic noise and a stable background, one averaged background measurement could be recorded with reduced uncertainty. In this case, the NES would be even lower ( $\sim 6 \cdot 10^{16}$  molec cm<sup>-2</sup> or  $\sim 24$ ppm m).

The noise in the detector offset measurement is expected to be statistic. The offset measurement was averaged over 1000 readouts and its noise was neglected in the calculations.

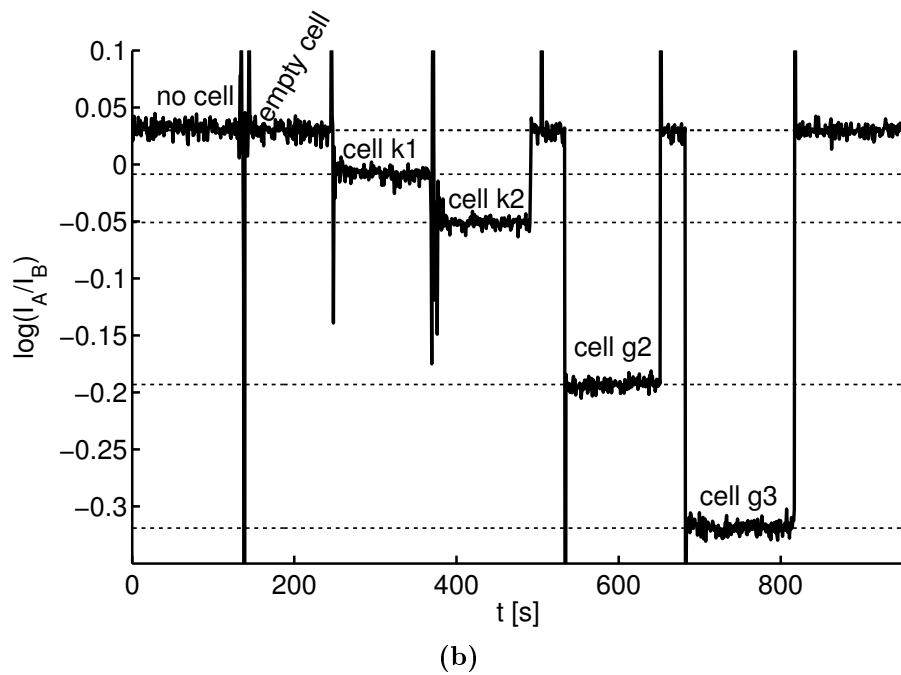
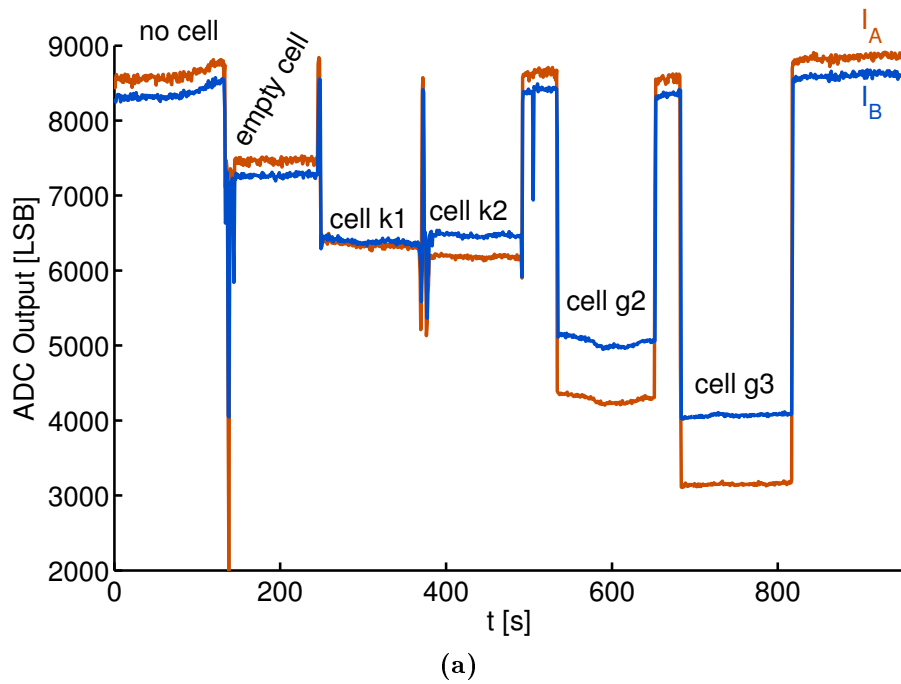


**Figure 4.13** – Results of a OP FPI  $\text{SO}_2$  measurement of the different gas cells (cell g1 was not available at that time). **(a)**: radiances  $I_A$  and  $I_B$  for the two FPI tilt settings  $\omega_A$  and  $\omega_B$ . **(b)**: logarithm of the ratio of  $I_A$  and  $I_B$ . It is proportional to the AA. A clear correlation with the  $\text{SO}_2$  CD is observed.

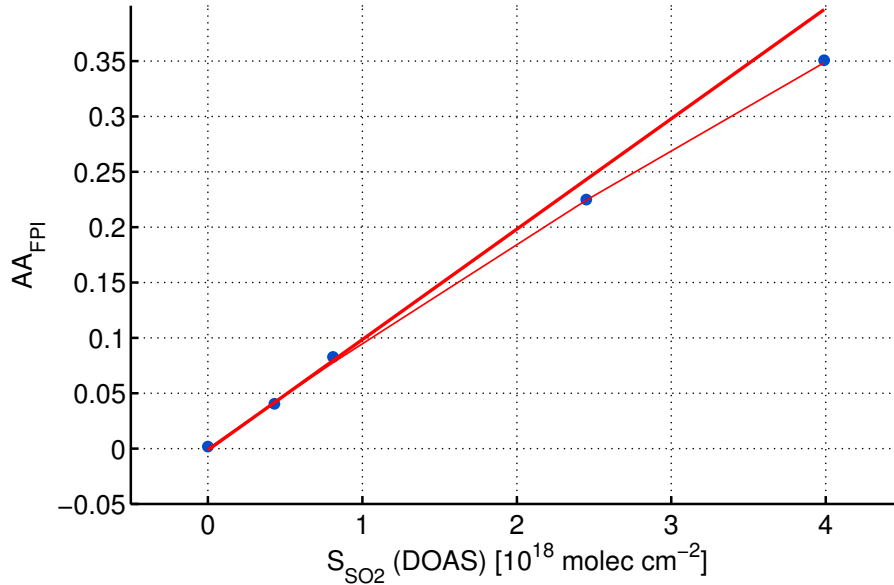


**Figure 4.14** – Measured calibration curve for the OP FPI  $\text{SO}_2$  instrument. The expected saturation effects for higher  $\text{SO}_2$  CD is observed. The small deviations most likely come from inaccurate positioning of the gas cells (in the DOAS or in the FPI measurement).

### 4.2.3 Stability

The upper panel of Fig. 4.15 shows a measurement sequence of the radiances  $I_A$  and  $I_B$  of around 5.5 hours with constant viewing direction. It was taken at the 9th of June in Heidelberg at partly cloudy conditions. The clouds are responsible for the high radiance variations. The temperature of the diode board is plotted in gray. It varies in a  $10^\circ\text{C}$  range and does not seem to have any impact on the measurement. The increase at around 17:00 local time is caused by direct exposition of the device to sunlight.

In the middle panel, the SZA is plotted. Within the measurement period it changes from  $27^\circ$  to more than  $70^\circ$ . In the lower panel the logarithm of the ratio of  $I_A$  and  $I_B$ , determining the AA, is shown. Until around 18:00 local time, it is approximately constant. Then, the value is slightly lower and gets increasingly noisy due to the reduced radiances (sunset). At around 16:30 the signal gets noisier, this can either be caused by special state of the cloud cover or unknown instabilities in the setup (e.g. of the servo). For comparison, the impact on the logarithmic ratio of the gas cell k1 is also plotted (dotted red line).

From the beginning of the measurement until 18:00 the SZA changes from  $27^\circ$  to roughly  $60^\circ$ . Thereby the geometric light path in the stratosphere increases by the factor  $\sim 1.78$ . For a stratospheric ozone vertical column of 300 DU this would correspond to an ozone slant column change of  $\sim 260$  DU. The measurement proves the tremendously lower ozone interference of the FPI method compared to filter based  $\text{SO}_2$  Cameras.

Another substantial advantage of the FPI method is the stability toward a cloudy

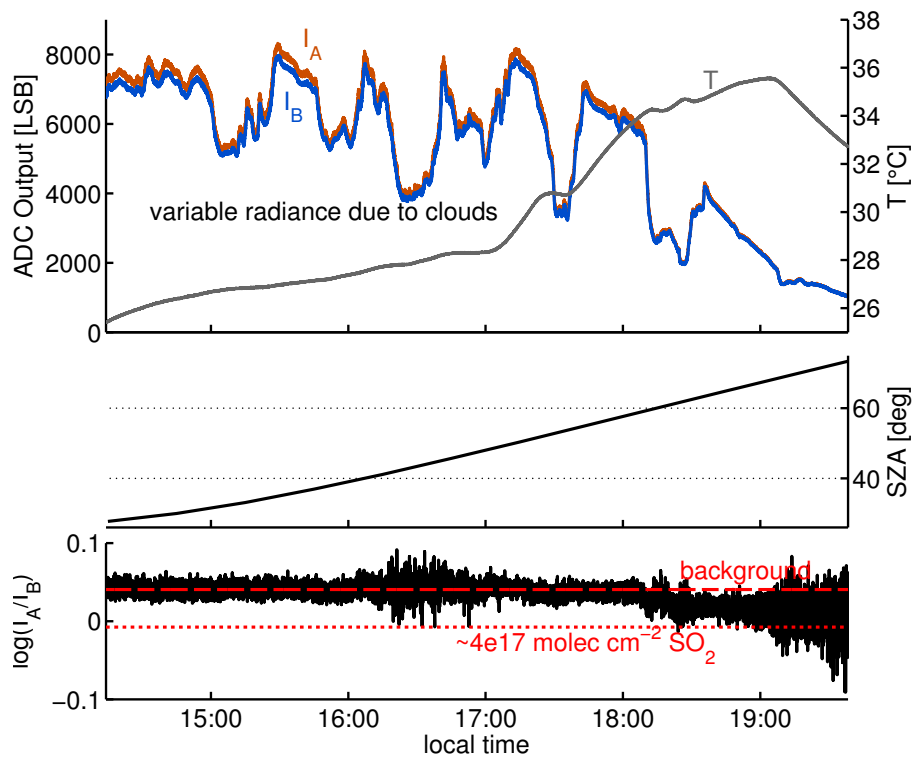


**Figure 4.15** – Long measurement time series of  $I_A$  and  $I_B$  in order to examine the instrument signal's stability. Compared to filter based  $\text{SO}_2$  Cameras, the performance of the FPI measurement is significantly more stable toward cloud impacts and ozone background variations caused by SZA changes. The dotted red line in the lower panel shows, how an  $\text{SO}_2$  CD of  $\sim 4 \cdot 10^{17} \text{ molec cm}^{-2}$  would affect the recorded instrument signal. The red dashed line indicates an average over the signal from the beginning until around 16:00.

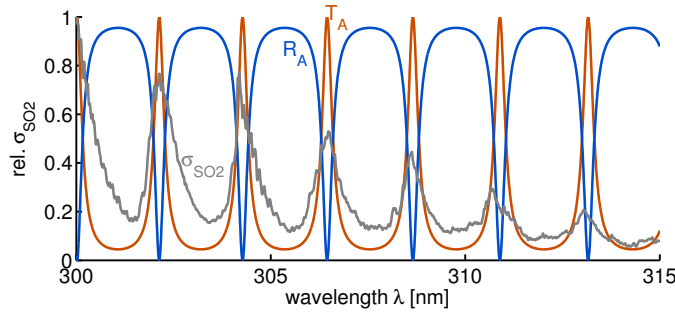


**Figure 4.16** – FPI transmission  $T_A$  and reflection  $R_A$  spectrum in FPI setting A. The reflection can be used to replace setting B in the measurement. A setup with no movable parts can thereby be realized. In addition,  $I_A$  and  $I_B$  can be recorded at the same time. In gray the  $\text{SO}_2$  absorption cross section is plotted.

background. With filter based  $\text{SO}_2$  Cameras a blue sky is required.

#### 4.2.4 Improvement suggestions

From the above considerations, several improvement suggestions become obvious. Since the imprecision of the servo dominates the noise, a more precise servo or a transmission gear can be used. Once the noise in the radiance measurement dominates, a parallelization optics and large aperture lenses can be used to increase the instrument etendue. This setup is described in more detail in Sect. 5.1. In principle, thereby, a photo electron shot noise dominated radiance measurement can be reached.

#### The transmission reflection setup

There is a different experimental setup, that allows to build OP FPI  $\text{SO}_2$  instruments without movable parts but with comparable sensitivity. In this setup, the incoming narrow light beam arrives at an FPI in a slightly tilted position. The tilt position corresponds to an FPI transmission setting A. Two photodiodes are employed to detect the transmitted and the reflected light from the FPI. The reflected light is determined by the spectral reflectivity of the FPI that is

$$R_{\text{FPI,A}} = 1 - T_{\text{FPI,A}} \sim T_{\text{FPI,B}}. \quad (4.21)$$

The optimum finesse for a reflection transmission setup is likely different as for the tuning setups considered above. Transmitted and reflected light can be detected at the same time in this method, so there are reduced errors due to the time lags in between measurement  $I_A$  and  $I_B$  compared to tuning methods. Imbalances (e.g. drifts) of the two required detector units can, however, cause problems.

## 4.2.5 Conclusion

A OP prototype of an FPI SO<sub>2</sub> remote sensing device was built, in order to validate the FPI remote sensing method introduced and modeled in Chap. 2 and Chap. 3. With this simple prototype construction, SO<sub>2</sub> could be quantified and a calibration curve could be recorded. Compared to the filter based SO<sub>2</sub> Camera, drastically reduced cross interferences to ozone and clouds could be demonstrated. Hence, the instrument would already be suited for employment in volcanic field practice. Its SO<sub>2</sub> NES of  $\sim 8.5 \cdot 10^{16}$  molec cm<sup>-2</sup> or  $\sim 34$  ppm m is sufficient for the typical SO<sub>2</sub> emission of many volcanoes. For instance, typical SO<sub>2</sub> CDs measured at Mount Etna in Italy are in the range of  $\sim 10^{18}$  molec cm<sup>-2</sup> (see e.g. [Bobrowski and Giuffrida, 2012](#)).

A major advantage of the FPI technique over the dispersive DOAS technique is the feasibility of an implementation in a fast imaging device.

## 5 FPI imaging applications

In the former chapters, the principle of remote sensing of gases in the UV with an FPI was investigated and proven experimentally for SO<sub>2</sub>. Compared to the SO<sub>2</sub> Camera, a higher sensitivity and a far higher selectivity are reached (see Sect. 3.2.2). The potential of the technique of being implemented in a fast imaging instrument is a substantial advantage over the dispersive DOAS technique. There are several approaches to the FPI imaging application that will be introduced in this chapter. [Pisani and Zucco \(2009\)](#) developed an imaging spectrometer with an FPI that was tuned via surface displacement modulation. However, only color was retrieved. A similar setup was proposed for SO<sub>2</sub> in [Kuhn et al. \(2014\)](#). The practical implementation of an FPI for UV SO<sub>2</sub> measurements by surface displacement tuning is complex (see Sect. 4.1.1). Hence, in this chapter, only methods, that are feasible with the air spaced FPI with fixed surface separation, used in the OP FPI SO<sub>2</sub> device are investigated. The different methods are compared by their effective etendue per pixel (determining the potential time resolution of the instrument), the data acquisition and required evaluation effort, and practical feasibility.

The methods are categorized by their acquisition mode of spatial information. After briefly discussing spatial scanning with the OP FPI device in Sect. 5.1, full frame imaging approaches with (Sect. 5.2) and without (Sect. 5.3) parallelizing the radiation from the FOV are introduced.

### 5.1 Scanning OP FPI device

A straightforward FPI imaging approach is to employ a OP FPI SO<sub>2</sub> device in a spatial scanning scheme, similarly to whisk broom imaging DOAS. An advantage of the FPI device is the high instrument etendue, that can be reached. In the setup, introduced in Chap. 4, the etendue is bound to the instrument FOV. With an additional parallelizing optics (see Fig. 5.1), a higher etendue can be achieved for a constant instrument FOV, employing a large aperture lens (lens 3). The etendue is limited by the FPI clear aperture and the incident solid angle of radiation, determined by  $\alpha_{\max} \approx 2^\circ$ .

The etendue of a spectrometer is determined by its entrance slit and the spectrometer's optical setup. The USB 2000+ from *Ocean Optics* is routinely employed for volcanic SO<sub>2</sub> measurements. It has an entrance slit of 1 mm × 50 μm and a *f*/4 - optics.

In Table 5.1 the calculations of the examined methods are summarized. The OP FPI SO<sub>2</sub> device can yield an up to 100 times higher effective etendue per pixel than

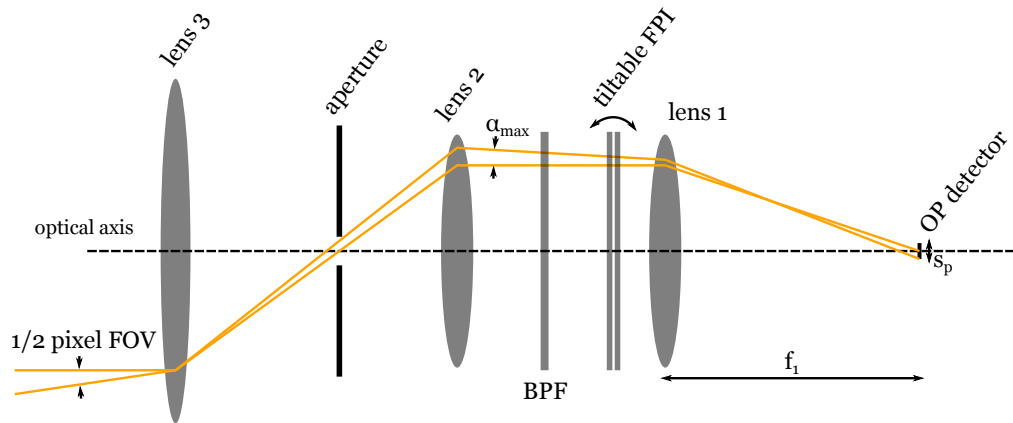


**Figure 5.1** – OP FPI SO<sub>2</sub> device with optics that allows to increase the etendue for a fixed instrument FOV. The clear aperture of lens 3 compensates the fixed FOV solid angle.

the spectrometer. This means that theoretically, for the same SNR, the acquisition time of the OP FPI SO<sub>2</sub> device is by a factor of  $\sqrt{100} = 10$  times shorter.

The mechanical scanning schemes will most likely limit the image acquisition time. The advantage of the dispersive DOAS measurement is to be able to detect several gas species (e.g. OClO, BrO) with one instrument and one spectral radiance acquisition. Moreover, it is routinely used and thus well investigated. The OP FPI SO<sub>2</sub> device, is stable and can be built compact. It would be considerably more interesting for volcanic applications, if there was a significant cost advantage.

## 5.2 Parallelized beam

Figure 5.2 shows the simulated ring symmetry of the SO<sub>2</sub> optical density on a camera's detector, when a suitable FPI is placed inside the light path. These ring structures are challenging to deal with (see Sect. 5.3), since for discrete tuning steps, they lead to inhomogeneous sensitivity across the detector. In order to bypass these complications, an optics that parallelizes light from the camera FOV before projecting it onto the detector, can be used. Figure 5.3 sketches a possible setup. An aperture and a lens (lens 2) determine  $\alpha_{\max}$  to around 2°. The orange circle in Fig. 5.2 marks the solid angle of the radiation incident on the FPI after parallelization. The SO<sub>2</sub> optical density in this circle is roughly homogeneous. However, for a camera FOV of 10° the etendue is by a factor of  $\left(\frac{\sin 2^\circ}{\sin 10^\circ}\right)^2 \approx 0.04$  smaller as for a non parallelizing method (see also Tab. 5.1). For the parallelized light beam, there are several feasible FPI tuning methods.

### 5.2.1 Tilt tuning

A tiltable FPI is indicated in Fig. 5.3 in the parallelized light path. Principally this is a feasible setup. However, when tilting the FPI, the ring symmetry will get

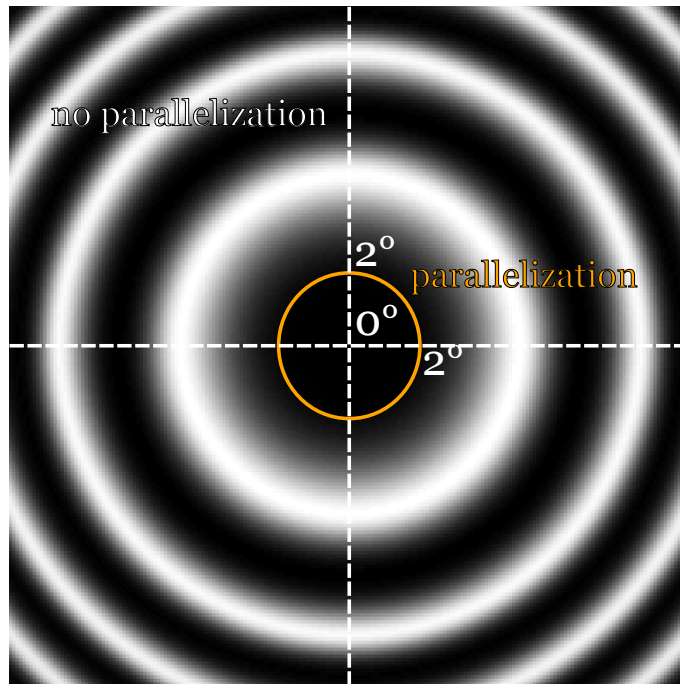


**Figure 5.2** –  $\text{SO}_2$  optical density across a camera FOV of  $20^\circ$  (edge to edge) when the FPI is placed in front of the camera. In order to simplify the data evaluation, the light can be parallelized by an additional optics. The resulting FPI incidence angle range is indicated by the orange circle. Note that thereby the etendue of the instrument is reduced.

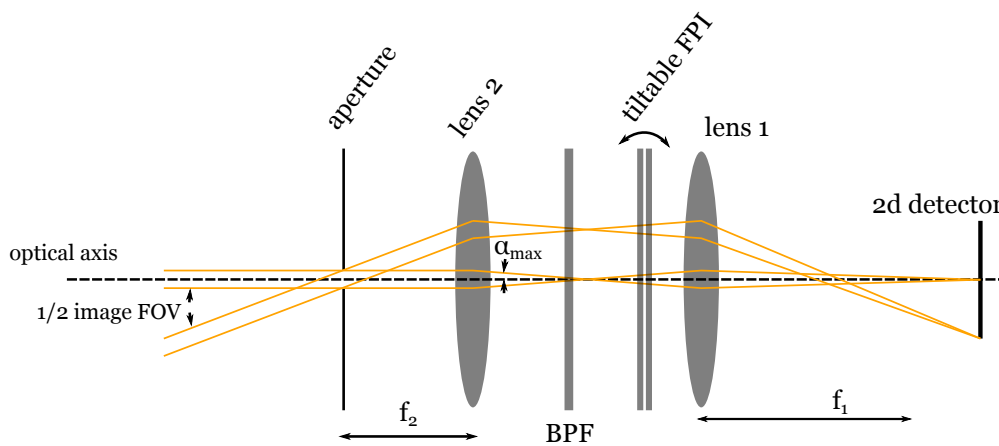


**Figure 5.3** – Optical setup of an FPI camera with an optics that parallelizes light from the camera FOV. The aperture size determines the degree of parallelization and thereby the instrument etendue. Within the parallelized light path the FPI can be placed and tuned, either by tilting (as indicated) or by modulating the refractive index  $n$  in between the two FPI surfaces.

distorted. The tilt affects the FPI incident angles differently, according to the tilt direction and the tilt axis. For non zero FPI tilts, a higher degree of parallelization might be required. Thereby the etendue further decreases.

Due to the thick quartz plates of the FPI ( $\sim 10$  mm, each), tilting can also affect the imaging properties of the setup.

### 5.2.2 Pressure tuning

Another tuning option is the pressure tuning option, already outlined in Sect. 4.1.1 for the OP FPI device. With the FPI mounted inside a box with varying pressure of a gas with high refractive index, the symmetry of the rings would not be affected by tuning. Two pressure settings, achieved by for instance a piston design are necessary (as employed in GCS instruments, see e.g. [Wehr et al., 2003](#)). Compared to other tuning methods this kind of tuning mechanics is rather complex to build.

### 5.2.3 Aperture tuning

The optical parallelizing setup allows another tuning method. The aperture radius  $a$  and the focal length  $f_2$  of lens 2 determine the maximum incident angle  $\alpha_{\max}$  (see Fig. 5.4 (a)):

$$\alpha_{\max} = \arctan \frac{a}{f_2} \quad (5.1)$$

With  $f_2 = 50$  mm, the aperture limiting  $\alpha_{\max}$  to  $2^\circ$  would be a pinhole with 3.5 mm cross section. For an increasing aperture cross section, the cone of incident radiation gets wider, resulting in a blurring of the effective FPI transmission structure for all pixels (see e.g. Fig. 3.3). A measurement scheme with a narrow and a large aperture is thinkable. The transmission of a heavily blurred FPI transmission structure (Fig. 5.4 (c), dashed line) can for instance replace FPI setting B. This results in a somewhat lower sensitivity of the measurement.

The method could further be improved by using a ring aperture (see Fig. 5.4 (b)). The part of the light beam that is parallelized by the pinhole aperture would be masked (thereby the etendue can be kept constant). With a pinhole and a ring aperture (or two ring apertures), the settings A and B can be set. In this method, the FPI is fixed within the camera's light path, while tuning is done by reshaping the traversing radiation beam by the apertures.

Figure 5.4 (c) shows the effective FPI transmission for the pinhole (drawn line) and the ring aperture (dotted line). A ring aperture with an outer radius of  $\sim 4.4$  mm and an inner radius of  $\sim 3.5$  mm in the focal plane of a lens with  $f = 50$  mm was assumed.

An aperture tuning scheme would be comparably easy to build. Most likely, focusing issues limit the technique.

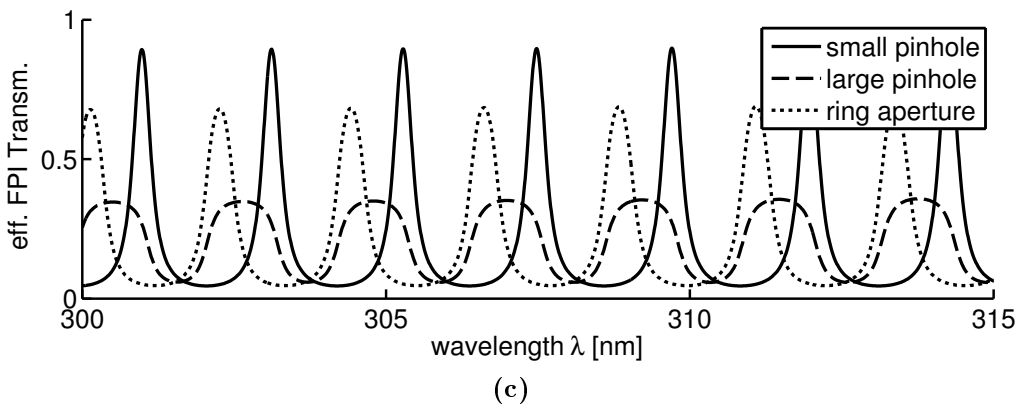
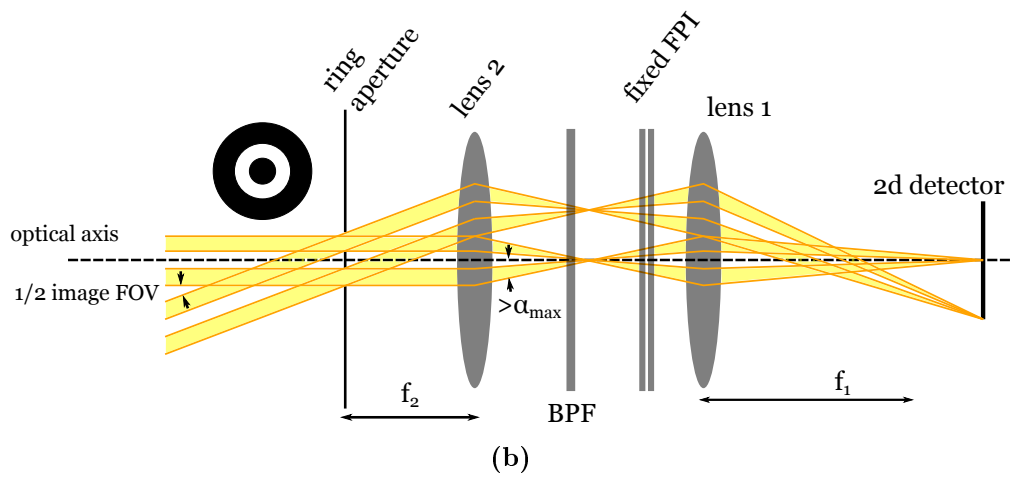
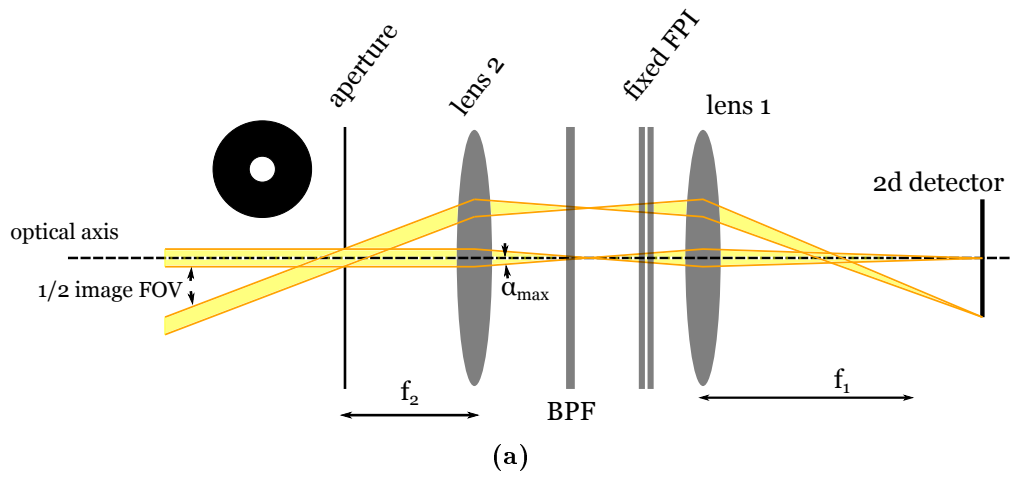


**Figure 5.4** – (a) a pinhole aperture is used to parallelize light from the camera FOV before it traverses the FPI with an approximately pixel independent transmission structure. (b) With a ring aperture, the light beam within the optical setup can be reshaped. It traverses the FPI now under larger angles, while the parallelized part is masked. (c) effective FPI transmission spectra for different aperture types.

## 5.3 Rings (no parallelization)

When rigidly mounting the FPI perpendicular to the optical axis in front of a camera, each incidence angle will see a different FPI transmission profile (see Sect. 3.2.3). This causes concentric rings of equal FPI transmission on the detector and in the camera FOV, respectively. (see e.g. Fig. 3.12 (b) and (c)). Figure 5.5 (a) and (b) show radiance measurements taken with a UV sensitive CCD camera. A BPF (similar to filter A' in Fig. 3.9) and the FPI of the OP setup were placed inside the camera light path. An image with (b) and without (a) an SO<sub>2</sub> gas cell, covering the whole camera FOV, was taken. Sub figure (c) shows the derived SO<sub>2</sub> optical density that is seen through the FPI. The expected rings are clearly visible.

This optical setup yields a  $\sim 30$  times higher etendue as the parallelized beam methods described in Sect. 5.2. However, inhomogeneous sensitivity across the detector makes the data evaluation challenging. In the following, some possible tuning implementations are discussed.

### 5.3.1 Tilt tuning

It is possible to simply tilt the FPI in front of the camera. However, the ring symmetry will be affected by the FPI tilt. In one half of the image, the incident angles get a positive contribution of the tilt angle  $\omega$ , on the other half they will get the same contribution with a negative sign. Moreover, due to the thickness of the FPI quartz plates, the image shifts on the detector.

For two tilt settings, there would be spots on the detector, where the SO<sub>2</sub> optical density is equal for both settings. At least three settings are needed to cover the whole camera FOV with SO<sub>2</sub> sensitivity. The variability of the SO<sub>2</sub> sensitivity across the detector can be minimized for an increasing number of different tilt positions.

### 5.3.2 Pressure tuning

A pressure tuning setup, as described in Sect. 5.2.2 can also be employed in the setup without beam parallelization. Compared to the tilt tuning approach, the ring symmetry would persist. The radii of the rings of maximum and minimum SO<sub>2</sub> optical density can be adjusted by varying the pressure. The result is similar to the surface separation tuning approach introduced in [Kuhn et al. \(2014\)](#). In between two settings there are rings of equal SO<sub>2</sub> optical density. So, also for pressure tuning, at least three tuning settings are needed to obtain sensitivity across the entire camera FOV.

### 5.3.3 Windowing

The windowing approach to FPI imaging is in principle different from the tuning approaches discussed above. The FPI is rigidly mounted in front of the camera. On

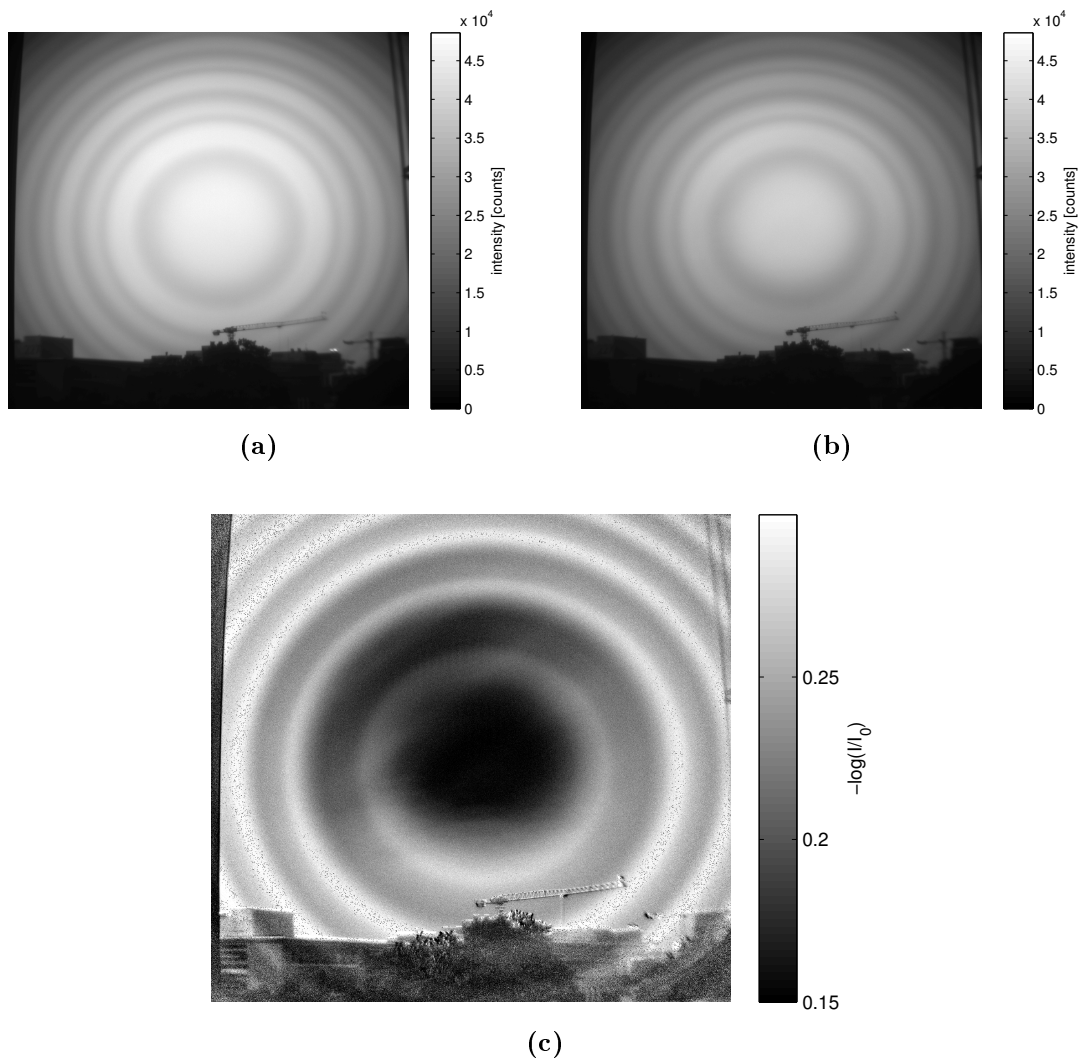


**Figure 5.5** – UV camera measurements with the SO<sub>2</sub> Camera filter A and the FPI inside the camera's FOV. The upper two images show the intensity without (a) and with (b) a SO<sub>2</sub> gas cell, covering the whole FOV. (c) SO<sub>2</sub> optical density calculated from (a) and (b). The expected ring structures are clearly visible.

the detector, the ring shaped patterns of different SO<sub>2</sub> optical density are present (as shown in Fig. 5.5 (c)). Tuning for each pixel is done by incrementally rotating the entire camera setup. In the different images, an object can be observed under slightly different camera incidence angles, and thus with different FPI transmissions.

The detector pixels are denoted by  $\{p, q\}$  in the following, the pixels of the image

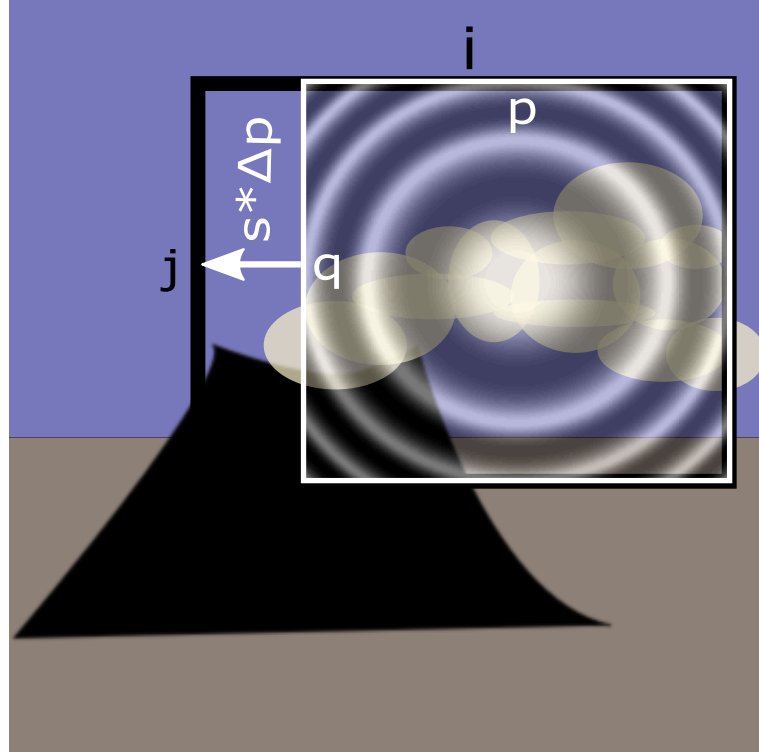


**Figure 5.6** – In black the frame of the final processed image is shown (coordinates  $i, j$ ). The camera FOV (coordinates  $p, q$ ) with its rings of SO<sub>2</sub> matching FPI pattern is moved across the image frame in order to gain sensitivity for every pixel  $\{i, j\}$ .

by  $\{i, j\}$  (see Figure 5.6). The FOV is shifted in  $s$  steps  $\Delta p$  in  $p$ -direction. For each image pixel  $\{i, j\}$  the measured radiance is

$$I_m^{\{i, j\}}(s) = \int d\lambda T_{cam}^{\{p(i, j, s), q(i, j, s)\}}(\lambda) Q^{\{p(i, j, s), q(i, j, s)\}}(\lambda) I^{\{i, j\}}(\lambda), \quad (5.2)$$

where  $T_{cam}^{\{p(i, j, s), q(i, j, s)\}}$  is the total transmittance of the camera optics (including FPI).  $Q^{\{p(i, j, s), q(i, j, s)\}}$  is the detector response of the camera for each image pixel  $\{i, j\}$  as a function of the shift  $s$ .

The transformation from image coordinates  $\{i, j\}$  to camera FOV coordinates  $\{p, q\}$  for a linear movement of the camera FOV in  $i$ -direction is given by:

$$p(i, j, s) = i + s\Delta p \quad (5.3)$$

$$q(i, j, s) = j \quad (5.4)$$

Shifting the camera FOV in a way that each image pixel at least once sees the FPI settings A and B as defined in Sect. 2.3.2 allows to calculate the AA for each pixel via:

$$\text{AA}^{\{i,j\}} = -\log\left(\frac{I_m^{\{i,j\}}(s_{\min})}{I_{m,0}^{\{i,j\}}(s_{\min})}\right) - \log\left(\frac{\cdot I_m^{\{i,j\}}(s_{\max})}{\cdot I_{m,0}^{\{i,j\}}(s_{\max})}\right) \quad (5.5)$$

$I_{m,0}$  denote the background radiances.  $s_{\max/\min}$  correspond to the values of  $s$  that maximize AA for each pixel. In the ideal case  $\text{AA}^{\{i,j\}}(S_{\text{SO}_2})$  for a given  $\text{SO}_2$  CD is pixel independent. In reality, the image pixels are observed with finite number of different FPI transmittance spectra. Certain pixels never see the two ideal FPI transmittances (setting A and B). This leads to an inhomogeneous sensitivity distribution across the image plane, depending on the step size  $\Delta p$ , the number of steps  $s$ , but also on the path of the FOV movement and the pixel size. These inhomogeneities can in principle be corrected for by calibration. In the following the  $\text{SO}_2$  sensitivity across the camera detector is investigated in a simulation.

## Simulation

We used the FPI model introduced in Chap. 3 for investigating the sensitivity of a windowing FPI  $\text{SO}_2$  camera across the image plane. The camera transfer function is fully represented by the incident angle dependence of FPI transmission:

$$T_{\text{cam}}^{\{p,q\}}(\lambda) = T_{\text{FPI}}(\lambda, \alpha(p, q)) \quad (5.6)$$

Influences of the BPF and the camera optics were neglected. A homogeneous spectral background radiance  $I^{\{i,j\}}(\lambda)$  was assumed using a measured spectrum of scattered sunlight. The relative  $\text{SO}_2$  sensitivity was determined by adding  $10^{18}$  molec  $\text{cm}^{-2}$  of  $\text{SO}_2$  for every pixel and calculating  $\text{AA}^{\{i,j\}}$  according to Eq. 5.5. Figure 5.7 shows the simulation results. The left column shows the final position of the camera FOV ( $200 \times 200$  pixels) in the image plane for  $s = [5, 10, 15]$  shifting steps. The step size  $\Delta p$  corresponds to  $1^\circ$ . The intensity distribution is shown in arbitrary units. We observe the ring structure that emerges due to the homogeneous background radiation and the homogeneous  $\text{SO}_2$  distribution. On the right side the respective resulting  $\text{SO}_2$  sensitivity distributions across the image plane are shown.

In the center of the camera FOV the concentric rings have a higher radial separation than at the FOV edges. Additionally, with respect to the moving direction, at the FOV edge columns, the perpendicular component of the rings and therefore the gradient of spectral FPI transmittance shift, is stronger than in the image center column. This leads to a low sensitivity in the image center for small total shifts. In the example, this can be observed for the images recorded at 5 and 10 steps, respectively. The image recorded at 15 steps has over a wide range a homogeneous  $\text{SO}_2$  sensitivity. The structures, that can still be observed can be reduced by choosing a smaller step size.

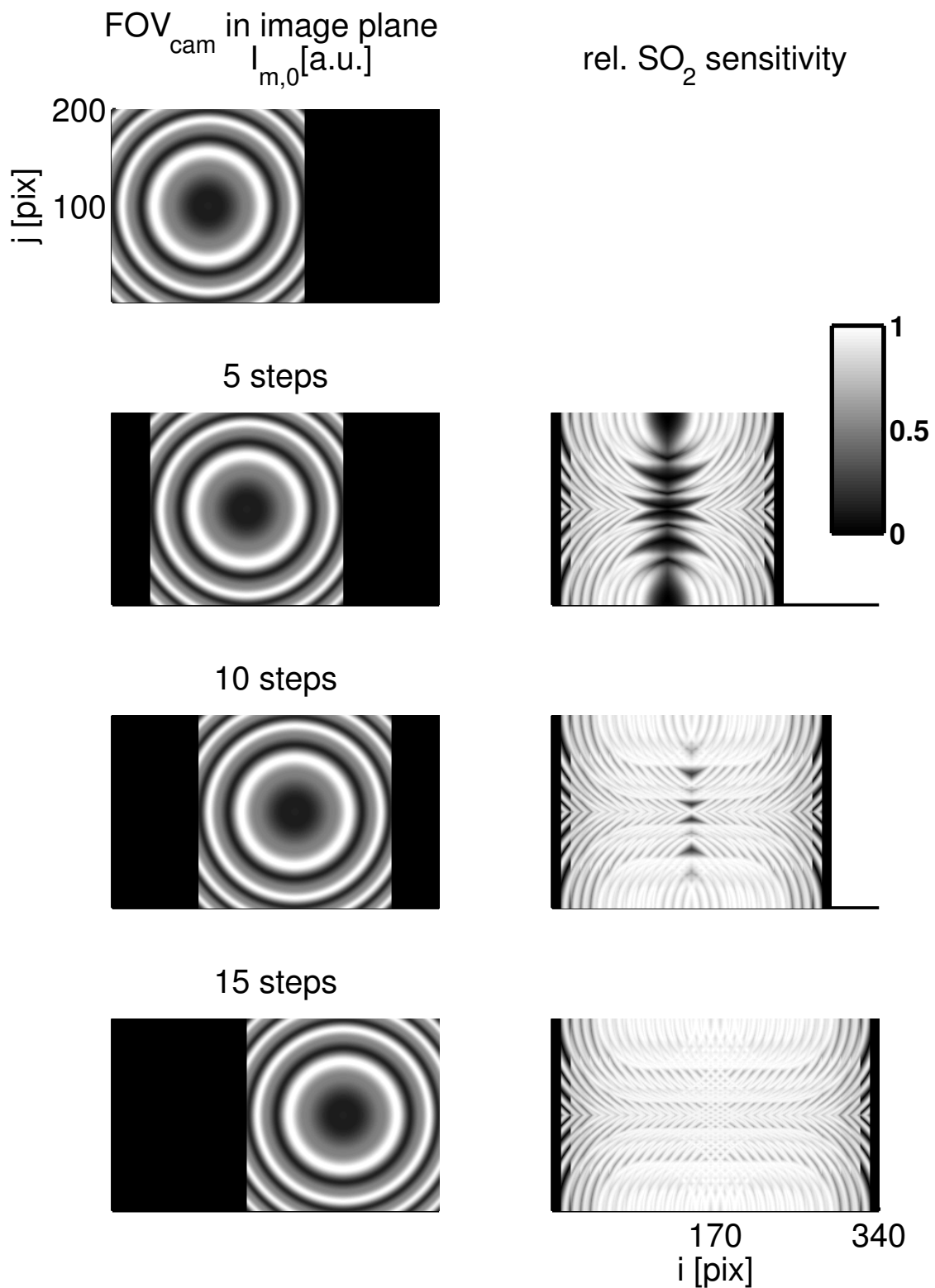


**Figure 5.7** – The left column shows the image FOV with the respective camera FOV in it after a different number of moving steps ( $\Delta p = 1^\circ$ ). In the right column the relative sensitivity distributions across the image FOV is shown. The image size, but also the sensitivity homogeneity increases with the number of steps and therefore with decreasing frame rate.

## Remarks

The simple and stable instrument setup is a major advantage of the windowing technique. Moreover, a high etendue is reached. In addition, the focus is not influenced by the tuning process.

One drawback is that this technique needs to record  $s > 2$  intensity images in order to obtain sensitivity across the whole image. Per pixel we therefore have more than the required two data points. This reduces the maximum achievable time resolution of the measurement. In order to retrieve the 2d SO<sub>2</sub> CD distributions, the images recorded under different angles have to be shifted to overlay again. For this, the employment of digital image processing might be required.

## 5.4 Summary

Table 5.1 summarizes the techniques introduced and discussed in this chapter. There is a tradeoff between the simplicity of the parallelizing beam optical setups and the high etendue of the non parallelizing optical setups. Finally, it comes down to the scattered UV radiance at the measurement location and the intended time resolution of the measurement. Experiments are required to verify the estimates of the practical limitations and to gain general experience in this rather novel field of UV remote sensing.

The imaging DOAS technique has the substantial advantage of being able to quantify several trace gases simultaneously. In principle the FPI technique can be applied to other trace gases as well (especially those with periodical absorption bands). In order to sense several gas species with optimum sensitivity, either very high FPI tuning ranges are required or several FPIs with different specifications have to be employed.

**Table 5.1** – Summary of the regarded imaging schemes. The relative light throughput per image pixel is estimated by the product of solid angle  $\Omega$  and cross section area  $A$  of the incoming light beam.  $\eta$  denotes the instrumental loss factor (accounting for e.g. FPI reflection or grating losses),  $N_{\gamma\lambda}$  is the number of radiance measurements, needed to acquire spectral information and  $N_{\text{frame}}$  the number of measurements needed to acquire a full frame image with  $100 \times 100$  pixels. The relative acquisition time  $t_{\text{frame}}$  per full frame measurement for a comparable SNR was estimated. It is assumed to be proportional to  $\sqrt{\eta} A \Omega N_{\gamma\lambda} N_{\text{frame}}$  for a photon shot noise dominated measurement. Advantages and technical limitations of the techniques are stated.

	<b>whisk broom</b>		<b>full frame</b>		<b>windowing</b>	
	spectrometer	OP FPI device	parallelized	ring symmetry:	ring symmetry	
per pixel	$A$ [mm <sup>2</sup> ] $\Omega$ [10 <sup>-6</sup> sr] $A\Omega$ [mm <sup>2</sup> sr]	0.05 48000 $2.4 \cdot 10^{-3}$	315 3800 1.2	9.5 9.5 $9 \cdot 10^{-5}$	315 9.5 $3.3 \cdot 10^{-3}$	315 9.5 $3.3 \cdot 10^{-3}$
rel. $A\Omega$ pp	1 (def.)	500	0.04	1.25	1.25	1.25
$\eta$	0.5	0.2	0.2	0.2	0.2	0.2
$N_{\gamma\lambda}^{-1}$	1	0.5	0.5	0.33 - 0.1	1	1
$N_{\text{frame}}^{-1}$	$10^{-4}$	$10^{-4}$	1	1	1	0.33 - 0.1
rel. $t_{\text{frame}}$	2333	330	3.7	1 - 3.3	1 (def.) - 3.3	
major advantages	several gases can be measured simultaneously	compact, negligible temperature dependence	ring structures avoided, simple evaluation	high etendue	no moving parts within camera setup, high etendue	
practical limitation	spatial mechanics	scanning mechanics	tilt tuning: further reduced etendue; aperture tuning: sensible optics; tuning: complex mechanics	intricate evaluation, asymmetrical rings for tilted FPI	intricate evaluation, image processing required	data processing

## 6 Conclusions and Outlook

### Conclusion

In this thesis, an optical remote sensing technique for atmospheric trace gases in the UV was investigated. The core of this technique is an Fabry-Pérot interferometer (FPI) with its spectral transmission matched to the trace gas molecule's absorption structures. The considerations concentrated on the application of this FPI technique to the differential absorption structures of SO<sub>2</sub> at wavelengths  $\lambda < 315$  nm. In contrast to dispersive remote sensing techniques (e.g. DOAS), the FPI technique can be applied in a fast imaging scheme.

A model was developed, in order to assess the basic behavior of the FPI and to simulate the instrument responses of different FPI setups. Optimal FPI setup parameters could be determined from SNR estimates. Within the model study, the FPI technique was compared to the filter based SO<sub>2</sub> Camera technique. Expected higher SO<sub>2</sub> sensitivity and selectivity of the FPI method could be confirmed. Moreover, the model results represented a basis for both, the design of the prototype of a one pixel (OP) FPI SO<sub>2</sub> remote sensing device, and the theoretical assessment and feasibility considerations of FPI imaging schemes.

In the scope of this thesis, the prototype of a portable and robust OP FPI SO<sub>2</sub> device was built. The motivation was the first proof of concept of the technique and to examine the performance of the FPI SO<sub>2</sub> remote sensing method apart from its imaging application. The instrumental setup was described and characterized. A first, unique SO<sub>2</sub> measurement could be performed. Using quartz cells containing known SO<sub>2</sub> CDs, a calibration curve of the instrument was recorded.

The drastically reduced cross interferences compared to the filter based SO<sub>2</sub> Camera could be verified to a large extent. Especially, the remarkably low influences of the solar zenith angle (and thus ozone interferences) and clouds to the FPI measurement were shown and are a major advantage over the filter based technique.

The progression of the measured calibration curve is as expected from the model. It enabled the determination of the noise equivalent SO<sub>2</sub> signal of the OP FPI SO<sub>2</sub> device to  $\sim 8.5 \cdot 10^{16}$  molec cm<sup>-2</sup> or  $\sim 34$  ppm m of SO<sub>2</sub> for a measurement period of 1 s. This is for instance already sufficient for the application in field measurements at many volcanoes. The low cross interferences would even allow an absolute calibration of the instrument.

In this rudimentary prototype, the noise is dominated by the imprecision of the employed servo motor. Suggestions were made by which, the SNR can be improved significantly. Moreover, a setup with comparable performance but no movable parts

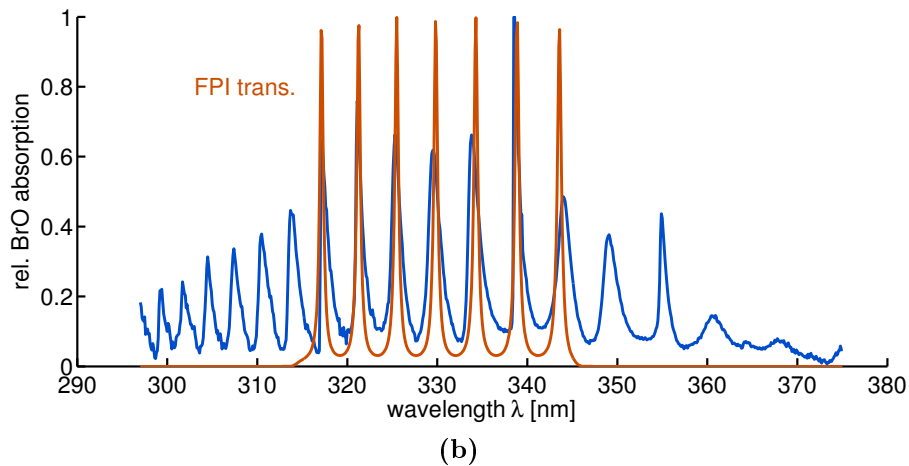
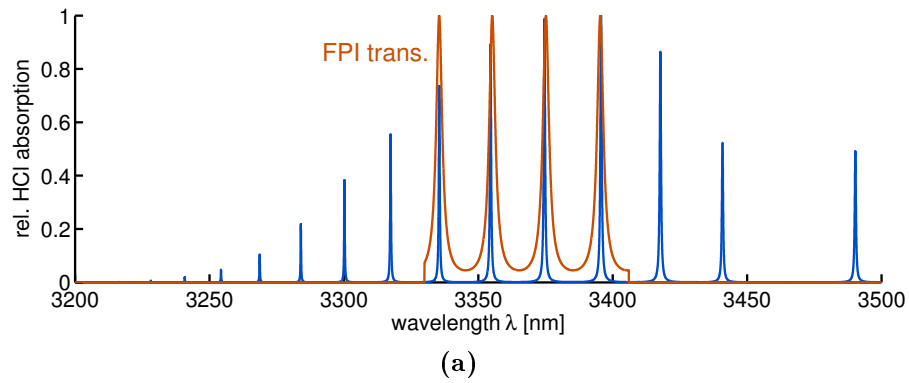


**Figure 6.1** – FPI transmittance spectra can be matched to the absorption features of many molecule species. Examples are shown for HCl **(a)** and BrO **(b)**.

is proposed.

In the last part of this thesis, considerations on the imaging application of the FPI remote sensing technique were introduced. Besides whisk broom scanning, several methods are presented that differ in their principal optical setup and their FPI tuning approach. The considerations are summarized in Tab. 5.1. The methods mainly differ in their extend limiting the measurement's time resolution, but also in the extent of required data post processing.

The FPI transmittance across the detector of a camera setup is essential for many FPI imaging implementations. This was modeled and experimentally confirmed. Ring shaped features of maximum and minimum  $\text{SO}_2$  optical densities on the detector could be verified by mounting the FPI and a BPF in front of a UV sensitive camera.

## Outlook

The detection limit of the OP FPI SO<sub>2</sub> setup can be significantly lowered by employing for instance a gear transition for the servo. It can be built more robust and compact. For the setup described in this thesis, dimensions of around 15 cm × 10 cm × 6 cm and a weight of < 1 kg can be reached.

Exploiting the FPI's reflection as, proposed in Sect. 4.2.4 allows the construction of a OP FPI device with no movable parts. The time resolution is not longer limited by the tuning process and radiances with FPI setting A and B can be recorded simultaneously. Since no temperature stabilization or servo motor would be needed, the power consumption of this setup would be extremely low with only ~ 350 mW. This is roughly a fifth of the typical cell phone power consumption. It could therefore easily be operated and fueled by a smart phone (e.g. on the basis of [Wilk, 2015](#)).

Moreover, it could be run by a series connection of ~ 10 lemons for some minutes. This is particularly interesting for measurements in Sicily at Mt. Etna.

Besides the OP applications, also FPI imaging schemes can be realized. For instance, the introduced windowing principle is easily implemented by rigidly mounting the FPI in front of a UV camera and mounting the camera on a rotary platform. Recorded images can be shifted back to overlay by digital image processing techniques.

The aperture tuning method is another exciting option. Its optical setup can also be implemented robustly, only an aperture has to varied. A comparable imaging instrument has probably never been realized, yet.

The FPI technique in principle works for all trace gases that have strong and ideally periodical narrowband absorption features. For volcanic studies, the assessment of the application to BrO or OClO would be interesting, though being much weaker absorbers than SO<sub>2</sub>. Moreover, the technique can be applied in other wavelength ranges. Fig. 6.1 shows FPI transmission structures roughly matched to HCl (sub figure (a), absorption data from [Rothman et al. \(2013\)](#) ) in the infrared and BrO (sub figure (b), absorption data from [Fleischmann et al. \(2004\)](#)) in the UV.

Another interesting point to consider is the application of a static FPI camera. A UV sensitive camera with BPF and FPI inside the light path is pointed towards the volcano, so that the summit is in the center of the ring shaped sensitivity features. Theoretically, the plume SO<sub>2</sub> could be quantified from intensity modulations at rings of high SO<sub>2</sub> optical density gradient on the detector. Although no full frame can be recorded with this method, it would be possible to determine SO<sub>2</sub> fluxes and plume propagation velocities (by correlation methods).

# Bibliography

- J. J. Barrett and S. A. Myers. New Interferometric Method for Studying Periodic Spectra Using a Fabry-Perot Interferometer. *J. Opt. Soc. Am.*, 61:1246–1251, 1971.
- S. Beirle, C. Hörmann, M. Penning de Vries, S. Dörner, C. Kern, and T. Wagner. Estimating the volcanic emission rate and atmospheric lifetime of SO<sub>2</sub> from space: a case study for Kilauea volcano, Hawai'i. *Atmos. Chem. Phys.*, 14:8309–8322, 2014.
- D. Benton. Passive scene imaging of absorbing gases by narrowband dielectric filter modulation. *Journal of the European Optical Society - Rapid publications*, 8(0), 2013. ISSN 1990-2573. URL [http://www.jeos.org/index.php/jeos\\_rp/article/view/13008](http://www.jeos.org/index.php/jeos_rp/article/view/13008).
- G.J.S. Bluth, J.M. Shannon, I.M. Watson, A.J. Prata, and V.J. Realmuto. Development of an ultra-violet digital camera for volcanic SO<sub>2</sub> imaging. *J. Volcanol. Geotherm. Res.*, 161(12):47 – 56, 2007.
- N Bobrowski and G Giuffrida. Bromine monoxide/sulphur dioxide ratios in relation to volcanological observations at Mt. Etna 2006–2009. *Solid Earth*, 3(2):433–445, 2012.
- Kelly V Chance and Robert JD Spurr. Ring effect studies: Rayleigh scattering, including molecular parameters for rotational Raman scattering, and the Fraunhofer spectrum. *Applied Optics*, 36(21):5224–5230, 1997.
- Wolfgang Demtröder. *Laserspektroskopie: Grundlagen und Techniken*. Springer-Verlag, 2007.
- O.C Fleischmann, M. Hartmann, J.P. Burrows, and J. Orphal. New ultraviolet absorption cross-sections of BrO at atmospheric temperatures measured by a time-windowing Fourier transform spectroscopy. *J. Photochem. Photobiol. A.: Chem.*, 168:117–132, 2004.
- Bo Galle, Mattias Johansson, Claudia Rivera, Yan Zhang, Manne Kihlman, Christoph Kern, Thomas Lehmann, Ulrich Platt, Santiago Arellano, and Silvana Hidalgo. Network for Observation of Volcanic and Atmospheric Change (NOVAC)—A global network for volcanic gas monitoring: Network layout and instrument description. *J. Geophys. Res., D*, 115(D5), 2010. ISSN 2156-2202.
- J. Grainger and J. Ring. Anomalous Fraunhofer Line Profiles. *nature*, 193:762, 1962.

- H. Horvath. The refractive index of Freon 12. *Appl. Opt.*, 6, 1967.
- C. Kern, F. Kick, P. Lübcke, L. Vogel, M. Wöhrbach, and U. Platt. Theoretical description of functionality, applications, and limitations of SO<sub>2</sub> cameras for remote sensing of volcanic plumes. *Atms. Meas. Tech.*, 3:733–749, 2010.
- C. Kern, C. Werner, T. Elias, A. J. Sutton, and P. Lübcke. Applying UV cameras for SO<sub>2</sub> detection to distant or optically thick volcanic plumes. *J. Volcanol. Geotherm. Res.*, 262:80–89, 2013.
- Rei Kitamura, Laurent Pilon, and Miroslaw Jonasz. Optical constants of silica glass from extreme ultraviolet to far infrared at near room temperature. *Appl. Opt.*, 46 (33):8118–8133, 2007.
- J. Kuhn, N. Bobrowski, P. Lübcke, L. Vogel, and U. Platt. A Fabry–Perot interferometer-based camera for two-dimensional mapping of SO<sub>2</sub> distributions. *Atmospheric Measurement Techniques*, 7(11):3705–3715, 2014. doi: 10.5194/amt-7-3705-2014. URL <http://www.atmos-meas-tech.net/7/3705/2014/>.
- J Lampel, U Frieß, and U Platt. The impact of vibrational Raman scattering of air on DOAS measurements of atmospheric trace gases. *Atmos. Meas. Tech. Discuss.*, 8(3):3423–3469, 2015.
- F. Lohberger, G. Hönninger, and U. Platt. Ground-based imaging differential optical absorption spectroscopy of atmospheric gases. *Appl. Opt.*, 43:4711–4717, 2004.
- P. Lübcke, N. Bobrowski, S. Illing, C. Kern, J. M. Alvarez Nieves, L. Vogel, J. Zielcke, H. Delgado Granados, and U. Platt. On the absolute calibration of SO<sub>2</sub> cameras. *Atmos. Meas. Tech.*, 6:677–696, 2013.
- Lawrence L Malinconico. Fluctuations in SO<sub>2</sub> emission during recent eruptions of Etna. *Nature*, 278:43–45, 1979.
- Gustav Mie. Beiträge zur Optik trüber Medien, speziell kolloidaler Metallösungen. *Ann. Phys.*, 330(3):377–445, 1908.
- A. J. Moffat and M. M. Millan. The applications of optical correlation techniques to the remote sensing of SO<sub>2</sub> plumes using sky light. *Atmos. Environ.*, 5:677–690, 1971.
- T. Mori and M. Burton. The SO<sub>2</sub> camera: A simple, fast and cheap method for ground-based imaging of SO<sub>2</sub> in volcanic plumes. *Geophys. Res. Lett.*, 33, 2006.
- Rodolfo Olmos, José Barrancos, Claudia Rivera, Francisco Barahona, Dina L López, Benancio Henriquez, Agustín Hernández, Efraim Benitez, Pedro A Hernández, Nemesio M Pérez, et al. Anomalous emissions of SO<sub>2</sub> during the recent eruption of Santa Ana volcano, El Salvador, Central America. *Pure Appl. Geophys.*, 164 (12):2489–2506, 2007.

- A Perot and Charles Fabry. On the application of interference phenomena to the solution of various problems of spectroscopy and metrology. *Astrophys. J.*, 9:87, 1899.
- Marco Pisani and Massimo E. Zucco. Compact imaging spectrometer combining Fourier transform spectroscopy with a Fabry-Perot interferometer. *Opt. Express*, 17(10):8319–8331, May 2009. doi: 10.1364/OE.17.008319. URL <http://www.opticsexpress.org/abstract.cfm?URI=oe-17-10-8319>.
- U. Platt and J. Stutz. *Differential Optical Absorption Spectroscopy: Principles and Applications (Physics of Earth and Space Environments)*. Springer, 2008.
- U Platt, D Perner, and HW Pätz. Simultaneous measurement of atmospheric CH<sub>2</sub>O, O<sub>3</sub>, and NO<sub>2</sub> by differential optical absorption. *J. Geophys. Res.*, 84(C10):6329–6335, 1979.
- SA Pollack. Angular dependence of transmission characteristics of interference filters and application to a tunable fluorometer. *Appl. Opt.*, 5(11):1749–1756, 1966.
- Alan Robock. Volcanic eruptions and climate. *Rev. Geophys.*, 38:191–219, 2000.
- Walter Roedel and Thomas Wagner. Aerosole. In *Physik unserer Umwelt: Die Atmosphäre*, pages 463–519. Springer, 2011.
- L.S. Rothman, I.E. Gordon, Y. Babikov, A. Barbe, D. Chris Benner, P.F. Bernath, M. Birk, L. Bizzocchi, V. Boudon, L.R. Brown, A. Campargue, K. Chance, E.A. Cohen, L.H. Coudert, V.M. Devi, B.J. Drouin, A. Fayt, J.-M. Flaud, R.R. Gamache, J.J. Harrison, J.-M. Hartmann, C. Hill, J.T. Hodges, D. Jacquemart, A. Jolly, J. Lamouroux, R.J. Le Roy, G. Li, D.A. Long, O.M. Lyulin, C.J. Mackie, S.T. Massie, S. Mikhailenko, H.S.P. Müller, O.V. Naumenko, A.V. Nikitin, J. Orphal, V. Perevalov, A. Perrin, E.R. Polovtseva, C. Richard, M.A.H. Smith, E. Starikova, K. Sung, S. Tashkun, J. Tennyson, G.C. Toon, Vl.G. Tyuterev, and G. Wagner. The {HITRAN2012} molecular spectroscopic database. *Journal of Quantitative Spectroscopy and Radiative Transfer*, 130(0):4 – 50, 2013. ISSN 0022-4073. doi: <http://dx.doi.org/10.1016/j.jqsrt.2013.07.002>. URL <http://www.sciencedirect.com/science/article/pii/S0022407313002859>. {HITRAN2012} special issue.
- A. Serdyuchenko, V. Gorshelev, M. Weber, W. Chehade, and J.P. Burrows. High spectral resolution ozone absorption cross-sections – Part 2: Temperature dependence. *Atmos. Meas. Tech.*, 7:625–636, 2014.
- sflux GmbH. Sic uv photodiode selection guide, 2015. URL [http://www.sflux.de/fileadmin/pdf-links/UV\\_photodiode\\_selection\\_guide.pdf](http://www.sflux.de/fileadmin/pdf-links/UV_photodiode_selection_guide.pdf). Retrieved 23 June 2015.

- C. Spinetti and M.F Buongiorno. Volcanic aerosol optical characteristics of Mt. Etna tropospheric plume retrieved by means of airborne multispectral images. *J. Atmos. Sol.-Terr. Phy.*, 69:981–994, 2007.
- C Textor, HF Graf, C Timmreck, and A Robock. *Emissions of Atmospheric Trace Gas Compounds*, chapter Emissions from volcanoes, pages 296–303. Kluwer, Dordrecht, 2004.
- Jan-Lukas Tirpitz. Optimierung von In-Situ-Gasmonitoren für CO<sub>2</sub> und SO<sub>2</sub>. Bachelorarbeit, University of Heidelberg, 2014.
- A.C. Vandaele, C. Hermans, and S. Fally. Fourier transform measurements of SO<sub>2</sub> absorption cross sections: II. Temperature dependence in the 29000-44000 cm<sup>-1</sup> (227-345 nm) region. *J. Quant. Spectrosc. Radiat. Transfer*, 110:2115–2126, 2009.
- T Wagner, B v Dix, C v Friedeburg, U Frieß, S Sanghavi, R Sinreich, and U Platt. MAX-DOAS O<sub>4</sub> measurements: A new technique to derive information on atmospheric aerosols—Principles and information content. *Journal of Geophysical Research: Atmospheres (1984–2012)*, 109(D22), 2004.
- Richard Wehr, Eamonn McKernan, Adrian Vitcu, Roman Ciurylo, and James R. Drummond. Dynamic spectroscopic measurements of the temperature and pressure cycles in a MOPITT pressure modulator cell. *Appl. Opt.*, 42(33):6595–6604, Nov 2003. doi: 10.1364/AO.42.006595. URL <http://ao.osa.org/abstract.cfm?URI=ao-42-33-6595>.
- Christoph Wilk. Entwicklung eines Ein-Pixel-SO<sub>2</sub>-Sensors. Bachelorarbeit, University of Heidelberg, 2015.
- E. L. Wilson, E. M. Georgieva, and W. S. Heaps. Development of a Fabry-Perot interferometer for ultra-precise measurements of column CO<sub>2</sub>. *Meas. Sci. Technol.*, 18(5):1495–1502, 2007.

# Danksagungen

Ich möchte mich herzlich bedanken bei

Prof. Ulrich Platt für die Möglichkeit an diesem spannenden Thema arbeiten zu dürfen und für den Optimismus und die Risikobereitschaft, die Voraussetzungen für diese Arbeit waren. Außerdem möchte ich mich für die Ermöglichung der Teilnahme an den Konferenzen bedanken.

Prof. Thomas Wagner für die Übernahme des Zweitgutachtens.

meinen Betreuern Peter Lübcke und Nicole Bobrowski, die immer offen für Fragen und Diskussionen waren und auch wesentlich dazu beitrugen die Motivation aufrecht zu erhalten. Bei Nicole möchte ich mich zudem für die Ermöglichung der Teilnahme an der Kampagne auf Sizilien bedanken bei der ich wertvolle Erfahrungen sammeln durfte.

Leif Vogel, der im Rahmen meiner Bachelorarbeit wertvolle Beiträge zu dieser Arbeit geleistet hat.

Lukas Tirpitz und Denis Pöhler für die Unterstützung bei der experimentellen Arbeit.

Peter Lübcke, Nicole Bobrowski, Angelika Klein, Simon Warnach und Lukas Tirpitz für wertvolle Korrekturen.

Johannes Zielcke für Korrekturen, hilfreiche Ratschläge, und viele Kilometer in den Bergen.

der ganzen Arbeitsgruppe für die angenehme Atmosphäre und die große Hilfsbereitschaft.

meinen Mitbewohnern für die Übernahme von Hausarbeiten, für willkommene Abwechslung; und insbesondere Jonas, der mich während meines ganzen Studiums begleitete und in abendlichen Diskussionen auch zu dieser Arbeit beitrug.

allen Freunden für jegliche Ausbrüche aus dem Alltag.

meiner Familie, insbesondere meinen Eltern Susanne und Martin für die jahrelange, uneingeschränkte Unterstützung und meinen Geschwistern Simone, Peter und Verena auf die ich mich immer verlassen konnte.

Amanda, für ein unaussprechliches Pensum an Unterstützung, Geduld und Toleranz.

Erklärung:

Ich versichere, dass ich diese Arbeit selbstständig verfasst habe und keine anderen als die angegebenen Quellen und Hilfsmittel benutzt habe.

Heidelberg, den (Datum) .....